Studies of Chemical Adsorption Using Low-Energy Electron Diffraction

Thesis by

Ellen D. Williams

In Partial Fulfillment of the Requirements
for the Degree of

Doctor of Philosophy

California Institute of Technology
Pasadena, California

1982

(Submitted September 10, 1981)

Table of Contents

Acknowledgments

I would like to express my deep appreciation to my research advisor, Henry Weinberg, who has encouraged me to strive for independence and excellence in my scientific research, as well as providing his personal support in my endeavors. In addition, I am grateful for having had the opportunity to interact with the graduate students, post-doctoral fellows and visiting faculty who have been associated with the Weinberg group during my years at Caltech. In particular, I have benefitted from collaboration and discussion with Bill Bowser, Chi -Ming Chan, Steve Cunningham, Howard Evans, Jim Gleeson, Dale Ibbotson, Charles Sobrero, Pat Thiel and John Yates.

I would also like to thank the staff of the chemical engineering department. Their friendliness and competence make working in the department a pleasure. In particular, I am indebted to George Griffith, Kathy Lewis, Seichi Nakawatase, Mike Nagy, Ray Reed, Henry Smith and John Yehle for their help.

I am deeply grateful to my parents, Lois and Richard Williams, for their life-long support, and to my parents-in-law, Liedeke and Tom Gehrels, who have welcomed me into their family. Most of all, I would like to thank my husband, Neil Gehrels, who makes it all worthwhile.

I have received financial support for my graduate studies from the National Science Foundation and International Business Machines, Inc.

Abstract

Both experimental and computational studies based on low-energy electron diffraction (LEED) have been performed to determine the nature of order in chemically adsorbed overlayers. These studies have been directed towards obtaining a better understanding of adatom-adatom interactions by measurement of their most obvious manifestations; change in overlayer order during adsorption and co-adsorption, island formation, and order-disorder phenomena.

The effect of the co-adsorption of hydrogen on the ordering of CO on Rh(111) has been studied using LEED and thermal desorption mass spectrometry. The results indicate that the adsorption of CO proceeds via a physically adsorbed intermediate. In addition, there is a strong repulsive interaction between CO molecules and hydrogen atoms co-adsorbed on Rh(111). This interaction is apparent at distances up to 2.7 - 3.1 Å indicating that it is a through-metal effect.

A series of LEED patterns has been observed during the adsorption of sulfur on the reconstructed IR(110)-(1x2) surface. The structure observed at lowest coverages has a p2mg symmetry. This allows a determination of the absolute coverage, and indicates a probable binding site for the sulfur atoms.

A Monte Carlo simulation of the order-disorder behavior of oxygen on W(110) has been performed. General expressions relating the values of the interaction energies to the transition temperatures for a lattice gas with first, second and third neighbor interactions have been determined. Symmetry considerations in selecting a model for the interaction energies are discussed.

The effect of the ordering of adsorbed molecules into small islands on the LEED beam profile has been determined. In the limit of a random distribution of island positions the overall intensity is shown to be the weighted sum of the intensities from the individual islands. Computer simulations of island-containing overlayers have been used to determine the effect on the beam profiles of deviations from a random distribution of islands.

Experimental studies of island formation for CO on Ru(001) have

been performed. The finite size of the ordered islands has a strong effect on the order-disorder behavior. Quantitative measurements of this effect have allowed a determination of the island size distribution and thus, the mean island size as a function of coverage.

I. Introduction

In the mid 1920's Davisson and Germer demonstrated the wave nature of the electron by diffracting low-energy electrons from the (111) surface of nickel(1). The fundamental significance of their experiment was so great that it overshadowed the significance of their results concerning the nickel surface itself. Thus, for almost forty years, the use of low-energy electron diffraction (LEED) to study surfaces was largely neglected. Improvements in ultra-high vacuum technology in the 1960's led to a resurgence of interest in the study of solid surfaces and LEED became a common technique used for a multitude of pruposes. One application of LEED is as a qualitative probe to monitor changes in geometry of the surface during chemical adsorption. Furthermore, there has been a great deal of interest in developing LEED as a quantitative tool for the determination of surface structure on an atomic scale(2). In addition to the lively activity in these two areas of LEED research, a rather small number of workers have been developing LEED as a quantitative technique for the study of long range order on surfaces(3,4). Finally, an application of LEED has been developed that has significance not only for surface studies, but also for the understanding of the theory of phase transitions. This is the study of two-dimensional order-disorder phenomena in chemically adsorbed overlayers. It is currently one of the most exciting areas of research in surface science, and it is described more thoroughly in the following.

When a molecule chemically adsorbs on a surface, there is generally one location with respect to the surface atoms (i.e. bridge site, on-top site, etc.) for which the binding energy is strongest. Thus, a single crystal surface represents a periodic array of binding sites for the adsorbed species. It is frequently observed using LEED that mol-

ecules adsorb in ordered overlayers with a periodicity related to but greater than that of the surface atoms. The fact that all of the available binding sites are not occupied indicates that there must be adatom-adatom interactions that dictate the positions of adsorbed species with respect to one another. The symmetry of the structure of the overlayer is determined by the qualitative nature of the interactions. A wide variety of types of overlayers are observed in LEED, and it is often necessary to postulate the existence of interactions that are anisotropic and oscillatory in sign with distance to explain the observations. Such interactions arise as a result of overlap of the oscillatory electron density in the metal set up by the adsorbed molecules(5,6).

From the preceding discussion, it is apparent that chemically adsorbed overlayers represent a physical realization of the two-dimensional lattice gas that has been widely used as a model in studies of the theory of phase transitions(7). It is surprising that in spite of intense theoretical interest in two dimensional order-disorder transitions, the first experimental evidence for such a transition, reported by Davisson and Germer for the (2x2) structure of oxygen on Ni(111) in 1927, went unremarked for over forty years. Order-disorder behavior in chemically adsorbed overlayers was rediscovered by Buchholz and Lagally for the system of oxygen on W(110) in 1975(6). Since that time there have been slowly increasing numbers of experimental reports of order-disorder phenomena in chemically adsorbed systems.

The theory of two-dimensional order-disorder phenomena has been studied extensively. Until recently, most of the literature has been couched in terms of the Ising model, i.e. of spins on a lattice, rather than in terms of a lattice gas. Fortunately, the transformation from

the spin lattice to lattice gas is well understood, so that the theoretical results are readily applicable to lattice gas systems. However, the theory of phase transitions, even for the idealized lattice systems, is extremely difficult. Therefore, analytical results have been obtained only for a few very simple systems. These systems include many lattice geometries but are rather limited in the range of interactions between neighboring sites. This is a problem, since chemically adsorbed overlayers frequently display rather complex structures that must be the result of rather complex sets of interaction energies. In addition, analytical results have been obtained only for spin lattices in zero magnetic field. The analogy between spin lattices and lattice gases is such that a spin lattice in zero magnetic field corresponds to a lattice gas at half coverage. Therefore comparison with theory is limited to only one coverage, whereas experimental phase diagrams of transition temperature as a function of coverage are rich with information about the adatom-adatom interactions.

To circumvent the limited availability of analytical results, various approximate methods have been developed. The most successful, in terms of calculating phase diagrams for lattice gases, have been Monte Carlo simulation(9) and renormalization group theory(10). In Monte Carlo simulation, a model of the system of interest is created. Then the system is changed from its original configuration by changes in the positions of individual atoms in the model, governed by the Boltzmann probabilities. When changes in atomic positions no longer cause changes in the thermodynamic quantities of the system, equilibrium has been reached and the properties of interest can be calculated from the known configuration of the atoms. The Monte Carlo technique has the advan-

tages that it is conceptually simple and that it generates physical configurations of the system which can provide insight into the observed types of behavior. The disadvantages of the Monte Carlo technique are that it is necessary to use a finite size model, and that it is extremely demanding in terms of computer time.

Renormalization group theory is based on the idea of using a change of scale to reduce the range of correlations in a system. In this way, a difficult many body problem can be reduced to a solvable few body problem. Once a solution is found, the scaling transformations are reversed to obtain the solution for the original problem. The scaling hypothesis, if correct anywhere(11), is only strictly correct near a critical point. However, renormalization group theory has been used to calculate phase diagrams even far from a critical point that are in reasonable agreement with diagrams calculated by other methods. Although, it is an approximate technique, renormalization group has the benefit that, once the transformations have been set up, phase diagrams can be calculated fairly easily. This allows the effects of changing parameters in the model system to be determined readily, in contrast to Monte Carlo simulations.

It is immediately apparent that LEED, which measures the degree of order in the overlayer, is suitable for following order-disorder transitions. The transitions which have been measured using LEED to date have fallen into two categories. The first is the second order transition that occurs with increasing temperature at or near the optimum coverage for the overlayer structure(12). At these coverages, the LEED beam is the sum of a delta function due to the long range order, and a Lorentzian due to the short range order. The long range order, and thus

the intensity due to the long range order drop abruptly to zero at the transition temperature, T_c. The correlation length, which defines the short range order, diverges at T_c. The contribution of short range order to the intensity is therefore a maximum, and the width of the Lorentzian a minimum at T_c. These effects will be obscured by instrumental broadening, which must be taken into account before a quantitative analysis of the diffracted beam profiles can be made.

At lower coverages, first order transitions from a two-phase coexistence regime to a one phase regime have been observed using LEED(13). The ordered phase in the two phase region consists of many small ordered clusters called islands. As the temperature is increased, the density of the disordered phase increases at the expense of the islands. This leads to a gradually decreasing intensity and increasing width of the LEED beams. The two phase region disappears entirely at the transition temperature. At this point there will still be some short range order in the homogeneous disordered phase. However, the contribution of this to the LEED intensity will be so small that the transition temperature can be defined adequately as the point at which the LEED beam profile becomes indistinguishable from the background.

Both the theoretical and experimental frameworks are in place for the study of order-disorder phenomena and adatom-adatom interactions using LEED. In this thesis, several studies related to these topics are described. In sections III and IV experimental studies investigating the qualitative influence of adatom-adatom interactions on overlayer structures are presented. A Monte Carlo simulation of the order-disorder behavior of oxygen on W(110) is described in section II. In section V the determination of a quantitative relationship between the finite sizes of ordered

regions on the surface and the shape of the diffracted beam profile is presented.

Finally, an experimental determination of the order-disorder behavior of CO on Ru(001) and an analysis of the results using the relationships derived in section V are described in section VI.

References

1. C. Davisson and L. H. Germer, Phys. Rev. 30, 705(1927).

2. M. A. Van Hove and S. Y. Tong, Surface Crystallography by LEED - Theoretical Methods and Computer Programs, Springer-Verlag, New York 1978.

3. R. L. Park, in Structure and Chemistry of Solid Surfaces, Ed. G. Somorjai, Wiley, New York, 1969.

4. M. Henzler, in Electron Spectroscopy for Surface Analysis, Springer-Verlag, New York, 1977.

5. T. B. Grimley and M. Torrini, J. Phys C6,868(1973).

6. T. L. Einstein and J. R. Schrieffer, Phys. Rev. B7,3629(1973).

7. T. D. Lee and C. N. Yang, Phys. Rev. 87,410(1952).

8. J. C. Buchholz and M. G. Lagally, Phys. Rev. Letters 35,442(1975).

9. D. P. Landau in Monte Carlo Methods in Statistical Physics, Ed. K. Binder, Springer-Verlag, New York, 1979.

10. C. Domb and M. S. Green, Eds., Phase Transitions and Critical Phenomena, Vol. 6, Academic Press, New York, 1977.

11. H. E. Stanley, Introduction to Phase Transitions and Critical Phenomena, Oxford University Press, New York, 1971.

12. L. D. Roelofs, A. R. Kortan, T. L. Einstein and R. L. Park, Phys. Rev. Letters 46,1465(1981).

13. M. G. Lagally, T. -M. Lu and G. -C. Wang in Ordering in Two Dimensions, Ed. S. Sinha, Elsevier, Amsterdam, 1980.

Section II

A Determination of Adatom-Adatom Interactions Energies: Application to Oxygen Chemisorbed on the Tungsten (110) Surface

[This section was published as a paper by E. D. Williams, S. L. Cunningham and W. H. Weinberg, in *The Journal of Chemical Physics* 68, 4688 (1978).]

Abstract

A Monte Carlo simulation has been carried out to describe two-dimensional order-disorder phenomena. The model contains (attractive) first, (repulsive) second, and (attractive) third neighbor pairwise interactions. The special case of oxygen chemisorption on a tungsten (110) surface, on which an ordered p(2x1) overlayer is formed at low surface temperatures, is considered explicitly. From the measured order-disorder transition temperatures at both quarter- and half-monolayer surface coverages, (non-unique) values of the three pairwise interaction energies have been determined. These pairwise interaction energies have been used to determine the variation in the total interaction energy, the heat capacity and the entropy with surface temperature.

1. Introduction

The interaction of oxygen with the (110) surface of tungsten has been studied thoroughly by a number of investigators[1,2,3,4,5]. Up to, and somewhat above, half-monolayer coverage, oxygen forms a p(2x1) ordered array when adsorbed on W(110) near room temperature. When the temperature is increased, a rapid decrease in the intensity of the half-order beams in the LEED pattern occurs, beginning near 450 K. The decrease is much greater than that due to a Debye-Waller attenuation, and it is not caused by desorption of oxygen which takes place only at much higher temperatures. The decrease in intensity must be due therefore to a reduction in the degree of order of the oxygen overlayer. If this loss of order is due to movement of the adatoms between sites of equivalent symmetry, rather than between different kinds of sites, then the adsorbed oxygen can be described as a two-dimensional lattice gas with interactions between adatoms on neighboring sites. The disordering of the overlayer structure with increasing temperature then corresponds to the order-disorder transition which is predicted theoretically for such a gas[6]. Since the temperature dependence of the degree of order is determined solely by the adatom interaction energies in this model, experimental data concerning LEED beam intensities as a function of temperature can be used to determine the values of the interaction energies.

2. Model for the Adatom Interactions

The position of the oxygen atoms on W(110), as determined by dynamical calculations of LEED intensity-voltage (I-V) spectra[7], is shown in Fig. 1. In addition to the structure shown, the rows of oxygen atoms could be shifted over by one row of tungsten atoms into an anti-phase domain, or rotated to lie in the $(0,\bar{1})$ direction in a perpendicular domain. The four

possible domains are equivalent insofar as the symmetry of the surface is concerned and will occur with equal probability on a perfect surface.

Two possible models for the adatom interaction energies giving rise to the observed p(2x1) structure are shown in Fig. 1. The interactions ε_a, ε_b and ε_{2b}, where ε_a and ε_{2b} are attractive and ε_b repulsive, were used in two previous attempts to analyze LEED intensity-temperature (I-T) data for this system.[5,8] This model will certainly account for the formation of a p(2x1) structure. However, there are several serious flaws in it. As Ertl[8] has pointed out, if only two-body interactions are in effect (as was assumed in the prior analyses), it is a violation of fundamental symmetry restrictions to assign different values to ε_a and ε_b which correspond to interactions over the same distance in the crystallographically equivalent directions (1,0) and $(0,\bar{1})$. Furthermore, this set of two-body interactions would not allow the formation of perpendicular domains, which are known to be present since both the $(0,\frac{1}{2})$ and $(\frac{1}{2},0)$ LEED beams are observed experimentally. Finally, in both of the earlier studies, the values of ε_a and ε_{2b} were found to be equal. Since theoretical results[9-11] indicate that the magnitude of the interactions should decrease with increasing distance, this is further evidence that this model is physically unrealistic.

The interaction model used in this study, with the parameters ε_1, ε_2, ε_3 and ε_4 where ε_1 and ε_4 are attractive, and ε_2 and ε_3 are repulsive, also gives rise to a p(2x1) structure, but in a more physically reasonable manner. All four interactions are invariant under the symmetry operations of the surface and thus form a consistent set of two-body interactions. This conformity with surface symmetry also allows perpendicular domains to form with equal probability. The inclusion of the second and third neighbor

interactions, which were ignored in the earlier studies, is physically reasonable in light of the importance of the longer range attractive fourth neighbor interaction, which is necessary to explain the persistence of order at low coverages.

Three-body effects are likely to be important in adatom-adatom interactions[10,11]. It seems possible that there would be variations in the values of ε_1 and ε_4 in the (1,0) and $(0,\bar{1})$ directions due to three-body effects and the orientation of the domain being considered. While the method of analysis used for this work could easily be adapted to deal with three-body interactions, this was not done since the data were not sufficient to determine uniquely the larger number of parameters this would entail. For the same reason, the parameters ε_2 and ε_3, which undoubtedly have slightly different values, were assumed to be equal for this study.

Both models for the interaction energies shown in Fig. 1 implicitly disregard the existence of an equivalent lattice of three-fold adsorption sites. Within a given domain or island, occupation of sites on both lattices would not be expected due to the strong through-space interactions which would arise in such a case. Disordering by motion of adatoms out of an island at low coverage could, of course, result in occupation of sites on both lattices, but this would be reflected only as small perturbations in the high temperature tail of the I-T curve.

3. Methodology

Using the interaction model containing ε_1, $\varepsilon_2 = \varepsilon_3$, and ε_4, the experimental data of Lu et al.[5] were analyzed by the Monte Carlo method. It is known that a Monte Carlo calculation can reproduce the analytical results for a lattice gas with only nearest-neighbor interactions at half-monolayer

coverage[12,13]. Hence, the extension of the method to systems with more complex interactions and to coverages other than half-monolayer, where analytical solutions are not available, seems justified[8,13,14]. The finite lattice used in a Monte Carlo calculation is an asset in analyzing LEED data since the coherence width of the LEED beam allows the degree of order to be sampled over an area of only 50 to 200 Angstroms in diameter.

In this work, a 30x30 lattice with periodic boundary conditions is used to represent the binding sites on the surface. In the neighborhood of this lattice size, the shape of the I-T curve varies with lattice size only below $I/I_{max} \approx \frac{1}{2}$[12,13]. Therefore, as long as only the data for normalized intensities greater than ½ are used, the lattice size does not have to be treated as an additional parameter in the analysis.

Beginning with some given configuration of adatoms on the lattice, typically either a perfectly ordered array or an arrangement generated in an earlier trial, the adatoms are moved about on the lattice until an equilibrium configuration is reached. The hopping scheme used to move the adatoms in a Monte Carlo calculation does not have to be physically reasonable since only the final equilibrium configuration, and not the approach to equilibrium, is under consideration[12]. In this calculation, the hopping scheme is the following: A filled and an empty site are chosen at random. The energy for an adatom at each site and the distance between the sites are calculated. The probability, P, that the adatom will move to the empty site is then determined both by an arbitrary weighting factor in the distance and by the Boltzmann factor calculated from the energy difference between the sites and the temperature, i.e.,

$$P = e^{-\Delta E/kT} \, e^{-(d-1)/\lambda} \qquad (1)$$

where ΔE is the energy difference between the sites, d is the dimensionless distance between the sites (with the nearest neighbor distance set equal to unity), and λ is an arbitrary weighting factor which is related to the inelastic mean free path of the migrating adatom. Repeated trials showed that the magnitude of λ only affects the rate at which equilibrium is reached and not the nature of the equilibrium itself.

The total interaction energy and the (kinematic) LEED intensity of the initial configuration are calculated according to

$$E = \tfrac{1}{2}\sum_{i=1}^{30}\sum_{j=1}^{30} L(ij)\left\{N_1(ij)\varepsilon_1+N_2(ij)\varepsilon_2+N_3(ij)\varepsilon_3+N_4(ij)\varepsilon_4\right\} \qquad (2)$$

$$I^{(1)} = \left[\sum_{i=1}^{30}\sum_{j=1}^{30} L(ij)(-1)^i\right]^2/N^2 \qquad (3)$$

and

$$I^{(2)} = \left[\sum_{i=1}^{30}\sum_{j=1}^{30} L(ij)(-1)^j\right]^2/N^2 \qquad (4)$$

where L(ij) is unity for an occupied site and zero for an empty site, $N_a(ij)$ is the number of a^{th} neighbors of site (i,j), N is the number of adatoms on the surface, and $I^{(1)}$ and $I^{(2)}$ correspond to the intensities of the perpendicular domains.

Each time an adatom moves between sites, the changes in the total energy and in the LEED beam intensities are calculated. Plots of these variables as a function of the number of moves are used to determine when equilibrium has been reached. An example of such a construction is shown in Fig. 2. The existence both of a stable maximum in the intensity of one domain and a minimum in the energy are the criteria for determining the attainment of equilibrium. The configurations generated after approximately 6000 moves

in the calculation represented in Fig. 2 are considered equilibrium configurations. Since the values of energy and intensity vary even after equilibrium has been reached, it is necessary to average the values calculated for many configurations. Averaging the values for every configuration generated would bias the result since subsequent configurations are highly correlated[12]. To reduce this problem, the values for configurations separated by an average of one move per adatom (which corresponds to 450 moves at half-monolayer coverage) are averaged. Typically, 10 to 40 values are averaged for each calculated point.

Occasionally, arrangements of adatoms with coexisting domains are generated in the course of a simulation. Fig. 3a shows an example of a configuration with domains, and Fig. 3b shows an equilibrium configuration for the same temperature. Since there are unfavorable interaction energies only along the boundaries of the different domains and favorable interactions within the bulk of the domains, the increase in energy for domain formation is small, although the decrease in intensity is large. Furthermore, random motion of the adatoms will not favor one domain over the other. Therefore, configurations with domains are metastable and, once formed, will tend to persist. Fortunately, these configurations are easily identified either by viewing the plots of the intensity as a function of the number of moves or the configuration itself. Values for such configurations are not included in the averaging.

To determine the values of the interaction energies, Monte Carlo simulations of the equilibrium configuration as a function of temperature at half-monolayer coverage are made for many sets of parameters. The range of the ratios of the interaction energies tested, $\varepsilon_1:\varepsilon_2:\varepsilon_4$, is shown in Fig. 4.

The magnitude of the interaction energies scales directly with the transition temperature so that calculated I-T curves may be shifted easily to the correct transition temperature ($T \simeq 730$ K) for comparison with the experimental data. Once the scaling factors have been determined, I-T curves at quarter-monolayer coverage may be calculated for a cross section of the parameters tested at half-monolayer coverage.

4. Results and Discussion

A. Fit to Experimental Data

Of all the parameters tested, the only set which fits the experimental transition temperature at quarter-monolayer coverage ($T \simeq 480$ K) corresponds to the ratio

$$\varepsilon_1 : \varepsilon_2 : \varepsilon_4 = -1 : 5/6 : -1/3$$

the scaling factor is 2.09 kcal/mole, so that the set of interaction energies is

$$\varepsilon_1 = -2.1 \text{ kcal/mole}$$

$$\varepsilon_2 = \varepsilon_3 = +1.7 \text{ kcal/mole}$$

$$\varepsilon_4 = -0.7 \text{ kcal/mole}$$

Fig. 5 shows a plot of the experimental and the calculated I-T curves at fractional surface coverages of 0.53 and 0.25. The fit at $\theta = 0.53$ is good at all temperatures below the transition temperature. The calculated curve at quarter-monolayer coverage does not fit the data so well at low temperatures, but it does have the correct transition temperature.

A crude estimate of the uncertainties in the intensities calculated using the Monte Carlo simulations gives a value for the uncertainty in the

calculated transition temperatures of approximately ± 10 K for $\theta = 0.5$ and ± 20 K for $\theta = 0.25$. This leads to an uncertainty of about ± 10% in the interaction energies.

B. Uniqueness of the Parameters

Since only two transition temperatures were used to determine three parameters, the uniqueness of the parameters is an important question in spite of the rather large range of parameters tested. To investigate the possibility of nonuniqueness, a general relationship between the values of the parameters and the transition temperatures was sought.

At half-monolayer coverage, the energy change when an adatom moves from a perfection ordered position to the most favorable disordered site is given by

$$\Delta E_{\frac{1}{2}} = 3\varepsilon_2 - 4\varepsilon_4$$

When the parameters were scaled to give a transition temperatures of 726 K, it was found that all of the sets of parameters tested obeyed the equality

$$\Delta E_{\frac{1}{2}} = 8.0 \pm 0.2 \text{ kcal/mole} \qquad (5)$$

This relationship can be scaled, of course, to any desired transition temperature.

The energy change for an adatom moving out of an island to a vacant part of the surface, important at lower coverages, is

$$\Delta E_{\frac{1}{4}} = -(2\varepsilon_1 + 4\varepsilon_4)$$

Using values of the parameters determined at half-monolayer coverage, intensity versus temperature curves were simulated at quarter-monolayer coverage, and these used to determine the quarter-monolayer coverage

transition temperature. A construction of T_{tr} at $\theta = 0.25$ as a function of $\Delta E_{\frac{1}{4}}$ is shown in Fig. 6. The best straight line through the points, as determined by a weighted least squares fit, conforms to the equation

$$T_{tr}(\theta = 0.25) = (75 \pm 10 \frac{K}{kcal/mole})\Delta E_{\frac{1}{4}} - (36 \pm 64)K \qquad (6)$$

The large uncertainties are mainly due to the scatter in the calculated intensities at $\theta = 0.25$.

Therefore, it can be seen that insofar as the two relationships governing the values of the interaction energies are correct, the parameters are not unique.

The I-T curves shown in Fig. 5 are determined, however, completely by the transition temperatures at a quarter- and a half-monolayer coverage. Their shape is thus independent of the ratio of the values of the parameters used in their calculation.

C. Island Size and Shape

Any net attractive model for the interactions between adatoms, including the ones used in this and earlier studies,[5,8] predicts the occurrence of a single large island as the equilibrium configuration at low coverage, on a perfect lattice. This is, of course, not observed experimentally. At quarter-monolayer coverage, a uniform distribution of islands[5] with both domain orientations is observed. The reasons for this apparent conflict with the theoretical prediction include kinetic effects as well as the fact that the single crystal surface on which the measurements are made is not a perfect lattice. Kinetic effects, such as limited and random

diffusional motion, would hinder the union of the small islands. Imperfections in the crystal lattice, which are known to be important in the adsorption of oxygen on W(110),[4] would serve as sites for the nucleation of the many small islands and possibly also as barriers to growth of the islands beyond a certain size.

The model used in this study gives rise to elongated islands on a perfect lattice. If the islands of oxygen on W(110) are larger than the coherence width of the LEED beam, circular LEED spots, as observed experimentally, would result regardless of the shape of the island. If the islands are smaller than the coherence width of the beam,[5] then the islands would have to be approximately circular to give the observed spot shape. In this case, the model would be in apparent conflict with the physical evidence. This is not thought to be a fatal defect in the model, however, for two reasons. The first is that in view of the known strong effect of surface steps on domain formation for oxygen on W(110),[4] it seems likely that surface defects play a role in defining the observed island shape. The second is that, as mentioned in the discussion of the model, three-body effects[10,11] are important in adatom interactions. Three-body interactions could result in a change in the magnitude of the interactions parallel and perpendicular to the rows of oxygen atoms within a domain, giving rise to a spot shape different than that predicted by the model with only two-body interactions.

D. Energy, Heat Capacity and Entropy

The total interaction energy as a function of temperature was calculated

as described in the discussion of the method using the parameters of Sec. 4A. In addition, the heat capacity was calculated from the relationship

$$C_V = \frac{1}{kT^2}\left(\langle E^2\rangle - \langle E\rangle^2\right) \tag{7}$$

Since the heat capacity depends on the difference of two numbers of similar size, it is necessary to average a large number of values to reduce the uncertainty in the calculated values. From 90 to 280 points were averaged to determine each value of C_V. The calculated energy and heat capacity for half-monolayer coverage are shown in Fig. 6. In spite of some remaining scatter in the calculated points, the heat capacity curve has the expected shape with a maximum at the same temperature as the inflection in the energy curve.

It is also possible to determine the values of the average number of first, second and third neighbor pairs as a function of temperature from the Monte Carlo calculations. Making a simple extension of the quasi-chemical approximation,[6] it is possible to use these values to estimate the temperature dependent part of the entropy according to

$$\frac{S_Q}{k} = \ln\left[\frac{(2L^2)!^3}{(N_1)!(N_2)!(N_3)!\left(\frac{N_{10}}{2}\right)!^2\left(\frac{N_{20}}{2}\right)!^2\left(\frac{N_{30}}{2}\right)!^2(N_{100})!(N_{200})!(N_{300})!}\right] \tag{8}$$

where $N_{io} = 4\theta L^2 - 2N_i$, $N_{ioo} = N_i + 2L^2(1-2\theta)$, N_i is the number of i^{th} neighbor pairs, and L is the dimensionality of the lattice (30 unit cells in this case). A plot of S_Q as a function of temperature is shown in Fig. 7. The zero of this construction is arbitrary since a nontemperature dependent term in the entropy has been omitted.

The plot of quasichemical entropy as a function of temperature is dependent only on the transition temperature at half-monolayer coverage and thus will not be affected by the nonuniqueness of the parameters. The upper asymptote of the energy curve

$$E(T = \infty) = \frac{1}{2}(2\varepsilon_1 + 2\varepsilon_2 + 2\varepsilon_4)$$

is not determined completely by Eqns. (5) and (6). Therefore, the energy curve is dependent on the ratio of the values of the parameters, i.e. it is not a unique function of the transition temperatures at half- and quarter-monolayer coverage.

5. Conclusions

General expressions relating the values of the interaction energies to the transition temperatures for a lattice gas with first, second and third neighbor interactions have been determined. A nonunique set of parameters which fit the experimental data for oxygen chemisorbed on W(110) were calculated and used to generate representative I-T, E-T, C_v-T and S-T curves. The importance of using both a physically and theoretically reasonable model to described adatom interactions has been emphasized and is an important ingredient in the calculations.

Acknowledgment

This work was supported by the Army Research Office (Durham) under grant # DAHC04-75-0170.

References

1. J. C. Tracy and J. M. Blakely, Surface Sci. 15, 257 (1969).

2. J. C. Buchholz and M. G. Lagally, Phys. Rev. Letters 35, 442 (1975).

3. T. Engel, H. Niehus and E. Bauer, Surface Sci. 52, 237 (1975).

4. T. Engel, T. Von Dem Hagen and E. Bauer, Surface Sci. 62, 361 (1977).

5. T.-M. Lu, G.-C. Wang and M. G. Lagally, Phys. Rev. Letters 39, 411 (1977).

6. T. L. Hill, Statistical Mechanics, McGraw-Hill, New York, 1956.

7. M. A. Van Hove and S. Y. Tong, Phys. Rev. Letters 35, 1092 (1975).

8. G. Ertl and D. Schillinger, J. Chem. Phys. 66, 2569 (1977).

9. T. L. Einstein and J. R. Schrieffer, Phys. Rev. B7, 3629 (1973).

10. T. L. Einstein, Phys. Rev. B 16, 3411 (1977).

11. A. M. Stoneham, Solid State Commun. 24, 425 (1977).

12. D. P. Laudau, Phys. Rev. B13, 2997 (1976).

13. G. Doyen, G. Ertl and M. Plancher, J. Chem. Phys. 62, 2957 (1975).

14. G. Ertl and M. Plancher, Surface Sci. 48, 364 (1975).

Figure Captions

Fig. 1: Schematic representation of the p(2x1) overlayer of oxygen on W(110) as determined by LEED along with two models for the oxygen-oxygen interaction energies: (1) ε_1, ε_2, ε_3 and ε_4 (ε_1, ε_4 <0 and ε_2, ε_3 >0) which are used in this work. Although not explicitly indicated in the figure, the 4th neighbor interaction in the ± (1,0) as well as the ± (0,1) directions is included. (2) ε_a, ε_b and ε_{2b} (ε_a, ε_{2b}<0 and ε_b>0) which were used in refs. 5 and 8.

Fig. 2: Energy (-□-) and intensity of the perpendicular domains (-Δ,0-) as a function of the number of moves.

Fig. 3: Configuration with perpendicular domains (a), and equilibrium configuration (b) generated at the same temperature.

Fig. 4: The range of ratios of the parameters ε_1, ε_2 and ε_4 for which I-T curves were calculated. The pairs ($|\varepsilon_2/\varepsilon_1|$, $\varepsilon_4/\varepsilon_1$) = (1,1.5) and (1,2.0) were also tested.

Fig. 5: Intensity of the (½,0) LEED beam for W(110) - p(2x1)O as a function of temperature for two different surface coverages. The theoretical curve calculated using ε_1 = -2.1 kcal/mole, $\varepsilon_2 = \varepsilon_3$ = +1.7 kcal/mole and ε_4 = -0.7 kcal/mole is compared with the experimental data from ref. 5.

Fig. 6: Transition temperature at quarter-monolayer coverage as a function of the energy difference, $\Delta E_{\frac{1}{4}} = -(2\varepsilon_1 + 4\varepsilon_4)$. The straight line corresponds to the weighted least squares fit of the points.

Fig. 7: Calculated total interaction energy (—O—) and heat capacity (--□--) as a function of temperature for θ = 0.5.

Fig. 8: Temperature dependent part of the entropy for $\theta = 0.5$, calculated using the quasichemical approximation. The zero of the entropy scale is arbitrary.

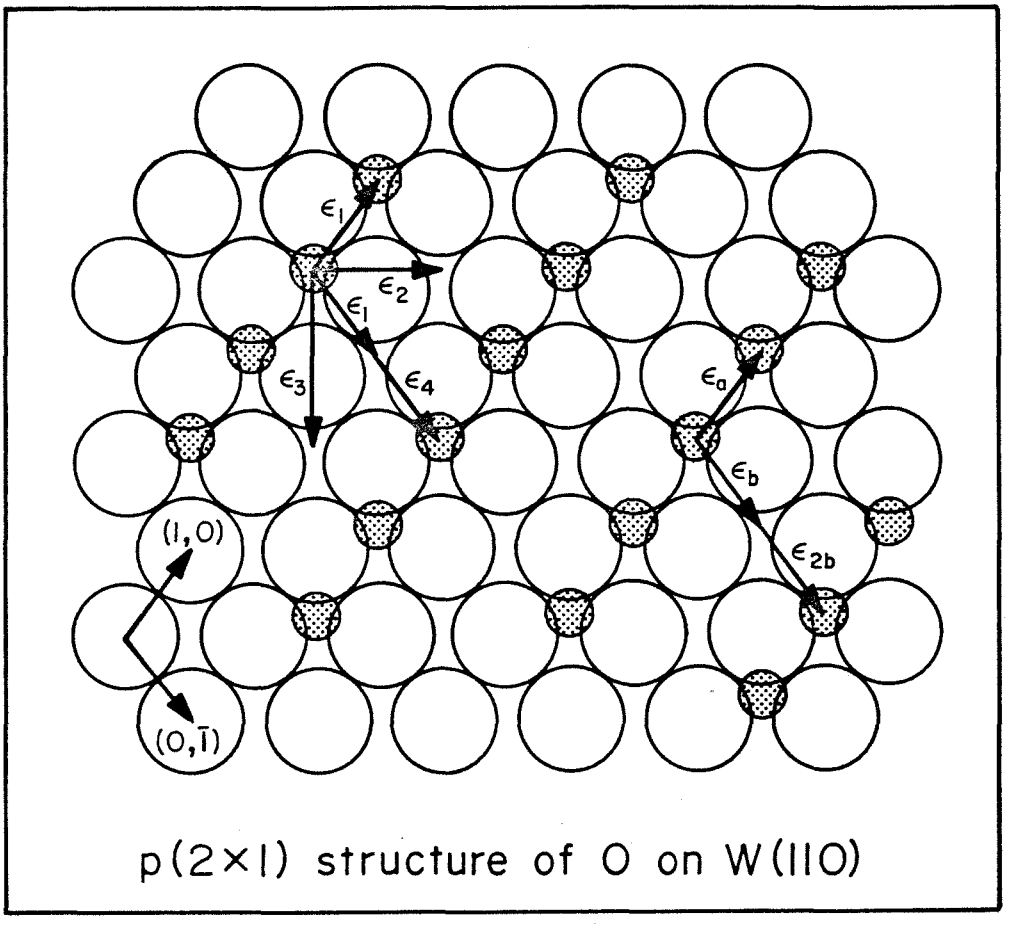
ϵ_1
ϵ_2
ϵ_1
ϵ_3
ϵ_4
ϵ_a
ϵ_b
ϵ_{2b}
(1,0)
(0,$\bar{1}$)
p(2×1) structure of O on W(110)

Fig.1

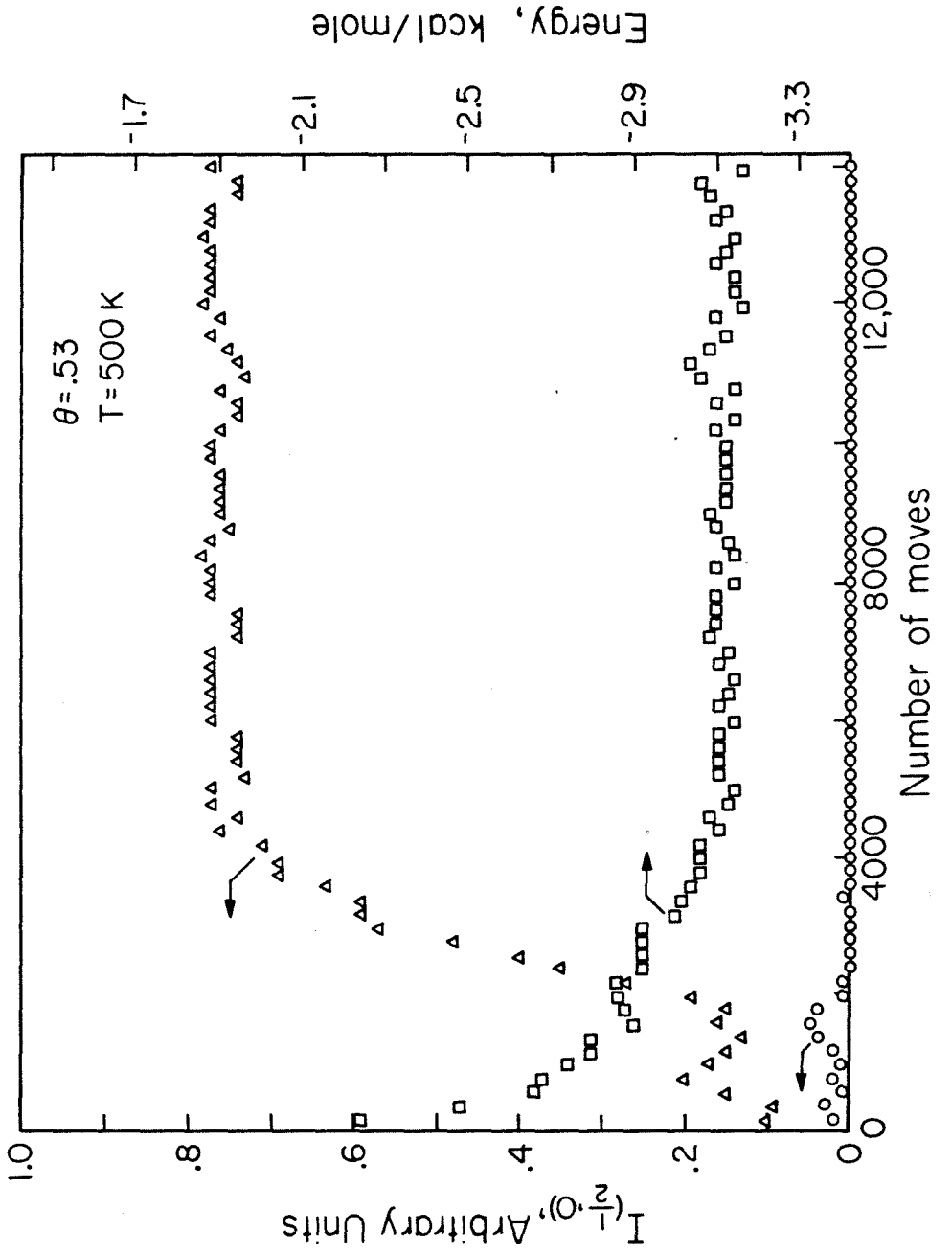
Energy, kcal/mole
-1.7
-2.1
-2.5
-2.9
-3.3
θ=.53
T=500 K
1.0
.8
.6
.4
.2
0
$I_{(\frac{1}{2},0)}$, Arbitrary Units
0
4000
8000
12,000
Number of moves

Fig. 2

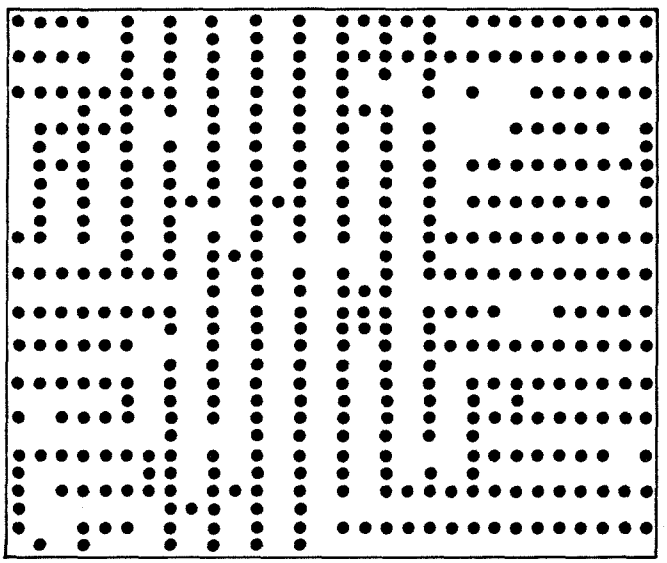

(a)

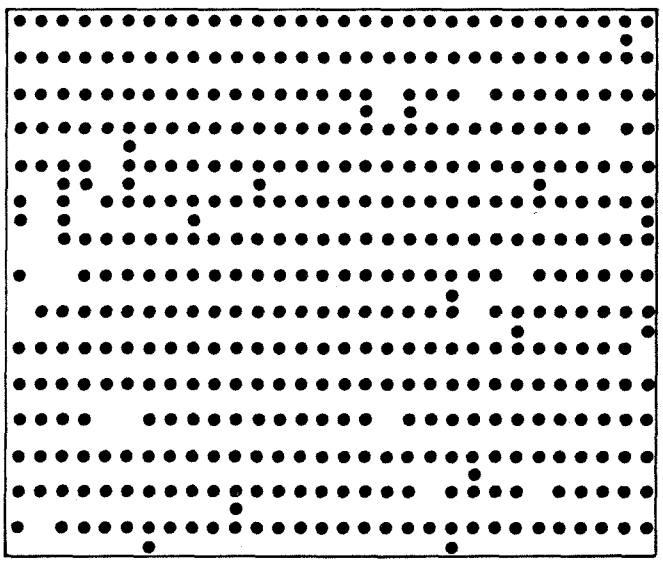

(b)

Fig. 3

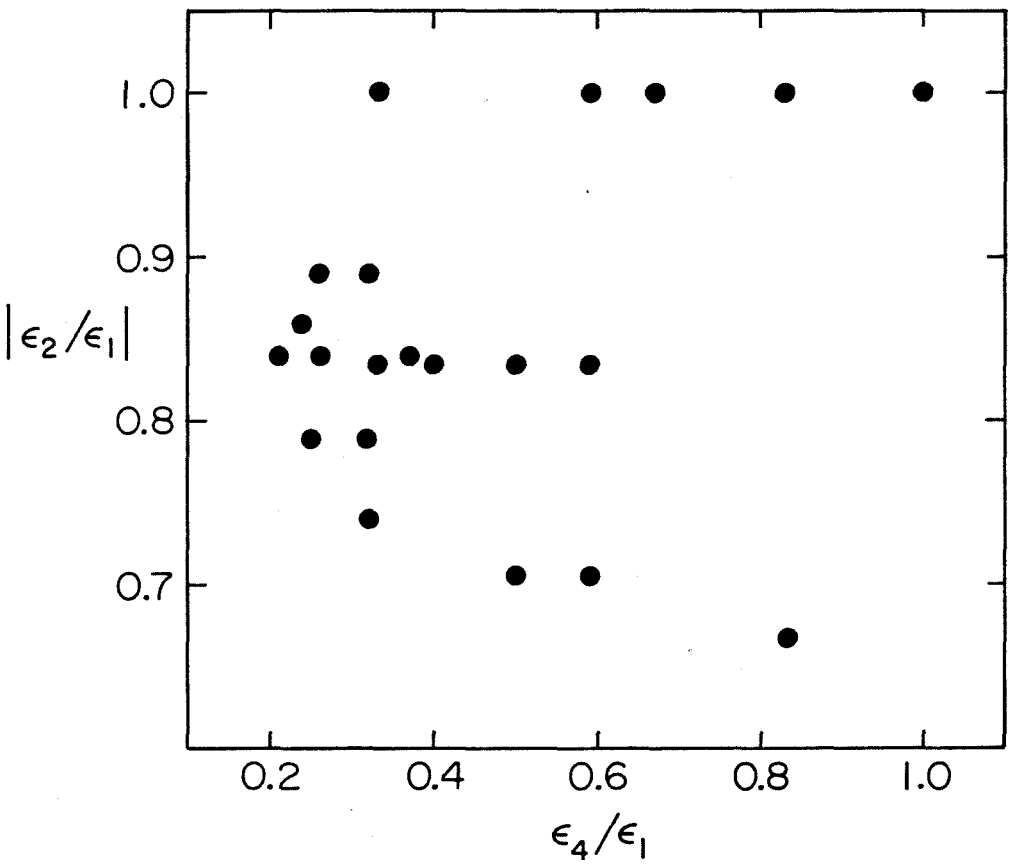
1.0
0.9
0.8
0.7
$|\epsilon_2/\epsilon_1|$
0.2
0.4
0.6
0.8
1.0
ϵ_4/ϵ_1

Fig. 4

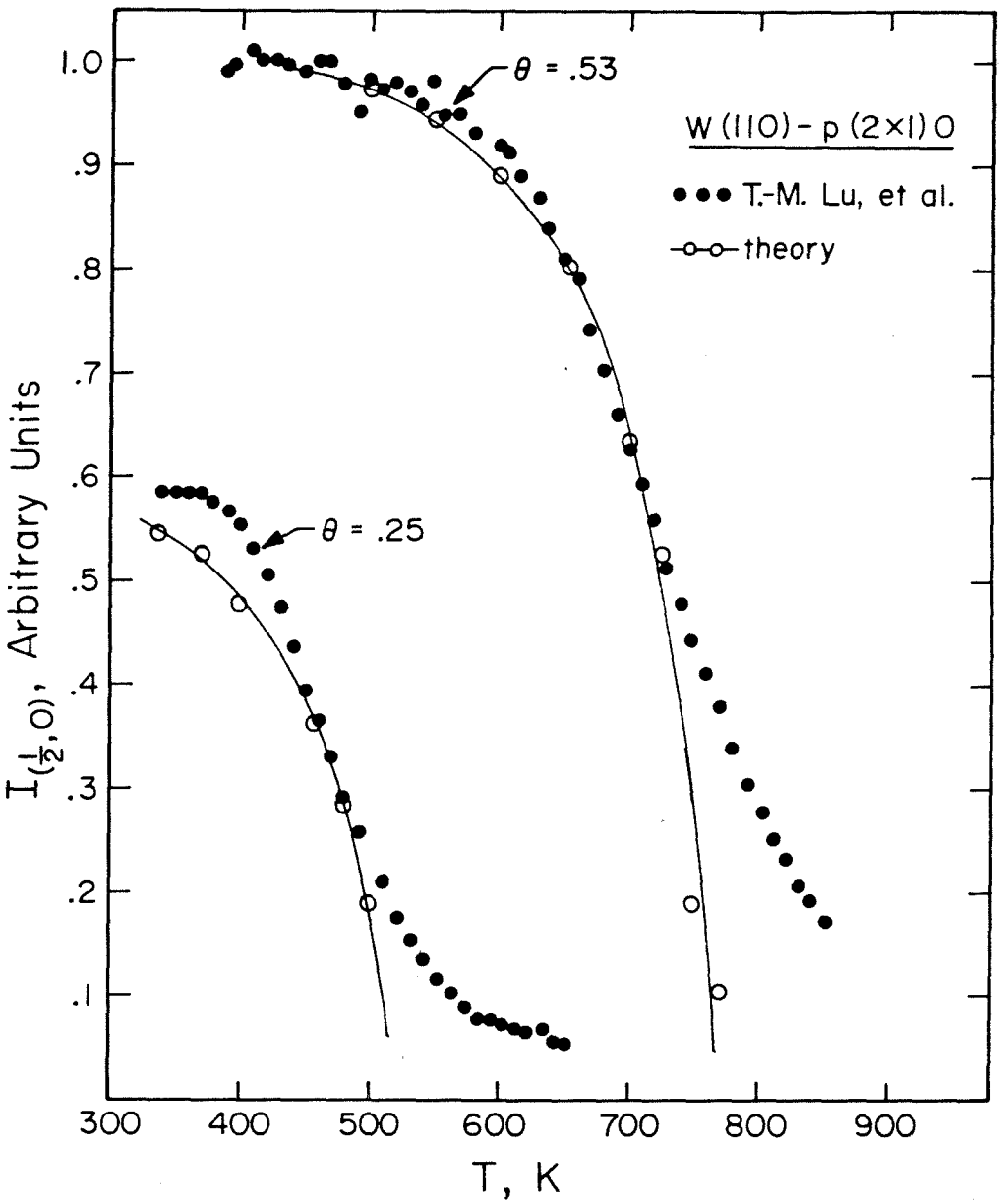
W (110) - p (2×1) O
T.-M. Lu, et al.
theory
θ = .53
θ = .25
$I_{(\frac{1}{2},0)}$, Arbitrary Units
T, K
1.0
.9
.8
.7
.6
.5
.4
.3
.2
.1
300
400
500
600
700
800
900

Fig. 5

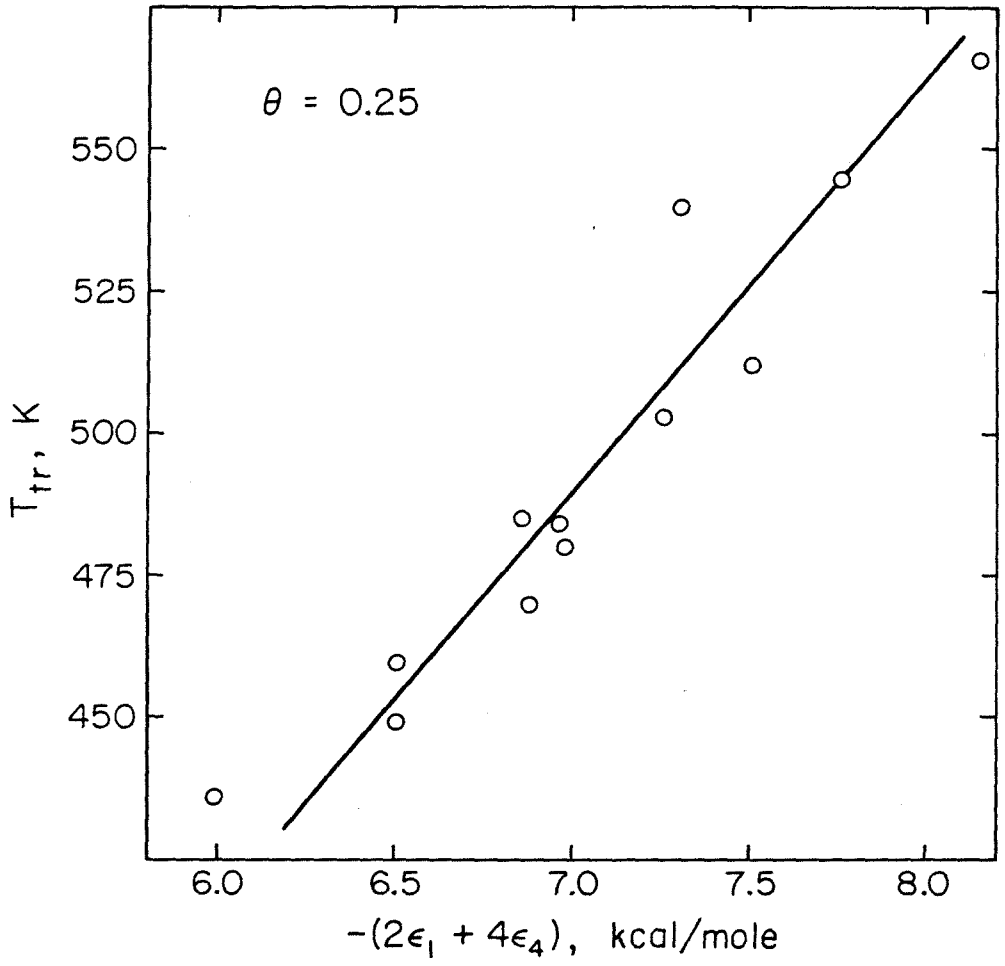
θ = 0.25
550
525
500
475
450
T_{tr}, K
6.0
6.5
7.0
7.5
8.0
$-(2\epsilon_1 + 4\epsilon_4)$, kcal/mole

Fig. 6

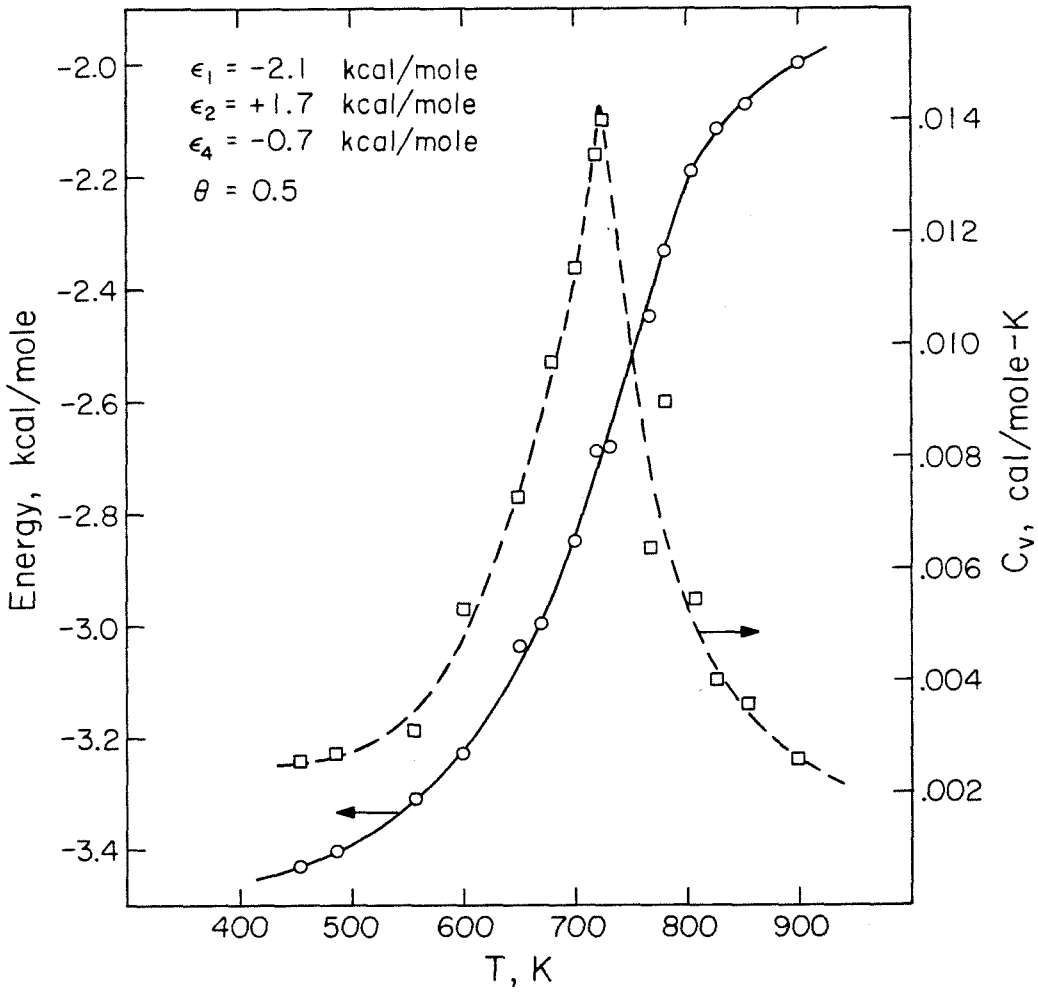
ϵ_1 = -2.1 kcal/mole
ϵ_2 = +1.7 kcal/mole
ϵ_4 = -0.7 kcal/mole
θ = 0.5
-2.0
-2.2
-2.4
-2.6
-2.8
-3.0
-3.2
-3.4
Energy, kcal/mole
.014
.012
.010
.008
.006
.004
.002
C_v, cal/mole-K
400
500
600
700
800
900
T, K

Fig. 7

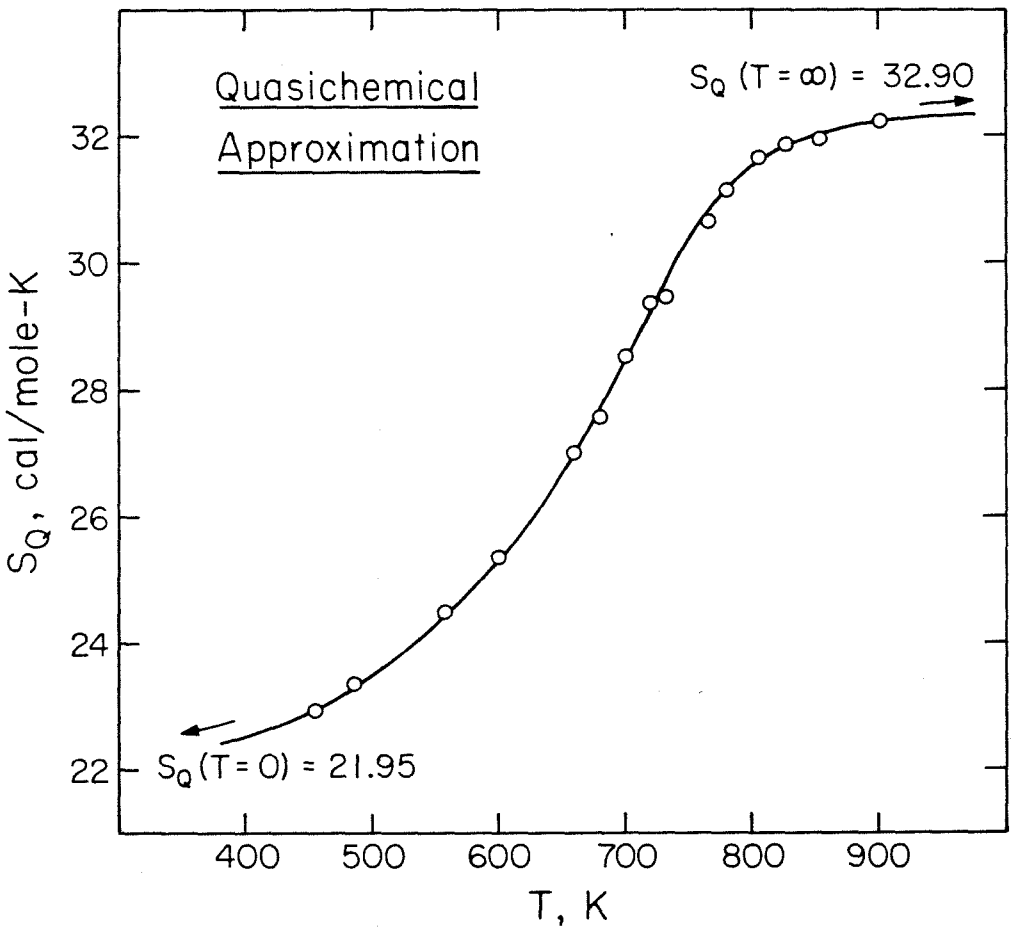
Quasichemical
Approximation
S_Q (T = ∞) = 32.90
S_Q (T = 0) = 21.95
S_Q, cal/mole-K
T, K
22
24
26
28
30
32
400
500
600
700
800
900

Fig. 8

Section III

Segregation of Co-Adsorbed Species: Hydrogen and Carbon Monoxide on the (111) Surface of Rhodium

[This section was published as a paper by E. D. Williams, P. A. Thiel, W. H. Weinberg and J. T. Yates, Jr. in *The Journal of Chemical Physics* 72, 3496 (1980).]

Abstract

The co-adsorption of CO and H_2 on Rh(111) at low temperature ($\sim$ 100 K) has been studied using thermal desorption mass spectrometry (TDS) and Low-Energy Electron Diffraction (LEED). The probability of adsorption of CO on rhodium pretreated with hydrogen has been found to vary nonlinearly with the amount of hydrogen on the surface. In addition, the effect of surface hydrogen on the CO LEED patterns indicates segregation of hydrogen and CO. These results can be explained qualitatively in terms of a strong repulsive CO-hydrogen interaction and a mobile precursor model of CO adsorption.

1. Introduction

The mechanism of the catalytic reaction of CO and hydrogen in the Fischer-Tropsch and methanation reaction has been a topic of continued interest and dispute (1,2). Of the two commonly posited reaction intermediates, one, an active form of surface carbon, has been discredited for some time in favor of the other, a hydrogen-CO surface complex. Recent work, however, has shown that surface carbon, formed by dissociation of CO under reaction conditions, is much more readily hydrogenated to methane than is molecular CO (3-9). At the same time, there is increasing evidence to suggest that surface complexes of CO and hydrogen do exist (10 - 12) and that direct hydrogenation of molecular CO is an alternate route to hydrocarbon formation (3). Apparently, both types of intermediates do occur, possibly with different effects on the product distribution. This duality may explain the diversity of activity and selectivity among the transition metals that catalyze the methanation and Fischer-Tropsch reactions. If there is a competition between the two sequences of elementary reactions, then the varying ability of different metals to promote CO dissociation as opposed to formation of hydrogen-CO complexes will give rise to a different extent of the reaction proceeding by each mechanism. The product distribution due to each mechanism individually, as well as that due to interactions among the different types of intermediates, then should give rise to an overall product distribution characteristic of the metal.

In order to understand better the fundamental processes governing the formation of hydrogen-CO complexes, the interaction of co-adsorbed hydrogen

and CO on Rh(111) has been studied under conditions where reaction does not occur. The individual chemisorption of hydrogen and CO has been studied previously and is well characterized (13 - 15). Hydrogen adsorbs dissociatively and forms no ordered structures observable by LEED. Hydrogen desorbs with an activation energy of 19 kcal/mole at zero coverage. On the other hand, CO adsorbs molecularly and forms three ordered super-structures at 100 K. These are a weak primitive (2x2) at θ_{CO} = 1/4 ($\theta_{CO} \equiv$ the number of CO molecules per surface rhodium atom), a $(\sqrt{3} \times \sqrt{3})R30^{o}$ at θ_{CO} = 1/3, and a (2x2) with three CO molecules per unit cell at θ_{CO} = 3/4 which is the saturation coverage. The activation energy for the desorption of CO is 32 kcal/mole in the limit of zero coverage.

The catalytic behavior of supported and polycrystalline rhodium has been studied also (8,16). Rhodium has somewhat lower activity for the methanation reaction than nickel, but similar selectivity. CO apparently dissociates on polycrystalline Rh under the reaction conditions (575 K and one atmosphere) and surface carbon is implicated as a reaction intermediate (8).

2. Experimental Details

The experiments were performed in a stainless steel ultra-high vacuum system equipped with ion pumps and titanium sublimation pumps. Following bakeout, the base pressure was below 1×10^{-10} torr. The system is equipped with four-grid LEED optics and a moveable Faraday cup in which the diameter of the aperture is 1.5 mm. The Faraday cup can be used to monitor the intensity of a diffracted LEED beam continuously as a function

of exposure. The system also contains a quadrupole mass spectrometer and a single pass cylindrical mirror Auger electron spectrometer.

Experiments were performed with two different Rh crystals, cut from the same boule. The Rh surfaces were oriented, cut and polished to within 1^{o} of the (111) orientation using standard methods. The polished crystals were spotwelded to two parallel 0.025 cm diameter Ta heating wires that were clamped in a Cu holder. Thermocouple leads of 5%Re/95%W and 26%Re/74%W were spotwelded together on a small piece of Ta foil on the crystal surface to make a junction. The crystal could be cooled to 90 K using liquid nitrogen refrigeration, and heated to above 1600 K resistively. The thermocouple calibration of Sandstrom and Withrow (17) was used below 273 K.

Initial contaminants of P, B, S and C were depleted from the near surface region by a combination of ion bombardment and oxygen treatment as described previously (18). The continued cleanliness of the surface following numerous thermal desorption experiments involving both CO and H_2 was monitored using AES.

Hydrogen and CO pressures during adsorption were measured with a Bayard-Alpert gauge. All exposures are expressed in Langmuirs (1 Langmuir $\equiv$ 1 L $\equiv 10^{-6}$ torr-s) and were calculated using the appropriate gauge sensitivities for H_2 and CO. Following exposure to a gas, the sample chamber was again evacuated to the base pressure of approximately 10^{-10} torr.

Thermal desorption experiments were performed using a heating rate of approximately 20 K per second and with the crystal positioned in line of

site of the mass spectrometer. Desorption of CO from the cold Cu support caused a gradually increasing background during CO desorption experiments. This background was estimated as linearly increasing below the desorption peaks in order to determine peak areas.

LEED experiments were performed using as low a beam flux as possible (0.1 - 0.2 $\mu A/mm^2$) to minimize electron beam induced desorption and/or dissociation.

3. Results and Analysis

Thermal desorption mass spectrometry (TDS) and low-energy electron diffraction (LEED) were used to characterize the co-adsorption of hydrogen and CO. TDS of H_2 was used to determine the relative coverage ($\hat{\theta}_H \equiv$ the fraction of the saturation coverage of hydrogen) as a function of exposure and the activation energy of desorption for H_2 from clean and CO covered rhodium. TDS of CO provided coverage-exposure relationships for CO adsorption onto surfaces pre-exposed to varying amounts of hydrogen. In addition, the coverage-exposure behavior was analyzed to determine the adsorption mechanism of CO. LEED was used to correlate the relative coverages of CO ($\hat{\theta}_{CO}$) determined by TDS with absolute coverages (θ_{CO}). The geometric structure of co-adsorbed layers of CO and hydrogen was studied by monitoring the intensity of the LEED patterns due to CO as a function of exposure to both hydrogen and CO.

A. Thermal Desorption of Hydrogen

The relative coverage of hydrogen as a function of exposure as determined from the areas under thermal desorption peaks, is shown in Fig. 1 for

adsorption at 100 K. The upper curve (drawn empirically) represents adsorption onto the clean surface; the lower, adsorption onto a surface covered with 0.21 monolayer of CO. The presence of CO causes the probability of adsorption of hydrogen to decrease much more rapidly than for adsorption onto a clean surface. However, the approach to saturation is much slower on the CO covered surface, and saturation does not appear to be achieved even after an exposure to 20 L of H_2. At a higher initial coverage of CO (θ_{CO} = 0.42), less than a tenth of a monolayer of hydrogen adsorbs during an exposure to 4 L of hydrogen. This indicates that even a moderate coverage of CO is highly efficient in blocking hydrogen adsorption.

The amount of CO desorbed from the co-adsorbed layer is constant within experimental uncertainty for constant initial coverages of CO and varying exposures to hydrogen. This indicates that hydrogen does not displace CO and that, to within a few percent, no reaction products due to CO + H are formed under these conditions, as expected (8).

Co-adsorption with CO decreases the desorption temperature of H_2 markedly. The results of an analysis of the desorption parameters for hydrogen on clean and CO covered Rh(111) by the method of Chan et al. (19) are shown in Fig. 2. The values calculated for the clean surface are in full agreement with previous results (13). The apparent energy of desorption from the CO covered surface is 1.5 to more than 3 kcal/mole lower than from the clean surface. The pre-exponential factor for the CO-covered surface will depend on the effective saturation density of hydrogen, n_s, in

the presence of CO. For instance, if the saturation coverage of hydrogen on the surface precovered with 0.21 monolayer of CO were 0.6 hydrogen atoms per rhodium atom, then the limiting value of the pre-exponential factor would be of magnitude 10^{-1} cm^2/s. However, the values calculated for desorption from the co-adsorbed system can be treated only as "apparent" parameters. A correct treatment of the changing nature of the mixed overlayer structure as H_2 desorbs would require a much more complex analysis than performed here.

B. Thermal Desorption of CO

No change in the activation energy of desorption for CO was observed upon co-adsorption with hydrogen. This result is not surprising since hydrogen desorbs at a lower temperature than CO.

In Fig. 3, the coverage-exposure relationship is shown for CO adsorption onto a surface precovered with increasing amounts of hydrogen. The most striking aspect of these data is the decrease in the initial probability of adsorption of CO with increasing hydrogen coverage and the extended linear dependence of CO coverage on exposure indicated by the dashed lines for each set of data. The saturation coverage of CO($\hat{\theta}_s$) decreases linearly with increasing amounts of hydrogen on the surface, as might be expected. Surprisingly, the initial slopedecreases nonlinearly with increasing hydrogen coverage. The values of the saturation coverage of CO and the initial slope for each initial coverage of hydrogen are listed in Table 1.

Measurements of the amount of hydrogen on the surface following expos-

ure to CO shows that there is a gradual loss of hydrogen with increasing coverage of CO. This loss is most severe for high initial coverages of hydrogen, where as much as a quarter of a monolayer of hydrogen is displaced.

To understand the mechanism of adsorption of CO, the expected behavior according both to first-order Langmuir and to mobile precursor (20) adsorption kinetics has been compared. To do this, both models were modified to account for the presence of hydrogen on the surface. This modification is very simple in the case of Langmuir kinetics, which predicts that the probability of adsorption is directly proportional to the number of empty sites. In adsorption onto a clean surface,

$$\frac{d\hat{\theta}}{d\varepsilon} \alpha \left(1 - \hat{\theta},\right)$$

where ε is the exposure. When hydrogen is present, the number of available sites is reduced according to

$$\frac{d\hat{\theta}}{d\varepsilon} \alpha \left(\hat{\theta}_s - \hat{\theta} \right)$$

where

$$\hat{\theta}_s = 1 - a\hat{\theta}_H$$

and a is a constant of proportionality.

A description of the mobile precursor model and details of the derivation of the kinetics of adsorption for the clean and hydrogen covered surface using this model are given in the Appendix. The result is

$$\frac{d\hat{\theta}}{d\varepsilon} \propto c_1 \frac{\left(\hat{\theta}_s - \hat{\theta}\right)}{\left(c_2 + \hat{\theta}_s - \hat{\theta}\right)}$$

A comparison of the behavior of the two models in the limit of zero coverage of CO yields the following:

Langmuir $\lim_{\hat{\theta} \to 0} \frac{d\hat{\theta}}{d\varepsilon} \propto \hat{\theta}_s$

Mobile Precursor $\lim_{\hat{\theta} \to 0} \frac{d\hat{\theta}}{d\varepsilon} \propto \frac{\hat{\theta}_s}{\left(c_2 + \hat{\theta}_s\right)}$

The nonlinear dependence of the limiting slope on the saturation coverage predicted by the mobile precursor model is a result of the possibility of the desorption of physically adsorbed CO from above sites occupied by hydrogen atoms.

The two models were fit to the data for adsorption of CO onto the clean surface. Using the parameters estimated from this fit, the coverage-exposure relationships are the following.

Langmuir $$\frac{d\hat{\theta}}{d\varepsilon} = 0.4(\hat{\theta}_s - \hat{\theta})$$

Mobile Precursor $$\frac{d\hat{\theta}}{d\varepsilon} = 0.525 \left(\frac{\hat{\theta}_s - \hat{\theta}}{0.5 + \hat{\theta}_s - \hat{\theta}} \right)$$

where $\hat{\theta}_s$ is the measured relative saturation coverage of CO for the given initial coverage of hydrogen. These equations were used without change to calculate the coverage-exposure behavior for adsorption onto a hydrogen precovered surface. The calculated behavior is shown with the full range of the data for initial hydrogen coverages of 0.0 and 0.58 in Fig. 4. For

adsorption onto the clean surface, the Langmuir model fails to agree with the data in the coverage range 0.6 - 0.9. The mobile precursor model agrees somewhat better, except that it predicts a more rapid approach to saturation above $\hat{\theta}_{CO} = 0.9$ than is observed. This could be due to the close packing of the CO molecules at this coverage which might change the probability of adsorption into an "open" site. For an initial hydrogen coverage of 0.58, using the parameters determined for the clean surface, the mobile precursor model is clearly much more successful in fitting the data than the Langmuir model. The quality of agreement for the other initial coverages of hydrogen is similar.

A major factor in the poor agreement of the Langmuir model is that it predicts too rapid a decrease in the initial slope. A comparison of the apparent initial slopes (calculated in the low coverage region of the theoretical curves which would appear linear within experimental uncertainty) for both models with the data is shown in Fig. 5. While neither model agrees quantitatively with the data, the mobile precursor model is more successful qualitatively in predicting the gradual non-linear dependence of intial slope on saturation coverage.

The mobile precursor model used here is obviously too simple to describe completely the complex co-adsorption system. To model this system correctly, the shifting geometric structure of the CO overlayer with coverage, the displacement of hydrogen, and the possibility of different desorption probabilities for CO physically adsorbed above sites occupied by hydrogen or by CO would have to be taken into account. However, the level

of agreement with even this simple model strongly supports the basic assumption of a physically adsorbed mobile precursor to adsorption.

Gorte and Schmidt (21) have shown that desorption via a "mobile precursor" intermediate can lead to a strong decrease in desorption temperature with increasing coverage for first-order desorption under some conditions. Since, by the principle of microscopic reversibility, adsorption and desorption must occur by the same elementary steps, this could explain the apparent, strong dependence of desorption energy and pre-exponential factor on coverage previously observed for CO on Rh(111) (14).

C. LEED

Intensity-exposure measurement of the three LEED patterns [p(2x2), $(\sqrt{3} \times \sqrt{3})R30^{o}$ and high coverage (2x2), hereafter referred to as (2x2)] observed for CO adsorption on Rh(111) at 100 K have been reported previously (14). The p(2x2) was not discussed before. Further observation confirms that, though very weak, it is a reproducible feature of CO adsorption. It increases in intensity steadily from zero coverage suggesting island formation. For a p(2x2) superstructure, island formation is the result of an attractive third neighbor CO-CO interaction. The decrease in intensity of the p(2x2) structure is concomitant with the development of the $(\sqrt{3} \times \sqrt{3})R30^{o}$ structure ($\sqrt{3}$ structure), and a superposition of the two patterns is briefly visible. The p(2x2) reaches maximum intensity at θ_{CO} = 0.23, slightly less than the value of 0.25 expected for a p(2x2) structure. This is probably due to local development of the $\sqrt{3}$ structure before the surface is completely covered by the p(2x2) structure.

No new LEED patterns were observed for co-adsorbed hydrogen and CO. However, the clean surface CO structures do form, under some circumstances, with modified intensity during co-adsorption. The effect of exposing the different CO superstructures to hydrogen and the formation of the CO superstructures on hydrogen covered surfaces have been investigated by monitoring the intensity of the LEED beams as a function of exposure to either hydrogen or CO.

Addition of hydrogen to the fully ordered (θ_{CO} = 0.23) p(2x2) structure causes a rapid decrease in intensity of the p(2x2) pattern. Similarly, addition of hydrogen to the fully ordered (θ_{CO} = 0.35) $\sqrt{3}$ structure causes a loss in intensity of the $\sqrt{3}$ pattern. Clearly, hydrogen atoms cannot occupy a position within either the p(2x2) or the $\sqrt{3}$ unit cell without perturbing the neighboring CO molecules.

The effect of hydrogen on the $\sqrt{3}$ structure for coverages of CO less than one-third is illustrated in Fig. 6. The dashed line shows the intensity-exposure behavior for CO adsorption on the clean surface. If exposure to CO is terminated before maximum ordering occurs, and followed by exposure to hydrogen, the solid curves result. At θ_{CO} = 0.25 and 0.30, hydrogen increases the amount of the ordered $\sqrt{3}$ structure on the surface. At θ_{CO} = 0.21, where only the p(2x2) CO structure is present, addition of hydrogen causes a transformation from the p(2x2) to the $\sqrt{3}$ structure. The maximum intensities obtained by addition of hydrogen are less than the maximum reached for CO adsorption above. The asymmetric decrease in intensity with hydrogen exposure beyond the maxima is due to the decreasing

probability of adsorption of hydrogen (cf., Fig. 1).

Addition of hydrogen to the partially ordered ($\theta_{CO} < 0.23$) p(2x2) structure does not increase the order as for the $\sqrt{3}$ structure. Rather, there is a steady loss of intensity which is slower for lower coverages of CO.

Exposure to hydrogen caused no change in intensity of the partially ordered ($\theta_{CO} = 0.5$ and 0.7) (2x2) structure. This may be due to the small probability of adsorption of hydrogen when a high coverage of CO is present.

The adsorption of CO onto a hydrogen precovered surface mimics adsorption onto the clean surface, as shown in Figs. 7 and 8. In both figures, curve (a) represents the intensity-exposure behavior for adsorption onto the clean surface. Curves (b) - (e) are for CO adsorption onto a surface covered with increasing amounts of hydrogen. As on the clean surface, on a hydrogen-covered surface, CO first forms a p(2x2) structure which is quickly transformed to a $\sqrt{3}$ structure. Then the final (2x2) structure is formed by continuous compression of the $\sqrt{3}$ structure. However, on the hydrogen covered surface, the CO structures form at lower coverage and with lower intensity than on the clean surface.

4. Discussion

A. Physical Nature of the Co-Adsorbed Overlayers

The LEED results indicate that the structure of the mixed overlayer is considerably different depending on the order of adsorption of hydrogen and CO. The results of the thermal desorption experiments, together with the intensity-exposure behavior give a consistent picture of the co-adosrbed system.

In the case where CO is adsorbed first, followed by hydrogen, it has been seen that hydrogen disrupts both the p(2x2) and the $\sqrt{3}$ unit cells for CO. Yet, while hydrogen decreases the order of a partially ordered p(2x2) overlayer, it increases the order of the $\sqrt{3}$ structure for θ_{CO} less than one-third. The destruction of the p(2x2) CO structure occurs because of the hydrogen induced transformation to the $\sqrt{3}$ structure. This raises the question of how hydrogen causes the transformation. If a hydrogen atom scattered electrons identically to a CO molecule (which is highly unlikely), addition of hydrogen could cause the transformation in the same way as addition of CO. However, in this case, addition of hydrogen should cause a maximum intensity equal to that for CO only, which is not observed. A second possibility is that a hydrogen atom attracts nearby CO molecules into a $\sqrt{3}$ structure around it. This requires that a hydrogen atom can occupy a $\sqrt{3}$ unit cell of CO without disturbing it, which is not the case. The final possibility, which is consistent with the experimental evidence, is that a hydrogen atom added to a p(2x2) structure repels the nearby CO molecules. To reduce the repulsive interaction, the CO molecules move away, causing a local increase in density of CO and transformation to the higher density $\sqrt{3}$ structure. As more hydrogen is added to the overlayer, a significant surface area will be covered by the $\sqrt{3}$ structure. Some hydrogen undoubtedly will then adsorb within the $\sqrt{3}$ areas, although the sticking probability for hydrogen should be lower in regions of higher density of CO, disrupting the $\sqrt{3}$ structure. Thus, the maxima in the solid curves in Fig. 6 probably do not correspond to complete ordering of CO in the $\sqrt{3}$ structure.

The nature of the CO-hydrogen repulsive interaction is of some

interest. If addition of hydrogen to the p(2x2) structure only disrupted the attractive third neighbor CO-CO interaction responsible for the p(2x2), disordering of the p(2x2) structure but not transformation to the $\sqrt{3}$ structure would occur. A true repulsion between hydrogen and CO is required to cause the transformation. The existence of a true repulsive interaction is confirmed by the decrease in activation energy of desorption for hydrogen added to a CO overlayer.

Geometrically, a hydrogen atom can be placed in the p(2x2) CO unit cell in a position 3.1 Å from each of three CO molecules or 2.7 Å from each of two CO molecules. The hard core radius of CO, determined from the distance of closest approach in the saturation structure is 1.55 Å (14). The radius of a chemisorbed hydrogen atom is probably less than 0.75 Å (22). Thus, the repulsive interaction between hydrogen and CO, at low coverages, must be a through-metal effect (23,24) rather than the result of orbital overlap.

When CO is added to a hydrogen precovered surface, initial formation of the p(2x2) structure occurs readily. The intensity of the p(2x2) pattern for CO added to a hydrogen covered surface is compared to that for CO on a clean surface in Fig. 9. The smooth curve is the clean surface behavior. The points represent the maximum intensity for CO added to a surface with different coverages of hydrogen as in curves (b) - (e) of Fig. 7. The decrease in intensity for the mixed overlayer corresponds to less than 0.03 monolayer more disordered CO than on the clean surface for each precoverage of hydrogen. The amount of hydrogen on the surface (0.26 to 0.92 monolayer) would be enough to prevent the formation of any p(2x2) CO structure, if it were distributed uniformly.

The fact that p(2x2) CO structures do form with intensity comparable to that on the clean surface indicates that there is segregation of hydrogen and CO.

The transformation of the p(2x2) CO structures on the hydrogen covered surfaces to $\sqrt{3}$ and then (2x2) structures undoubtedly takes place via addition of CO to the already existing ordered p(2x2) regions. At the same time, it is reasonable to assume that some CO adsorbs in regions of high hydrogen density in a random configuration that does not contribute to the LEED intensity.

In Table 2, the coverages of CO at which the three structures reach maximum intensity are listed for different precoverages of hydrogen. In addition, the ratios of the coverages for the $\sqrt{3}$ to the p(2x2) and the (2x2) to the $\sqrt{3}$ structures are shown. On the clean surface, these ratios should ideally be 1.33 and 2.25, respectively. The experimental values for the clean surface are rather close to what is expected. Since both the number of disordered CO molecules and the excluded area they occupy are unknown for the mixed overlayers, the meaning of the ratios for the hydrogen covered surfaces cannot be determined quantitatively. However, the large values for the ratio when the p(2x2) is transformed to the $\sqrt{3}$ structure are significant. This indicates that the net CO coverage increases in the transformation far more than is needed to account for the structural change, even if the excluded area per disordered CO has decreased, i.e., more CO molecules are added than are needed to complete the transformation. The additional molecules either increase the size of the ordered CO region, or are added to the hydrogen region; in all likelihood, both processes occur.

The ratio of coverages for the $\sqrt{3}$ to (2x2) structural change is nearly invariant for all hydrogen coverages. This suggests that the excluded area for the disordered CO molecules has decreased during the transformation. Otherwise, the ratios for the hydrogen covered surfaces would have been lower. In addition (and possibly causing the smaller excluded area), additional CO may have been added as in the p(2x2) to $\sqrt{3}$ transformation.

The mechanism for formation and growth of CO islands on a hydrogen covered surface deduced from these measurements is illustrated schematically in Fig. 10. The nucleation of an island is shown in Fig. 10(a). There, the initial chemisorption of a mobile precursor CO molecule causes migration of the relatively mobile (22) hydrogen atoms away from its vicinity due to the repulsive hydrogen-CO interaction. Other mobile precursor CO molecules adsorb preferentially near a chemisorbed CO, minimizing the CO-hydrogen interaction and initiating island formation. As more CO adsorbs, statistically some nucleation sites will fail to develop. Pockets of CO, either lone molecules or small clusters, will then be trapped in regions of high hydrogen density. Similarly, some hydrogen atoms may be trapped in the growing CO islands. These trapped species are not shown in Fig. 10. The p(2x2) island is shown at maximum size in Fig. 10(b). At this point, when a mobile precursor CO encounters the island, addition of the molecule at the edge of the island, which would cause either a decreased CO-H distance or a decreased H-H distance, becomes energetically less favorable than addition of a CO to the interior of the island causing a decreased CO-CO distance. Transformation of the island to the $\sqrt{3}$ structure begins and is possibly accompanied by additional adsorption of CO into the

hydrogen region. The completion of the transformation is shown in Fig. 10(c). At this point, the energy balance changes in favor of island growth. The $\sqrt{3}$ island increases in size until, in Fig. 10(d), the increase in CO-H repulsive energy and the compression of the hydrogen layer become too unfavorable to allow further growth. Addition of CO into the island is still energetically feasible, and CO adsorption into the hydrogen region with displacement of hydrogen may take place also. Adsorption of CO continues until the island is completely transformed to the high coverage (2x2) structure, shown in Fig. 10(e).

B. Relationship to Catalytic Behavior

The segregation of CO and hydrogen observed at 100 K, of course would not persist at high temperatures where effects of entropy dominate. Thus, there would not be an appreciable effect on the catalytic behavior of rhodium due to segregation. However, the repulsive interaction between hydrogen and CO is a microscopic, not a macroscopic, property and will occur regardless of the temperature or degree of segregation. This repulsion could decrease the probability of direct reaction of hydrogen and CO on Rh as compared to other metals for which the interaction is not repulsive.

Few studies resulting in direct information on the nature of the CO-hydrogen interaction have been reported. There is apparently a weak attractive interaction between hydrogen and CO on Pd(110) (25). On Ir(110), there appears to be little or no direct interaction (26). Correlation of such studies with those concerning the formation of complexes of CO and

hydrogen (10 - 12, 27) may be useful in determining the details of the reaction mechanisms for the hydrogenation of CO over transition metals.

5. Synopsis

(1) Adsorption of CO on Rh(111) proceeds via a physically adsorbed intermediate, a mobile precursor to adsorption.

(2) There is a strong repulsive interaction between co-adsorbed CO molecules and hydrogen atoms on rhodium. This results in partial segregation of hydrogen and CO following adsorption of CO onto an adlayer of hydrogen at 100 K. The interaction is apparent at distances up to 2.7 -3.1 Å, indicating that it is a through-metal effect. At smaller distances, of course, orbital overlap may be important.

Appendix

Derivation of Adsorption Kinetics Using the First-Order Mobile Precursor Model (20)

Each molecule impinging upon the surface has a probability of entering a physically adsorbed state above either a filled or an empty site. Its subsequent behavior is governed by a set of probabilities:

$P_a \equiv$ The probability that a molecule, physically adsorbed above an empty site, chemisorbs in that site.

$P_b \equiv$ The probability that a molecule above an empty site desorbs.

$P_b' \equiv$ The probability that a molecule above a filled site desorbs.

$P_c \equiv$ The probability that the physically adsorbed molecule diffuses to a position above another site.

On the clean surface, the frequency of encounter of empty sites is $1 - \hat{\theta}$; the frequency of encounter of filled sites is $\hat{\theta}$. Thus, a newly physically adsorbed molecule has a probability $P_{a1} = P_a(1 - \hat{\theta})$ of chemisorbing, $P_{b1} = P_b(1 - \hat{\theta}) + P_b'\hat{\theta}$ of desorbing, and $P_{c1} = 1 - P_{a1} - P_{b1}$ of diffusing to another site. If it diffuses, it then has probability, $P_{a2} = P_{c1}P_{a1}$ of chemisorbing, etc. Summation of the probabilities of chemisorption, P_{a1}, P_{a2},...., then leads to

$$\frac{d\hat{\theta}}{d\varepsilon} \alpha \frac{P_a}{P_a + P_b} \frac{1 - \hat{\theta}}{1 - c\hat{\theta}}$$

where $$c \equiv \left(1 - \frac{P_b'}{P_a + P_b}\right)$$

and ε is the exposure.

On a hydrogen covered surface, the frequency of encounter of empty sites is $\hat{\theta}_s - \hat{\theta}$, where $\hat{\theta}_s = 1 - a\hat{\theta}_H$ and a is a constant of proportionality. The frequency of encounter of filled sites is $1 - \hat{\theta}_s + \hat{\theta}$. Therefore, on a hydrogen covered surface, the newly physically adsorbed molecule has probability $P_{a1} = P_a(\hat{\theta}_s - \hat{\theta})$ of chemisorbing, $P_{b1} = P_b(\hat{\theta}_s - \hat{\theta}) + P_b'(1 - \hat{\theta}_s + \hat{\theta})$ of desorbing, and $P_{c1} = 1 - P_{a1} - P_{b1}$ of diffusing to another site. In this case, summation of the probabilities of chemisorption leads to

$$\frac{d\hat{\theta}}{d\varepsilon} \alpha \frac{P_a}{P_a + P_b - P_b'} \frac{\hat{\theta}_s - \hat{\theta}}{c_2 + \hat{\theta}_s - \hat{\theta}}$$

where

$$c_2 \equiv \frac{P_b'}{P_a + P_b - P_b'}$$

This reduces to the clean surface equation in the limit of zero coverage of hydrogen.

References

1. M. A. Vannice, Catal. Rev. 14, 153 (1976).
2. G. C. Bond, Catalysis by Metals, Academic Press, New York, 1962.
3. J. A. Rabo, A. P. Risch and M. L. Pontsma, J. Catal. 53, 295 (1978).
4. M. Araki and V. Ponec, J. Catal. 44, 439 (1976).
5. R. D. Kelley, T. E. Madey and J. T. Yates, Jr., J. Catal. 50, 301 (1977).
6. T. E. Madey, D. W. Goodman and R. D. Kelley, J. Vacuum Sci. Technol. 16, 433 (1979).
7. R. D. Kelley, T. E. Madey, K. Revesz, J. T. Yates, Jr., Appl. Surface Sci. 1, 266 (1978).
8. B. A. Sexton and G. A. Somorjai, J. Catal. 46, 167 (1977).
9. D. J. Dwyer and G. A. Somorjai, J. Catal. 52, 291 (1978).
10. K. Kraemer and D. Menzel, Ber. Buns. Ges. 79, 649 (1975).
11. V. H. Baldwin and J. B. Hudson, J. Vacuum Sci. Technol. 8, 49 (1971).
12. J. C. Bertolini and B. Imelik, Surface Sci. 80, 586 (1979).
13. J. T. Yates, Jr., P. A. Thiel and W. H. Weinberg, Surface Sci. 84, 427 (1979).
14. P. A. Thiel, E. D. Williams, J. T. Yates, Jr. and W. H. Weinberg, Surface Sci. 84, 54 (1979).
15. D. G. Castner, B. A. Sexton and G. A. Somorjai, Surface Sci. 71, 519 (1978).
16. M. A. Vannice, J. Catal. 37, 449 (1975).
17. D. R. Sandstrom and S. P. Withrow, J. Vacuum Sci. Technol. 14, 748 (1977).

18. C.-M. Chan, P. A. Thiel, J. T. Yates, Jr. and W. H. Weinberg, Surface Sci. 76, 296 (1978).

19. C.-M. Chan, R. Aris and W. H. Weinberg, Appl. Surface Sci. 1, 360 (1978).

20. P. Kisliuk, J. Phys. Chem. Solids 3, 95 (1957).

21. R. Gorte and L. D. Schmidt, Surface Sci. 76, 559 (1978).

22. K. Christmann, R. J. Behm, G. Ertl, M. A. Van Hove and W. H. Weinberg, J. Chem. Phys. 70, 4168 (1979).

23. T. B. Grimley and M. Torrini, J. Phys. C 6, 868 (1973).

24. T. Einstein and J. R. Schrieffer, Phys. Rev. B 7, 3629 (1973).

25. H. Conrad, G. Ertl and E. E. Latta, J. Catal. 35, 363 (1974).

26. D. E. Ibbotson, T. S. Wittrig and W. H. Weinberg, in preparation.

27. J. T. Yates, Jr., S. D. Worley, T. M. Duncan and R. W. Vaughan, J. Chem. Phys. 70, 1225 (1979).

Table Captions

Table 1: Parameters for adsorption of CO onto hydrogen covered surface. $\hat{\theta}_H$ is the initial coverage of hydrogen. $\hat{\theta}_s$ is the saturation coverage of CO. $d\hat{\theta}/d\varepsilon$ is the slope of the linear region of the $\hat{\theta}_{CO}$ - ε curve.

Table 2: Absolute coverages of CO at the points of maximum intensity for the three CO structures at different initial coverages of hydrogen.

(a) Ratio of the coverage in the $\sqrt{3}$ structure to that in the p(2x2).

(b) Ratio of the coverage in the (2x2) structure to that in the $\sqrt{3}$.

Table 1

$\hat{\theta}_H$	$\hat{\theta}_s$	$\frac{d\hat{\theta}}{d\varepsilon}$, L^{-1}
0.0	1.0	0.30
0.42	0.71	0.25
0.58	0.57	0.23
0.75	0.40	0.20
0.92	0.28	0.16
0.99	0.22	—

Table 2

$\hat{\theta}_H$	$\theta_{CO}^{p(2x2)}$	$\theta_{CO}^{\sqrt{3}}$	$\theta_{CO}^{(2x2)}$	(a) $R\left[\frac{\sqrt{3}}{p(2x2)}\right]$	(b) $R\left[\frac{(2x2)}{\sqrt{3}}\right]$
0.0	$.23^{1}$	$.34^{6}$	$.75^{0}$	1.52	2.13
0.26	$.14^{7}$	-	$.60^{0}$	-	-
0.42	$.11^{4}$	$.24^{7}$	$.53^{6}$	2.17	2.17
0.58	$.09^{2}$	$.20^{4}$	$.43^{0}$	2.22	2.11
0.75	$.06^{9}$	$.14^{3}$	$.30^{2}$	2.07	2.11
0.92	$.04^{0}$	$.07^{5}$	$.20^{7}$	1.88	2.76

Figure Captions

Fig. 1: Coverage-exposure behavior for adsorption of hydrogen at approximately 100 K. Circles correspond to adsorption onto the clean surface. (Open and closed circles represent data taken on two different crystals.) Triangles correspond to adsorption onto a surface with 0.21 monolayer of CO present.

Fig. 2: Desorption parameters for hydrogen. E_d is the activation energy for desorption. $\nu_0^{(2)}$ is the pre-exponential factor of the desorption rate coefficient. n_s is the number density of hydrogen at saturation. Circles represent desorption from the clean surface. Triangles represent desorption from the surface with 0.21 monolayer of CO present. Straight lines are drawn according to a linear least squares fit to the data.

Fig. 3: Coverage-exposure behavior for adsorption of CO onto the surface with varying amounts of hydrogen present. Adsorption temperature is approximately 100 K. Data points at $\hat{\theta}_{CO} < 0.5$ for adsorption on the clean surface have been omitted for clarity (see Fig. 4). Open and closed circles represent data from two different crystals.

Fig. 4: Comparison of coverage-exposure data with curves predicted by first-order Langmuir and mobile precursor adsorption kinetics. Open and closed circles are data points for adsorption onto a clean surface as in Fig. 3. Stars are data points for adsorption onto a surface precovered with 0.58 of the saturation coverage of hydrogen.

Fig 5: Comparison of the apparent initial slope (see text) of the coverage-exposure curve for two models of adsorption with the experimental values.

Fig. 6: LEED intensity as a function of exposure for the $\sqrt{3}$ structure. Dashed line shows the result of exposing the clean surface to CO. Solid lines show the results of terminating CO exposure at various coverages and initiating exposure to hydrogen. T_{Rh} is approximately 100 K. Intensities are normalized to unity at the maximum intensity of the $\sqrt{3}$ structure on the clean surface.

Fig. 7: LEED intensity as a function of exposure to CO for the two (2x2) structures on a surface covered with varying amounts of hydrogen.

(a) $\hat{\theta}_H = 0$ (d) $\hat{\theta}_H = 0.58$

(b) $\hat{\theta}_H = 0.26$ (e) $\hat{\theta}_H = 0.75$

(c) $\hat{\theta}_H = 0.42$

Intensities are normalized to unity at the maximum intensity of the $\sqrt{3}$ structure on the clean surface.

Fig. 8: LEED intensity as a function of exposure to CO for the $\sqrt{3}$ structure on a surface covered with varying amounts of hydrogen.

(a) $\hat{\theta}_H = 0$ (d) $\hat{\theta}_H = 0.75$

(b) $\hat{\theta}_H = 0.42$ (e) $\hat{\theta}_H = 0.92$

(c) $\hat{\theta}_H = 0.58$

Fig. 9: Intensity as a function of coverage of CO for the p(2x2) structure on the clean (solid line) and hydrogen covered (points) surface. The points represent the intensity at the maxima of the p(2x2) curves in Fig. 7, normalized to the maximum intensity on the clean surface. Each point is the result of an average of two to five measurements.

Fig. 10: Schematic illustration of adsorption of CO onto a surface covered with hydrogen. Open circles are rhodium atoms with d = 2.7 Å. Shaded circles are CO molecules with d = 3.1 Å. Shaded circles with arrow are physically adsorbed, mobile precursor CO molecules. Solid circles are H atoms with d = 1.5 Å (estimated). Adsorption sites shown have been chosen arbitrarily. Hydrogen and CO trapped in the "wrong" regions are not shown for clarity. See text for discussion.

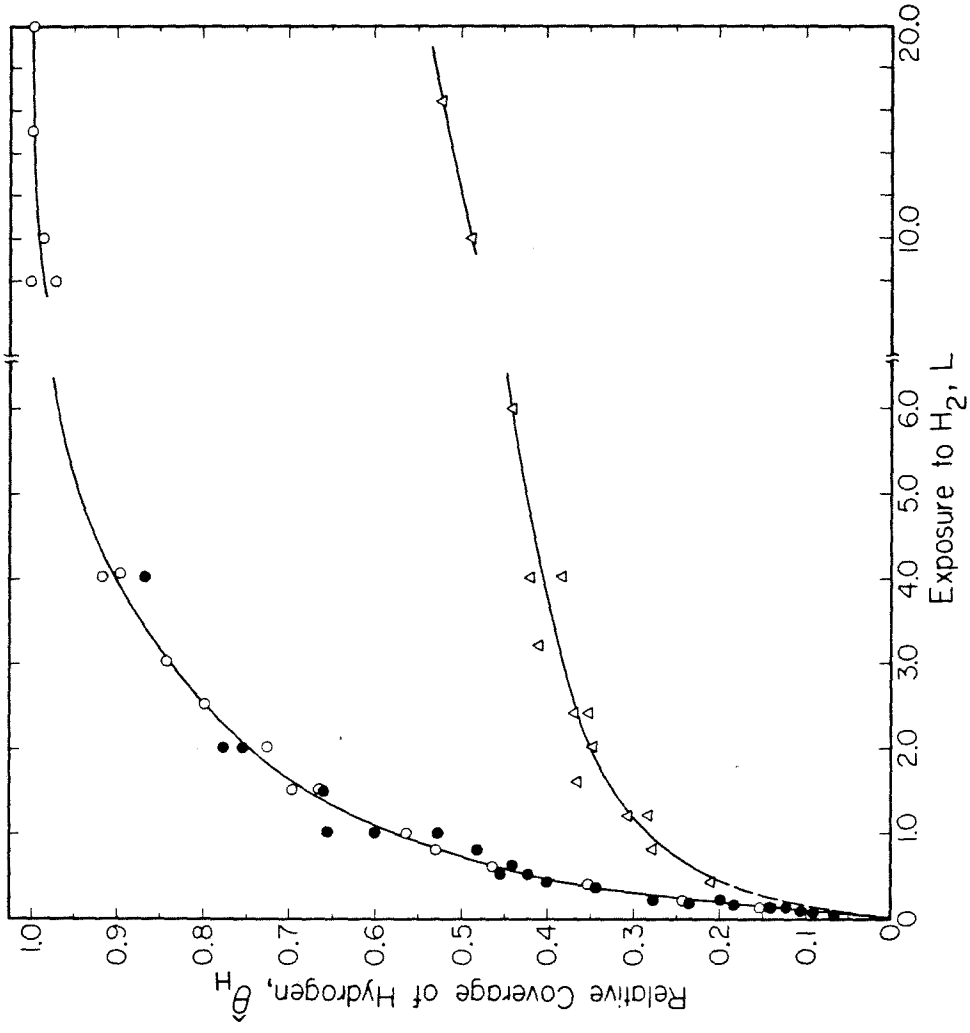
Relative Coverage of Hydrogen, θ_H
Exposure to H_2, L
0
0.1
0.2
0.3
0.4
0.5
0.6
0.7
0.8
0.9
1.0
1.0
2.0
3.0
4.0
5.0
6.0
10.0
20.0

Fig. 1

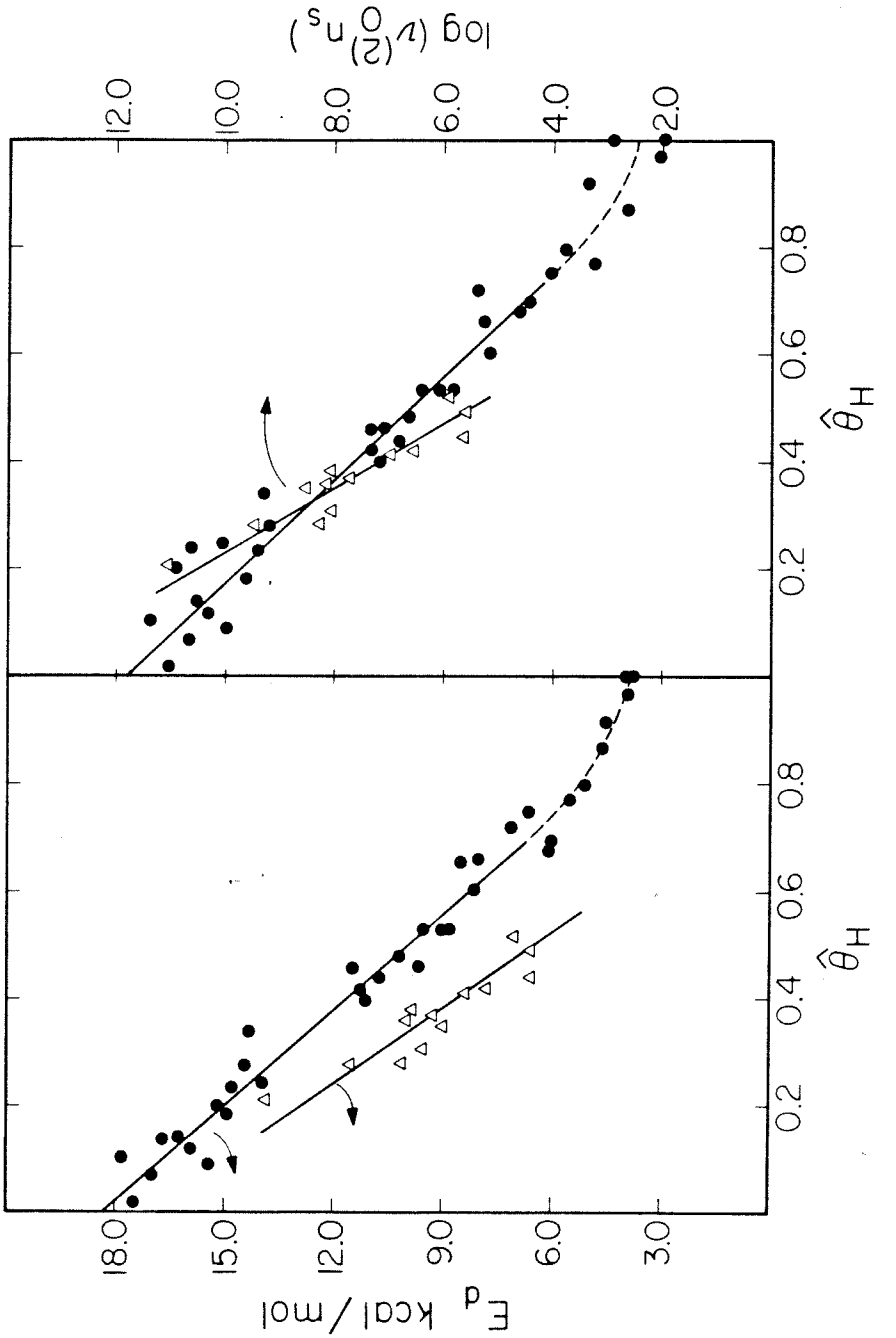
E_d kcal/mol
18.0
15.0
12.0
9.0
6.0
3.0
0.2
0.4
0.6
0.8
$\hat{\theta}_H$
log ($\nu_O^{(2)} n_s$)
12.0
10.0
8.0
6.0
4.0
2.0
0.2
0.4
0.6
0.8
$\hat{\theta}_H$

Fig. 2

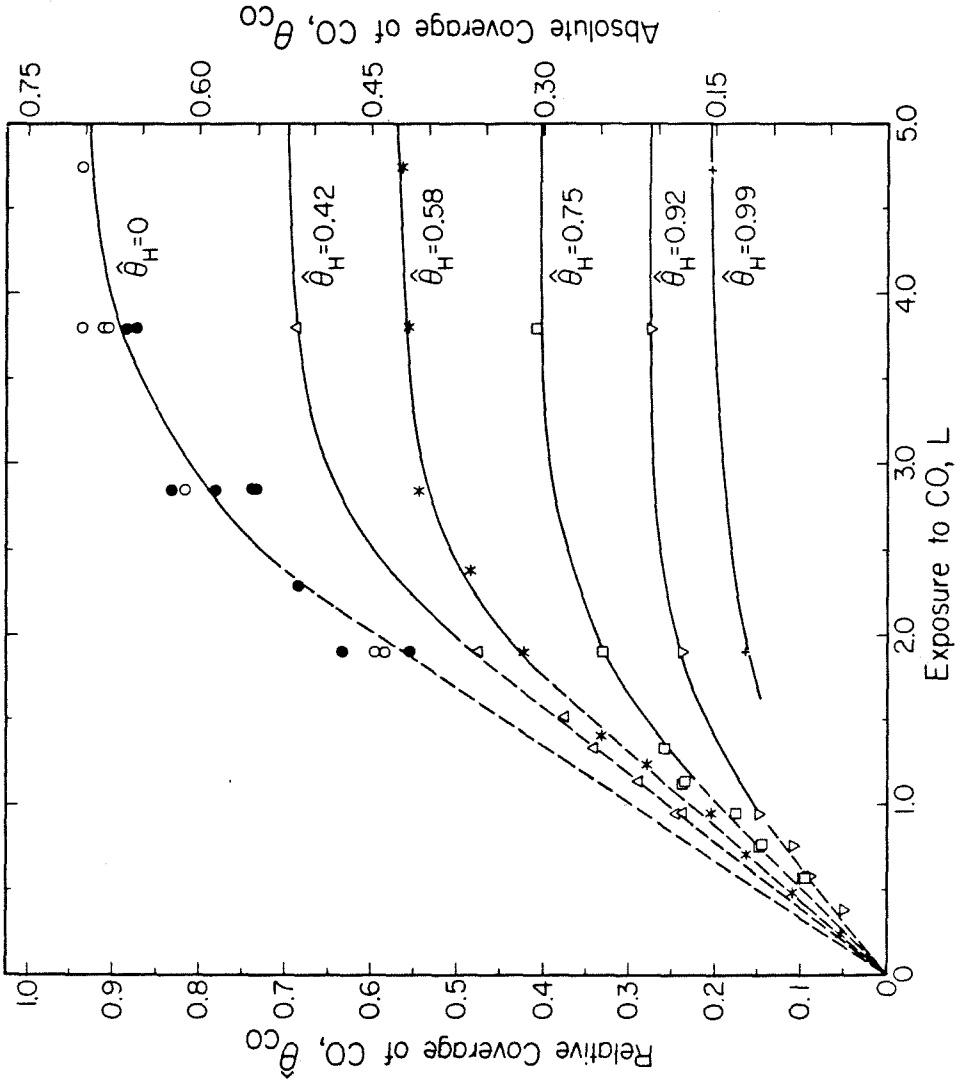
Absolute Coverage of CO, θ_{CO}
0.75
0.60
0.45
0.30
0.15
$\hat{\theta}_H$=0
$\hat{\theta}_H$=0.42
$\hat{\theta}_H$=0.58
$\hat{\theta}_H$=0.75
$\hat{\theta}_H$=0.92
$\hat{\theta}_H$=0.99
Relative Coverage of CO, $\hat{\theta}_{CO}$
1.0
0.9
0.8
0.7
0.6
0.5
0.4
0.3
0.2
0.1
0
1.0
2.0
3.0
4.0
5.0
Exposure to CO, L

Fig. 3

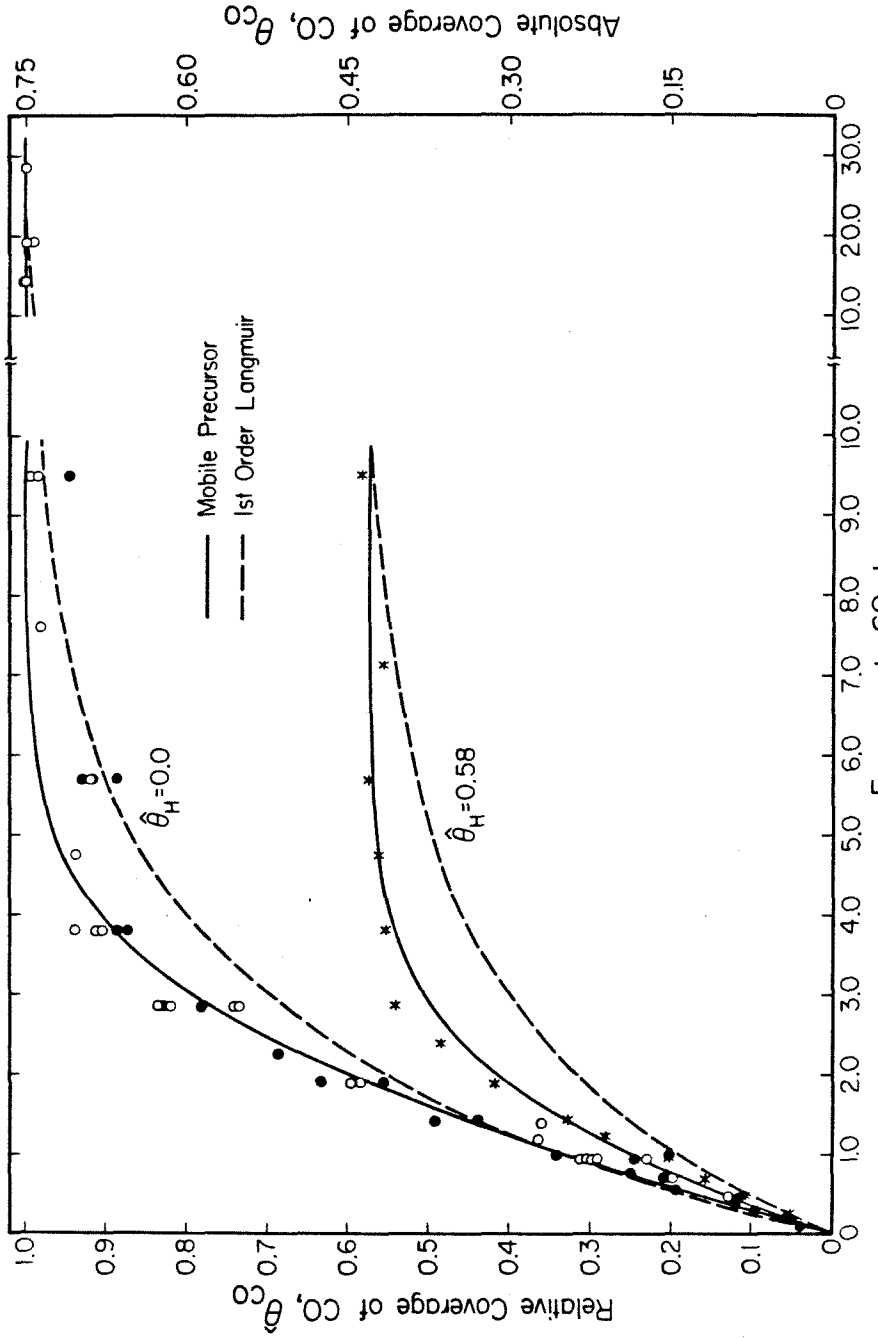
Relative Coverage of CO, θ_{CO}
Absolute Coverage of CO, θ_{CO}
Exposure to CO, L
Mobile Precursor
1st Order Langmuir
$\hat{\theta}_H$=0.0
$\hat{\theta}_H$=0.58

Fig. 4

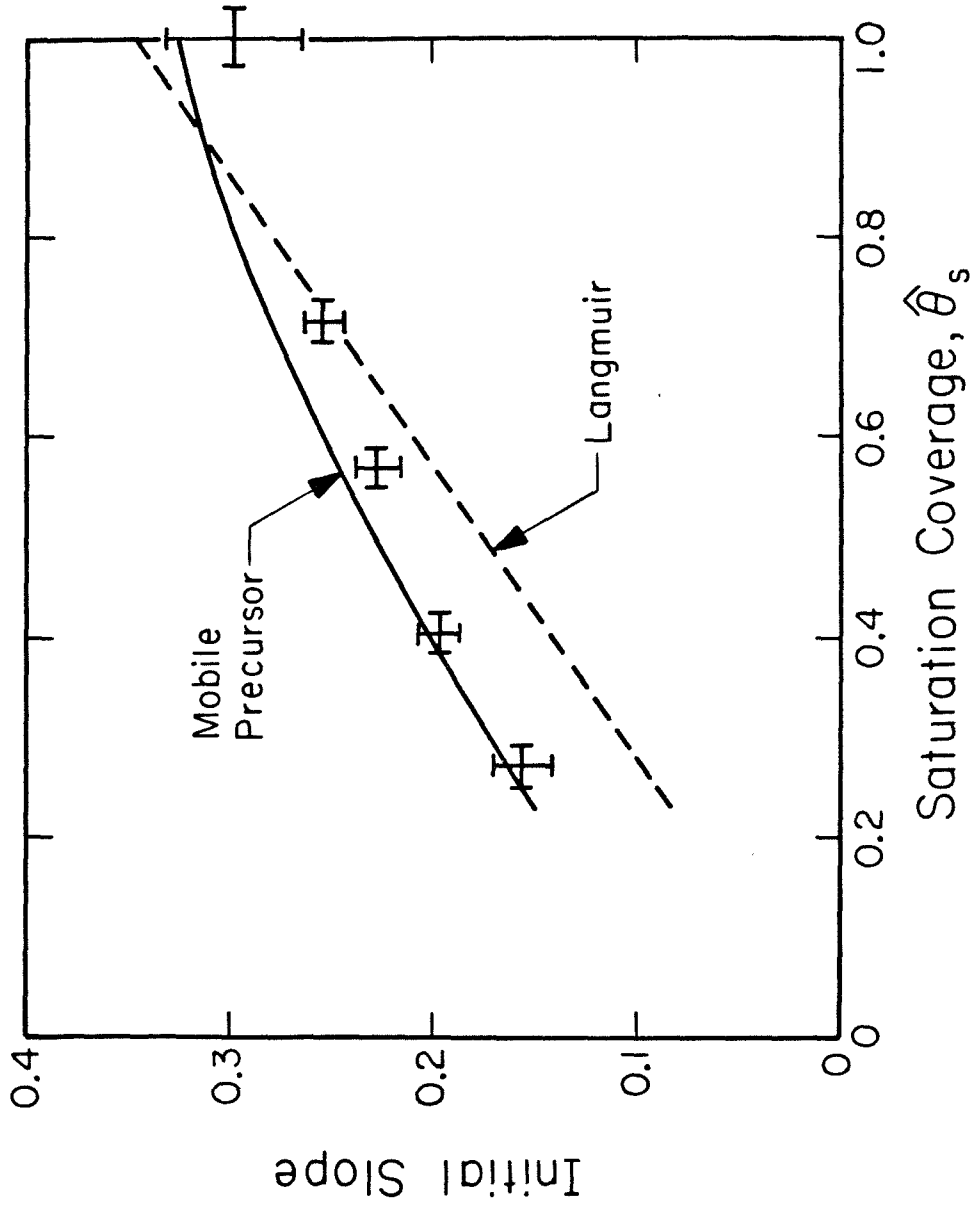
Initial Slope
0.4
0.3
0.2
0.1
0
0
0.2
0.4
0.6
0.8
1.0
Saturation Coverage, $\hat{\theta}_s$
Mobile Precursor
Langmuir

Fig. 5

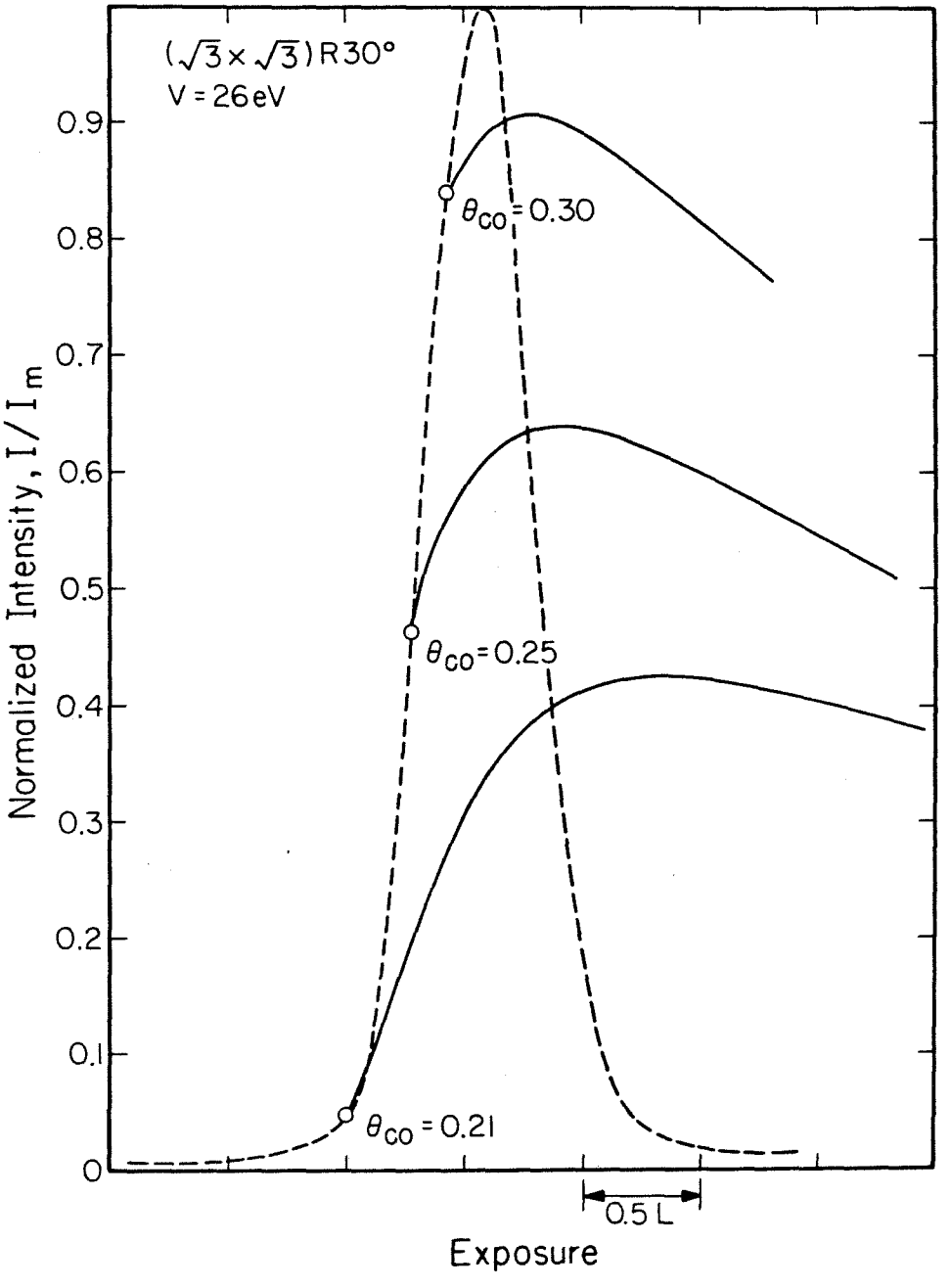
(√3×√3)R30°
V = 26eV
θCO = 0.30
θCO = 0.25
θCO = 0.21
0.5 L
Normalized Intensity, I / Im
Exposure
0
0.1
0.2
0.3
0.4
0.5
0.6
0.7
0.8
0.9

Fig. 6

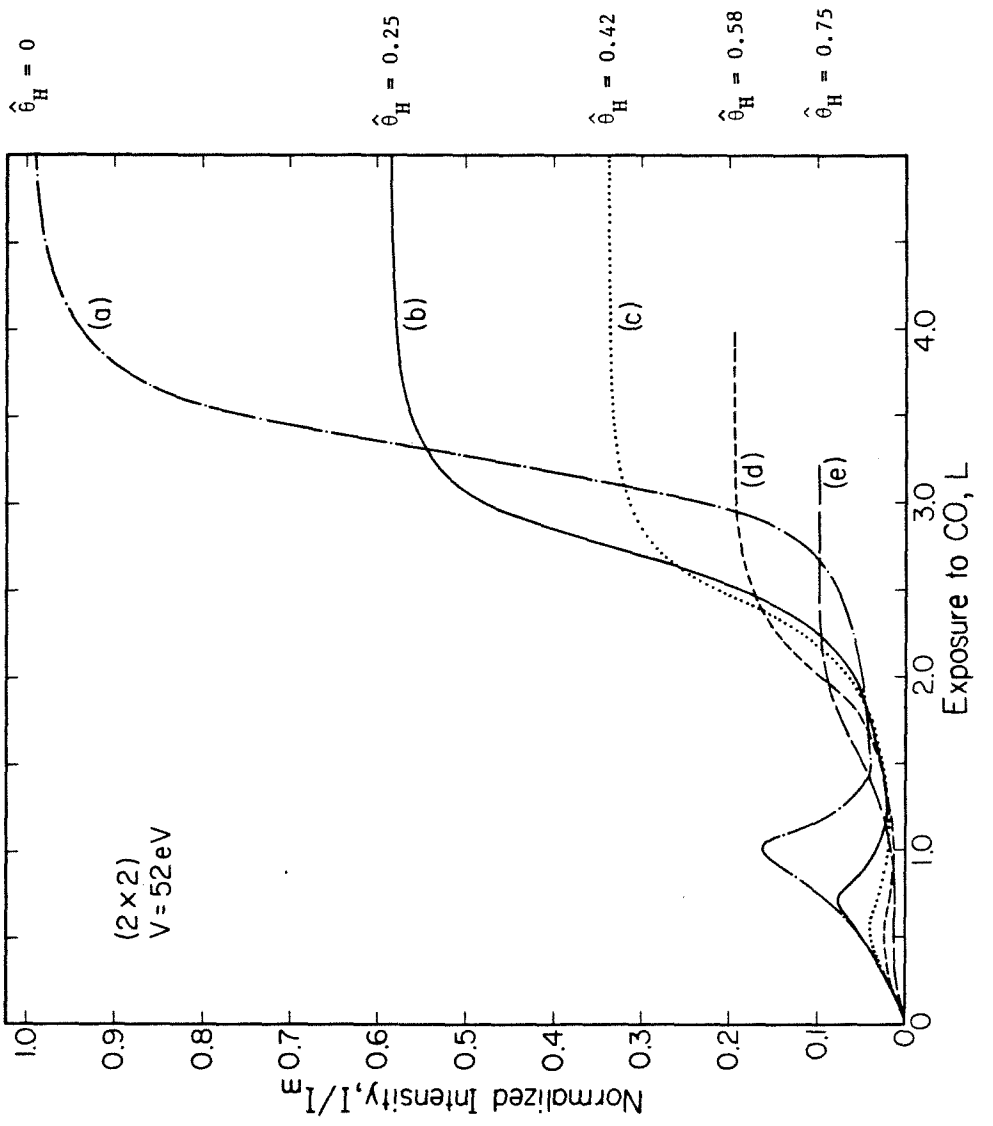
$\hat{\theta}_H$ = 0
$\hat{\theta}_H$ = 0.25
$\hat{\theta}_H$ = 0.42
$\hat{\theta}_H$ = 0.58
$\hat{\theta}_H$ = 0.75
(a)
(b)
(c)
(d)
(e)
(2×2)
V = 52 eV
Normalized Intensity, I/I_∞
Exposure to CO, L
0
1.0
2.0
3.0
4.0
0.1
0.2
0.3
0.4
0.5
0.6
0.7
0.8
0.9
1.0

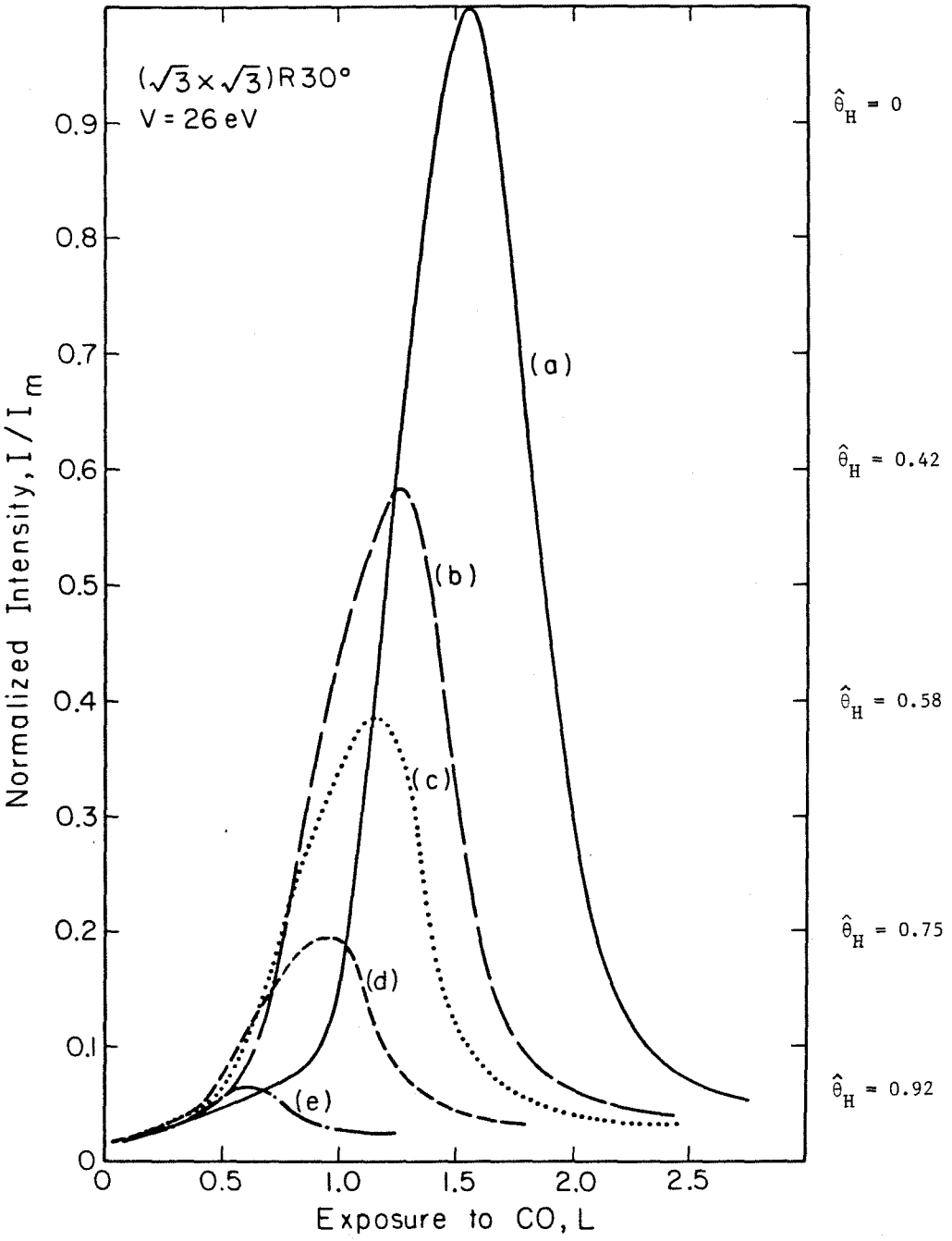
(√3×√3)R30°
V = 26 eV
Normalized Intensity, I / I m
Exposure to CO, L
0
0.1
0.2
0.3
0.4
0.5
0.6
0.7
0.8
0.9
0.5
1.0
1.5
2.0
2.5
(a)
(b)
(c)
(d)
(e)
θ̂H = 0
θ̂H = 0.42
θ̂H = 0.58
θ̂H = 0.75
θ̂H = 0.92

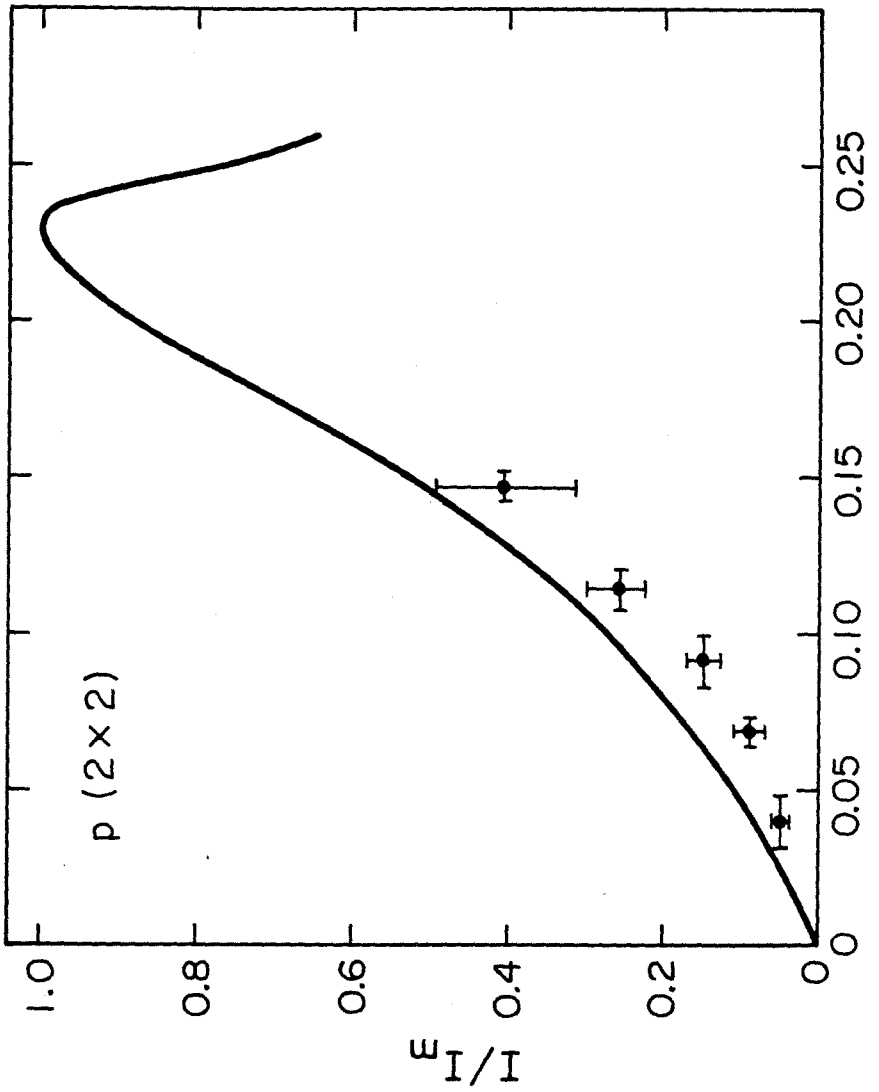

Fig. 9

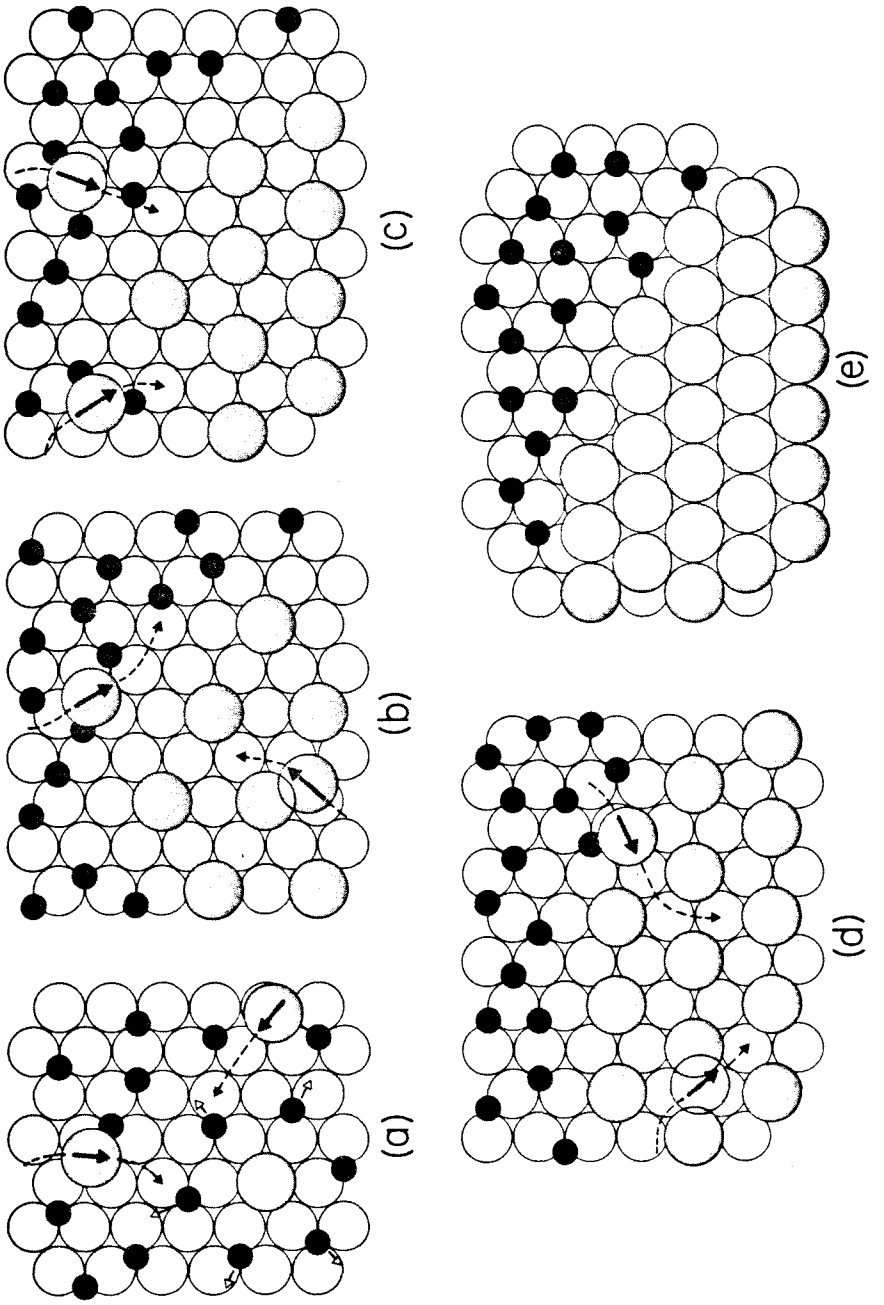

Fig. 10

Section IV

The Adsorption of Sulfur on the Reconstructed Ir(111)-(1x2) Surface

Surface Science 81 (1979) L309–L314

SURFACE SCIENCE LETTERS

THE ADSORPTION OF SULFUR ON THE RECONSTRUCTED Ir(110)-(1 × 2) SURFACE [a]

Ellen D. WILLIAMS [b], C.-M. CHAN [c] and W.H. WEINBERG [d]
Division of Chemistry and Chemical Engineering, California Institute of Technology, Pasadena, California 91125, USA

Received 25 September 1978; manuscript received in final form 12 October 1978

An important and intriguing problem in surface science is the reconstruction of the surface layers of atoms with respect to the bulk structure. This phenomenon has been observed for the (110) surface of Ir, Pt and Au [1–3], which all reconstruct into a (1 × 2) structure. Recently, experimental and theoretical work has been carried out to determine the structures of the clean (1 × 2)- and oxygen stabilized (1 × 1)-(110) surfaces of Ir [4–7]. As a complement to and an extension of this work, a study of the interaction of sulfur with the *reconstructed* Ir(110) surface has been undertaken. The structural analysis of the clean reconstructed Ir(110)-(1 × 2) surface showed that the missing row model with a topmost interlayer spacing of 1.22 ± 0.07 Å is the preferred structure [4,5,7]. It is this surface on which the overlayers of sulfur were adsorbed.

The experiments were carried out in a UHV system which has been described previously [6]. Sulfur was introduced onto the surface by exposure to H_2S gas (cp. grade, 99.5% purity). The presence of sulfur on the surface was monitored by Auger Electron Spectroscopy (AES). Even at saturation coverages of sulfur (exposure ~35 L H_2S, where 1 L $\equiv 10^{-6}$ Torr sec), the intensities of the Ir transitions in the Auger spectrum were nearly unattenuated. It was found that the sulfur could be removed from the surface by heating the crystal briefly in vacuum at 1600 K. As this treatment caused some carbon to migrate to the surface, the crystal was then cleaned by heating in 5×10^{-8} Torr of oxygen at 950 K, followed by flashing to 1630 K in vacuum.

A series of Low-Energy Electron Diffraction (LEED) patterns was observed upon exposure of the crystal to H_2S at 350 K. A (2 × 2) pattern with the ($\frac{1}{2}(2n + 1)$

[a] Supported by the National Science Foundation under Grant No. DMR77-14976.
[b] National Science Foundation Predoctoral Fellow.
[c] American Vacuum Society Predoctoral Scholar.
[d] Alfred P. Sloan Foundation Fellow, and Camille and Henry Dreyfus Foundation Teacher-Scholar.

O) beams absent was observed at low exposures and reached its maximum intensity after an exposure of 4 L H_2S. This pattern is illustrated in fig. 1. The intensity of this LEED pattern was not changed after heating to temperatures as high as 1200 K and then cooling back to 350 K. This indicates that either no hydrogen is left on the surface at 350 K, or that it is in a disordered state that does not affect the LEED pattern. As the exposure to H_2S was increased above 4 L, the "extra" (2 X 2) beams disappeared leaving the original beams of the (1 X 2) structure. Meanwhile, a streaky, diffuse pattern developed between the rows of the (1 X 2) pattern. Heating the crystal to 950 K after an exposure to 8 L H_2S caused the diffuse pattern to transform into a weak c(2 X 4) one. At higher exposures to H_2S (up to 35 L), a more intense c(2 X 4) structure with streaks parallel to the y-axis and located at $x = \frac{1}{4}(2n + 1)$ was observed after heating to 950 K. Comparison of the amplitude of the S transitions in the Auger spectra shows that the coverage at saturation is approximately twice that at the maximum intensity of the (2 X 2) pattern. Work is in progress to determine quantitatively the relative coverages corresponding to these LEED patterns, as well as the adsorption and desorption kinetics using thermal desorption mass spectrometry.

The observation that the (1 X 2) substrate beams remain bright and sharp throughout the growth *and disappearance* of the (2 X 2) pattern suggests that the adsorption of sulfur does not cause the Ir(110) surface to relax from the recon-

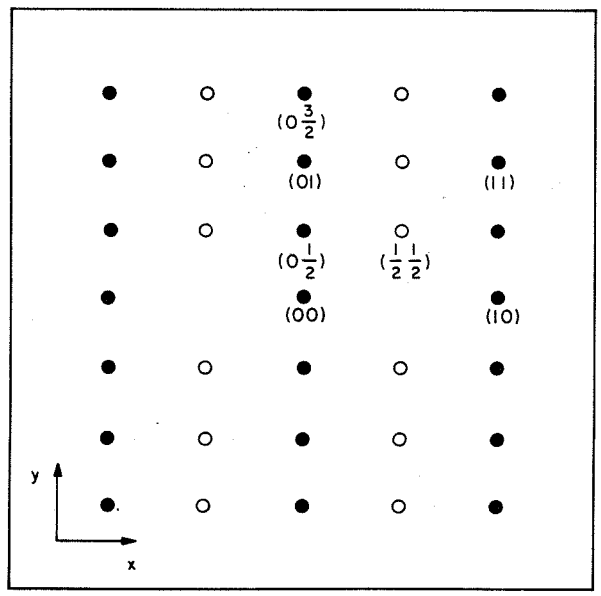

Fig. 1. p1g1-(2 X 2) LEED pattern observed after exposure of Ir(110)-(1 X 2) to 4 L H_2S at 350 K. Solid circles indicate substrate (1 X 2) beams, open circles the "extra" beams due to the (2 X 2) structure.

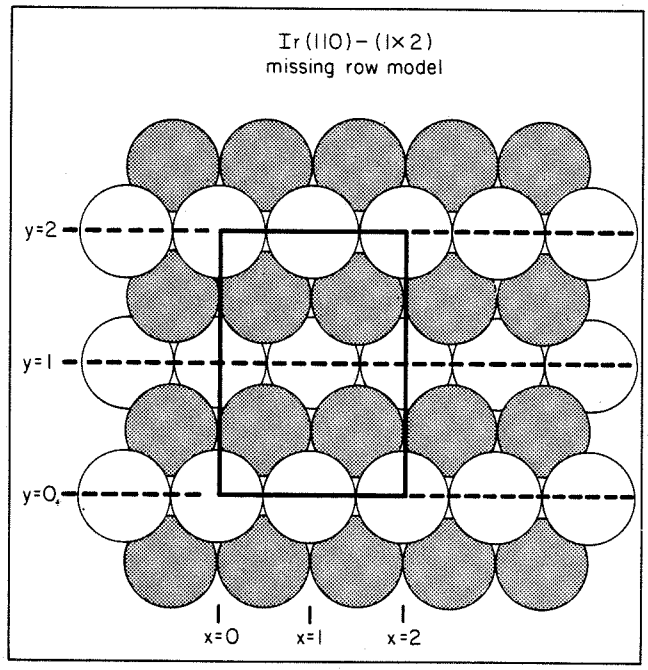

Fig. 2. Location of glide planes (– – –) for a p1g1 or p2mg-(2 × 2) unit cell on the Ir(110)-(1 × 2) surface (missing row model). Open circles indicate first and third layer Ir atoms; shaded circles, second layer Ir atoms.

structed (1 × 2) form. This, together with the occurrence of the missing beams in the (2 × 2) pattern, allows the structure corresponding to the (2 × 2) pattern to be delimited.

The absence of certain beams at all incident electron energies indicates destructive interference due to equivalent scatterers within the (2 × 2) unit cell. Specifically, the extinction of the $(\frac{1}{2}(2n + 1)\,0)$ beams indicates a surface structure of either P1g1 or p2mg symmetry [8]. Both of these symmetries include glide planes * parallel to the x-axis and located at $y = 0$, 1 and 2 within the unit cell. Due to the low symmetry of the (1 × 2) surface, as illustrated in fig. 2 for the missing row model for Ir(110)-(1 × 2) [4], there is only one possible set of locations for these glide planes. This restriction is equally valid for any other model of the reconstructed (1 × 2) surface.

For the p1g1 symmetry, there are two atoms within the unit cell, located at (x, y) and $(1 + x, \bar{y})$, with x and y such that the glide planes are the only symmetry elements of the structure. A posssible p1g1-(2 × 2) structure is shown in fig. 3. In

* A glide plane indicates invariance under the operation: translation parallel to the plane by one-half the length of the [(2 × 2)] unit cell, followed by reflection across the plane.

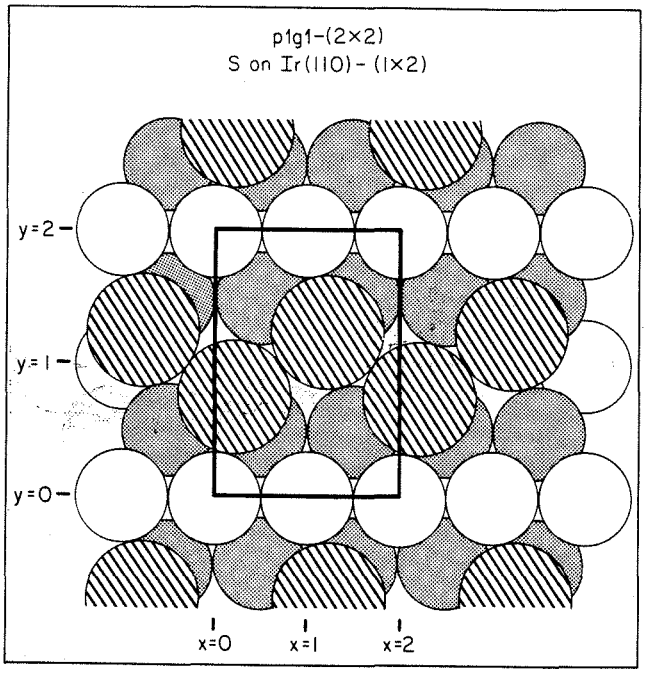

Fig. 3. A possible p1g1-(2 × 2) structure for sulfur on Ir(110)-(1 × 2). Sulfur atoms (cross-hatched) are shown with a hard sphere radius of 1.7 Å [9]. The radius of an Ir atom is 1.36 Å. Sulfur atoms are located at (x, y) and $(1 + x, \bar{y})$. Translating the S atoms to $(\bar{x}, y)$, $(1 + \bar{x}, \bar{y})$ results in an equivalent (mirror image) domain of the structure shown.

this illustration, the S atoms are prevented from occupying the sites on the "missing row" by S–S interactions.

Either two or four atoms per unit cell are allowed for the p2mg structure. The four-atom structure (which would correspond to a fractional coverage of unity) is considered unlikely on the basis of the evidence that much higher coverages of S are possible than that required for the (2 × 2) structure without attenuation of the Ir Auger signals. In the case of two atoms per unit cell, the S atoms would be located so that a mirror plane parallel to the y-axis runs through each S atom. Two possible p2mg structures are shown in fig. 4. The structures depicted would arise if S atoms with a covalent radius of 1.0 Å [9] were adsorbed in the threefold sites of the terraces of (111) planes exposed by the missing row. Other p2mg structures, generated by changing the y-coordinates shown in fig. 4a and b, are also plausible. For instance, a structure similar to that shown in fig. 3 but with a p2mg symmetry would be a reasonable hypothesis.

In an attempt to distinguish between the possibility of a p1g1 and a p3mg symmetry, the intensity versus voltage (I–V) profiles for two sets of corresponding beams in three quadrants were measured. As shown in fig. 5, the I–V spectra for

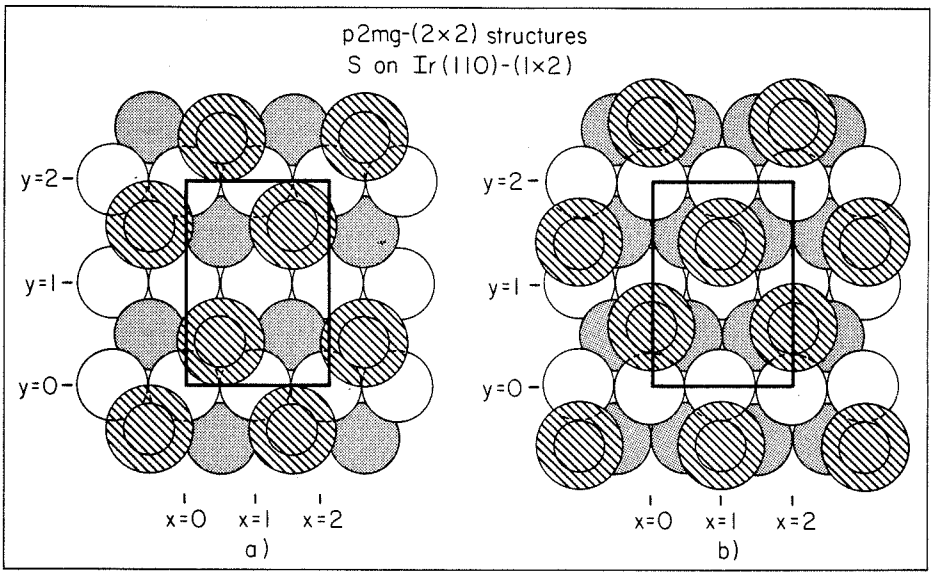

Fig. 4. Two possible p2mg-(2 × 2) structures for sulfur on Ir(110)-(1 × 2). The inner circle on the S atoms shows the covalent radius of 1.0 Å [9]. (a) S located in three-fold site formed by two top layer and one second layer Ir atoms. (b) S located in three-fold site formed by one top layer and two second layer Ir atoms.

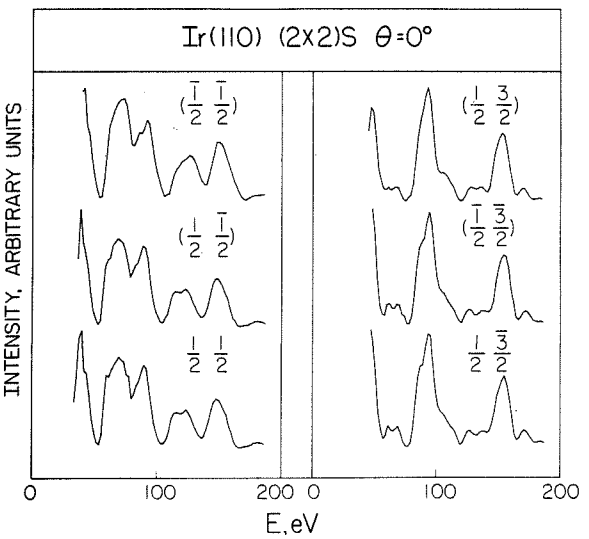

Fig. 5. LEED $I-V$ spectra showing the equivalence of corresponding beams in three quadrants. (a) The $(\frac{1}{2}, \frac{1}{2})$ beams. (b) The $(\frac{1}{2}, \frac{3}{2})$ beams.

the three beams of each set are identical. If the $(n/2, \pm m/2)$ beams had had different $I-V$ spectra than the $(-n/2, \pm m/2)$ beams, it would have shown that one domain of a p1g1 structure (see caption, fig. 3) predominated on the surface [10]. Since the I–V spectra are the same, it is not possible to determine which of the two symmetries is present, as the observed equivalence could be due either to equal representation of the two domains of a p1g1 structure or to a p2mg structure.

Therefore, symmetry considerations allow the structure of the (2 × 2) sulfur overlayer on the reconstructed Ir(110) surface to be limited to one of three possible types. The three types are the following: (1) a p1g1 structure with sulfur atoms at (x, y), $(1+x, \bar{y})$, $x \neq 0, \frac{1}{2}$ or 1, $y \neq 0, \frac{1}{2}$ or 1; (2) a p2mg structure with sulfur atoms at $(\frac{1}{2}, y)$, $(\frac{3}{2}, \bar{y})$, $y \neq 0, \frac{1}{2}$ or 1; and (2) a p2mg structure with sulfur atoms at $(0, y)$ $(1, \bar{y})$, $y \neq 0, \frac{1}{2}$ or 1. Structures with reasonable values for the x (in the case of the p1g1) and y coordinates of the sulfur atoms are shown for the three types in figs. 3 and 4. Of the three, the p1g1 seems the least likely, as it would require unsymmetrical interactions of the S atoms with neighboring Ir atoms. The structures shown in fig. 4a and b seem quite plausible, as S is known to adsorb in a three-fold site on Ni(111) [11].

A determination of the correct model of the three described above and of the coordinates of the S atoms within that model, will be made by a dynamical analysis of the LEED $I-V$ beam profiles [12].

References

[1] K. Christmann and G. Ertl, Z. Naturforsch. 28a (1973) 1144.
[2] H.P. Bonzel and R. Ku, J. Vacuum Sci. Technol. 9 (1972) 663.
[3] D.G. Fedak and N.A. Gjostein, Acta Met. 15 (1967) 827.
[4] C.-M. Chan, M.A. Van Hove, W.H. Weinberg and E.D. Williams, Phys. Rev. Letters, submitted.
[5] C.-M. Chan, M.A. Van Hove, W.H. Weinberg and E.D. Williams, in preparation.
[6] C.-M. Chan, S.L. Cunningham, K.L. Luke, W.H. Weinberg and S.P. Withrow, Surface Sci. 78 (1978) 15.
[7] C.-M. Chan, K.L. Luke, M.A. Van Hove, W.H. Weinberg and E.D. Williams, J. Vacuum Sci. Technol. (March/April, 1979).
[8] International Tables for X-Ray Crystallography, Vol. I (Kynoch, Birmingham, England, 1952).
[9] F. Tuinstra, Structural Aspects of the Allotropy of Sulfur and the other Divalent Elements (Waltman, Delft, Netherlands, 1967).
[10] M.K. Debe and D.A. King, Phys. Rev. Letters 39 (1977) 708.
[11] J.E. Demuth, D.W. Jepsen and P.M. Marcus, Phys. Rev. Letters 32 (1974) 1182.
[12] M.A. Van Hove, C.-M. Chan, E.D. Williams and W.H. Weinberg, in prepararion.

Section V

Computation of Profiles of Low-Energy Electron Diffraction Beams for Arrays of Ordered Islands

[This section will be published as a paper by E. D. Williams and W. H. Weinberg in *Surface Science* 110, 000 (1981).]

Abstract

In an attempt to determine the influence of the presence of adjacent islands on LEED beam profiles, an excluded area model has been proposed to describe the relative positions of ordered islands on a crystal surface. On the basis of this model, overlayers of different island density have been created on a finite lattice using a simple computer algorithm. The LEED from these overlayers has been calculated kinematically. Although the placement of the islands is not random, this does not perturb the LEED beam profile observably. Therefore, the kinematically diffracted intensity depends solely on the distribution of island sizes. Using this result, the intensity and half-width as functions of coverage have been calculated for one model of island growth.

1. Introduction

An attractive interaction between adatoms,* in combination with site-specific bonding, will give rise to the formation of ordered islands of adsorbate at small coverages if the temperature is sufficiently low. Evidence for such island formation has been observed in many experimental systems (*1 – 5*). To understand the thermodynamics and the adsorption and diffusion kinetics in an overlayer that contains islands, it is necessary to know the degree of order and the size and distribution of the islands (*6*). In principle, this information can be obtained using Low-Energy Electron Diffraction (LEED). Specifically, the shape of the diffracted electron beam is determined by the size and distribution of ordered regions of scatterers on the surface (*7 – 15*). A great deal of recent work concerning the quantitative analysis of LEED beam profiles has concentrated on the effects of surface steps on the diffracted beam (*10,13,14*).

It is easy to show that if the positions of ordered islands in an overlayer are random, then the fractional order beam profiles are equal to the weighted sum of the profiles of the individual islands on the surface (*7,15*). (An alternative derivation of this result is presented in the Appendix.) However, if the island positions are not random, but correlated with one another, this simple result will not hold as shown by the well-known phenomenon of beam splitting and streaking due to antiphase domains in overlayers *(8,9,11,15)*. For the correct determination of island size from LEED measurements, it is imperative to understand the effect of the distribution of island positions on the beam profile. To this end, a model for island position distribution is developed, and one- and two-dimensional overlayers based on

* The term "adatom" will be used to refer to any adsorbed species, atomic or molecular.

this model are generated. The LEED beam profiles for these overlayers are calculated kinematically to determine the effect that different degrees of correlation between island positions have on the profiles.

2. Model for Island Formation

A detailed description of overlayer formation would require a full molecular dynamics calculation taking into account the adsorption mechanism, gas pressure, surface temperature, adatom diffusion rate and substrate defect concentration. However, a qualitative understanding of the overlayer structure is possible from simple physical considerations. Computations of the LEED behavior from model overlayers based on such a qualitative understanding can be used to determine the amount of information available via LEED concerning the structure of the overlayer. For this purpose, an excluded area model of overlayer formation is proposed for overlayers in which there is island formation due to attractive interactions between adatoms.

During the early stages of overlayer formation, it is reasonable to assume that the atoms adsorb into sites of random position, but identical environment with respect to one another (i.e. bridge, on-top, etc.). Exceptions to this assumption are molecules with an extremely small probability of adsorption, or those that adsorb via a mobile precursor. For islands to form, some mobility of the adatoms following adsorption is required. If the adatoms are sufficiently mobile, they will move randomly about the surface until each (a) encounters another adatom and forms a pair (due to an attractive interaction) which has reduced mobility and will serve as a nucleus for an island; (b) is trapped at a defect, again forming an island nucleus; or (c) encounters

an already nucleated island and joins it. Statistically, those adatoms that adsorb initially near an island nucleus are more likely to join the preexisting island than to form a new nucleus. In a sense, then, once an island begins to form it acts as a sink for adatoms that adsorb nearby. For this reason, the distribution of island positions will not be random, but it will be governed by a weak excluded area effect. That is, there will tend to be a minimum distance between island centers. This minimum distance will be related to the mobility of the adatoms (which in turn may be limited by surface defects). Highly mobile adatoms may move long distances before joining an island and thus will form overlayers in which the islands are far apart. If the adatoms are of low mobility, small, closely-packed islands will result.

A computer algorithm was formulated to create island position distributions based on this excluded area model. Initially, a large number of adatoms was placed on a lattice representing the substrate at coordinates chosen using a random number generator. A section of the lattice, with the initial positions represented by x's is shown in Fig. 1. To determine island positions, this initial set of random adsorption sites was treated as follows. A subset of the sites was chosen arbitrarily, and all adatom positions within a distance r_{min} of each chosen site were found. The average position of the sites in each group was taken as a new site, and the original adatom positions were eliminated. This procedure was continued until all sites were separated by a distance of at least r_{min}. The "motion" of adatoms to a final nucleation site via this process is illustrated schematically by the arrows in Fig. 1. Once the island positions were fixed in this way, islands of any size, as shown by the circles in Fig. 1, could be placed on the lattice to form the overlayer. This algorithm was not meant to simulate island nucleation rigorously, but to provide an overlayer conforming to the excluded area

concept discussed above.

Island position distributions were created on 4000 × 4000 hexagonal lattices for three different values of r_{min}: 70, 35 and 21 substrate lattice spacings. Each set of island positions is characterized by the values of distances between nearest neighbor islands, as shown in Fig. 2. The histograms represent the probability of finding the nearest neighbor island at a distance, r, in any direction. Each histogram shows the average results from 16 to 36 independently created position distributions. Curve (a) is the result for a large value of r_{min}, which gives rise to a low density of islands. Curves (b) and (c) represent increasing densities of islands resulting from smaller values of r_{min}.

The rigid cutoff of the probability curves at r_{min} is nonphysical. In a real overlayer, a gradual tailing off at small values would occur. The use of this sharp cutoff causes a greater degree of long-range order in the island positions than would otherwise occur. Since the order of the island positions, as well as the order within the islands, determines the electron diffraction, the beam profiles for these calculated overlayers will have a greater dependence on the island position distribution than would occur for a physical overlayer.

3. Calculations of Beam Profiles

To determine the effect of an excluded area type distribution of island positions on the electron diffraction, LEED beam profiles were calculated for infinite one-dimensional and finite two-dimensional overlayers with the island position distributions shown in Fig. 2. In the one-dimensional case, the ordered islands had a structure of one scatterer on every third lattice

site. A $(\sqrt{3} \times \sqrt{3})R30°$ structure was used for the islands in the two-dimensional case.

Given the probability distribution for nearest neighbor island positions, the LEED beam profile can be calculated for a one-dimensional overlayer as has been shown by Houston and Park (*9,10*). In the case where all the islands are the same size and structure, the relevant equation is

$$I(K) = I_\Gamma(K) + I_\Gamma(K)\left[\frac{F[p_1(r)]}{1 - F[p_1(r)]} + \frac{F^*[p_1(r)]}{1 - F^*[p_1(r)]}\right] \qquad (1)$$

where $I_\Gamma(K)$ is the beam profile for a single island of size Γ; $p_1(r)$ is the normalized probability of finding the nearest neighbor island at a distance r; while F and F^* refer to the Fourier transform and its complex conjugate.

The LEED beam profile calculated in this way using the probability distribution of Fig. 2(c) is shown in Fig. 3. The dashed line represents the beam profile for the overlayer, and the solid line shows the profile for a single island. It is apparent that placing the islands in the one-dimensional array has very little effect on the beam profile. The beam profiles for arrays based on the distributions of Fig. 2(a) and (b), showed even smaller (but higher frequency) deviations from the single island beam profiles. These results are in contrast to results for islands separated by domain boundaries, where beam splitting was found for a similar distribution of nearest neighbor distances (*9*). The reason for the difference is that in this case the phase (domain) of each island is determined *independently* of the phase of adjacent islands. Only if adjacent islands are required to be out of phase does beam splitting occur for probability distributions of the width used here.

For a two-dimensional overlayer, the effect of the island position distribution on the beam profile should be even weaker than in one dimension due to

the extra degree of freedom. In other words, the probability distribution for finding the nearest neighbor island in any one direction on a two-dimensional overlayer will be broader and flatter than the distributions shown in Fig. 2. The beam profiles for two-dimensional arrays of islands were calculated directly using the island positions created as described in Section 2. The calculations can be done quite efficiently using the fact that the positions of all the scatterers in the overlayer can be represented as the convolution product

$$L(\vec{r}) = \sum_{\Gamma} j_{\Gamma}(\vec{r}) * l_{\Gamma}(\vec{r}) \qquad (2)$$

where $L(\vec{r})$ is a net of delta functions at the position of each scatterer in the overlayer; $j_{\Gamma}(\vec{r})$ is a net of delta functions at the position of each scatterer within an island of size Γ; $l_{\Gamma}(\vec{r})$ is a net of delta functions representing the positions of all islands of size Γ; and $*$ represents the convolution product.

The kinematic intensity is the absolute square of the Fourier transform of the positions of the scatterers. Using Eq. (2) and the property that the Fourier transform of a convolution product gives rise to a product of Fourier transforms, the intensity can be expressed as

$$I(\vec{K}) = \left| \sum_{\Gamma} F[j_{\Gamma}(\vec{r})] \times F[l_{\Gamma}(\vec{r})] \right|^2 \qquad (3)$$

This equation shows that the total diffracted intensity results from two separable terms. One term arises from the positions of the scatterers *within* the individual islands. The second depends only on the absolute positions of the island centers. This separability is useful in understanding the physical effects that determine diffraction from overlayers with islands.

Computations were first performed for overlayers in which all the islands were the same size. Somewhat surprisingly, it was found that the beam profiles calculated for individual 4000 × 4000 lattices were very noisy. The noise is believed to occur because a single lattice is not sufficiently large to represent a true statistical distribution of island positions. A similar effect has been seen in computer simulations of the LEED profile for a finite lattice with random displacements (*12*). To determine the beam profile, it was necessary to average the results for a large number (between 16 and 36) of overlayers. The criterion that beam profiles in different directions be the same was used to determine the extent of averaging required. More extensive averaging would reduce the noise level at the cost of greatly increasing the computational time.

The results of the computations for overlayers with all islands the same size are shown in Fig. 4. The points in the curves show the calculated beam profiles for three overlayers of absolute coverage approximately 0.07, with island position distributions corresponding to Fig. 2. The solid curves each represent the beam profile for a single island of the size present in that overlayer. The normalization factor for comparing the single island profiles to the overlayer profiles is the number of islands on the surface. To within the noise of the computation, the overlayer profile is identical to the single

island profile. This indicates that in spite of the excluded area constraint on the island positions, the island centers are acting as a randomly distributed set of scatterers that contribute a homogeneous background of constant intensity (*12*). The intensity profile due to a single island is then just multiplied with this background as in Eq. (3) to give the overall beam profile.

Beam profiles were also calculated for overlayers containing islands of different sizes. For a chosen distribution of island sizes, the smallest islands were placed at positions that had the closest neighbor islands, and similarly for increasing island sizes. Representative results of these calculations are shown in Fig. 5. Again, the points show the result of the computation. The solid lines were calculated according to

$$I(\vec{K}) = N \sum_{\Gamma} P(\Gamma)\, I_{\Gamma}(\vec{K}) \qquad (4)$$

where N is the number of islands, and $P(\Gamma)$ is the probability of occurrence of an island of size Γ. This equation can be derived rigorously, given the assumptions that the islands are distributed randomly (*7,15*) and that the distributions for islands of different size are independent. As shown in the Appendix, the cross terms in islands of different size that arise from an expansion of Eq. (3) contribute intensity only in the specular direction, given these assumptions. It can be seen in Fig. 5 that, as before, the island distribution does not affect the shape of the beam profile. As mentioned in Section 2, the calculated island distributions used here should have a stronger influence on the beam profile than would a physical distribution. This result, therefore, can be extrapolated safely to physical systems.

The peak intensity of a diffraction beam for an island containing N_{Γ} ordered scatterers is N_{Γ}^2. Therefore, the largest islands will influence the shape of the beam profile most strongly. Empirically, it has been found that

the full-width at half-maximum, W, of a beam profile for an overlayer of mixed island sizes can be approximated by

$$W \approx \sum_{\Gamma} P(\Gamma)\, N_{\Gamma}^2\, W_{\Gamma} / \sum_{\Gamma} P(\Gamma)\, N_{\Gamma}^2 \qquad (5)$$

where N_{Γ} is the number of scatterers in an island of size Γ; and W_{Γ} is the *FWHM* for a beam profile from an island of size Γ. Comparison of the *FWHM* calculated using this approximate expression and that determined from profiles calculated according to Eq. 4 has been carried out for twenty arbitrary distributions and ten ball-in-urn distributions (next section). The comparison was quite favorable with the values from Eq. (5) ranging from 1 to 10% higher than those from Eq. (4), for values of the FWHM from 0.01 to 0.06 l. s.$^{-1}$.

From Eq. (5), it is clear that an experimental determination of the *FWHM* will not refer to the mean island diameter on the surface but will be weighted heavily to the largest islands present. To the extent that the effects of multiple scattering (*13,16*) and instrumental limitations (*17,18*) allow, a detailed analysis of the line shape according to Eq. (4) can provide more information concerning the size distribution. In particular, a distribution containing many small islands will give rise to broad wings on the beam profile.

4. Coverage Dependence of Beam Profiles

LEED intensity as a function of coverage is frequently measured experimentally. Given a model for the island size distribution as a function of coverage, Eq. (4) can be used to calculate the beam profile and relative kinematical intensity at different coverages. For comparison with experiment, the calculated profile must be convoluted with the appropriate instrument

response function (*17,18*).

A model for island nucleation and growth should account for the formation of new islands with decreasing frequency as coverage increases, and an increasing mean island size with coverage. These characteristics can be described to zeroth order with a ball-in-urn model. The "urns" are island nucleation sites, of which there will be a characteristic number, M, depending both on the nature of the surface and the adsorbate. During adsorption, the adatoms will be distributed randomly among these sites. The number of ways that a given number of adatoms, n, can be distributed among the M sites is (*19*)

$$\Omega\ (M,n) = \frac{(M-1+n)!}{(M-1)!\,n!}. \tag{6}$$

The number of times that a nucleation site is occupied by an island containing l adatoms for all $\Omega\ (M,n)$ configurations is

$$\Omega'\,(M,n,l) = M\frac{(M-2+n-l)!}{(M-2)!\,(n-l)!}. \tag{7}$$

The frequency of observing an island of size l then is

$$F(l) = \Omega'\,(M,n,l)\,/\,M\ \Omega\ (M,n)\,. \tag{8}$$

According to this model, the most frequently occurring single island size is $l = 0$. The most probable size island for a given adatom to be in, however, is $l \approx n/M$ (for $n >> M$).

To predict the coverage dependence of the LEED behavior according to the ball-in-urn model, a finite number of island sizes was chosen. The probability of occurrence of each size was calculated based on Eq. (8) for different values of n. The island site density was chosen to be M = 3600 sites on a 4000 × 4000 lattice. Once the set of probabilities was determined, Eq. (4) was

used to calculate the beam profile. The calculations were carried out up to an absolute coverage of $\Theta = 0.137$. The optimum coverage for the $(\sqrt{3} \times \sqrt{3})R30°$ structure is $\Theta = 0.333$, so at $\Theta = 0.137$ somewhat less than half the surface is covered by islands. At this extent of coverage, experience from the computer calculations of Section 3 has shown that adjacent islands begin to coalesce. When this happens, neither the model for island growth nor the assumption of round islands is valid any longer.

To simulate the effect of instrumental broadening, the calculated profiles were convoluted with Gaussian functions of different widths. The property that the beam is isotropic was used to carry out a full two-dimensional convolution (*20*). The values of the intensity at $\Delta b^* = 0$ [the center of the $\sqrt{3} \times \sqrt{3})R30°$ beam] for different instrumental widths are plotted as a function of coverage in Fig. 6. Each curve has been independently normalized to unity at $\Theta = 0.137$. In Fig. 7, the corresponding widths of the beams are shown. It is clear, as has been pointed out previously (*17,18*), that instrumental broadening is a major barrier to extracting information concerning the overlayer. Even without broadening, however, Eqs. (4) and (5) remain only two equations in many unknowns [the set $P(\Gamma)$]. Comparison of calculated curves, as in Figs. 6 and 7, with experiment can serve as a check on a proposed model of island growth but not as a proof of its correctness.

The ball-in-urn model is a useful starting point for considering island growth due to its simplicity. There are two points in which the model fails to describe the island growth adequately, however. First, the model treats islands of all sizes (including "islands" with only one adatom) on an equal footing. In fact, very small islands will be less favorable energetically than larger islands, and they will be more likely to lose adatoms which may then migrate to larger islands. In addition, the model does not take into

consideration the greater probability of a migrating adatom encountering the more extensive edge of a large island than a small island. For both reasons, the ball-in-urn model will predict distributions that are too heavily weighted toward small islands. The physical factors that must be considered in any attempt to model island growth quantitatively have been discussed by Lagally *et al. (21)*.

5. Conclusions

For simulated island containing overlayers, no perturbation (streaking, splitting, etc.) of the shape of the diffracted beam profile occurs, even for overlayers for which the mean first neighbor distance between island centers is as small as thirty lattice spacings. This result, which is independent of any arguments concerning instrumental broadening, is valid so long as there is no correlation between the phases (domains) of different islands. Beam profiles for islands containing overlayers may be described as the sum of the profiles due to the individual islands present [Eq. (4)]. The mathematical derivation of this result requires the islands to be positioned randomly. However, the results of this study indicate that this is a weak requirement. Even overlayers with a relatively strong correlation between nearest neighbor island positions (see Fig. 2) appear to be random insofar as their effect on the beam profile is concerned.

Since the intensity for the profile from an individual island scales as the number of scatterers in the island squared, the largest islands in a distribution will influence the beam profile far more heavily than the small islands. For this reason, the width of the overall profile will not reflect the mean island diameter. Determination of the mean size will be model dependent if

only the *FWHM* is known. Analysis of the shape of the beam profile, particularly its wings, can provide additional information concerning the island size distribution.

APPENDIX

Beam Profiles for Random Arrays of Ordered Islands

The overall LEED intensity is (to within a constant of proportionality)

$$I(\bar{K}) = \left| F\left[L(\bar{r})\right]\right|^2 \tag{A1}$$

where $L(\bar{r})$ is the position distribution (a net of delta functions) of the scatterers. If the scatterers are arranged in islands of size Γ,

$$L(\bar{r}) = \sum_{\Gamma} j_{\Gamma}(\bar{r}) * l_{\Gamma}(\bar{r}) \tag{A2}$$

where $l_{\Gamma}(\bar{r})$ is the position distribution of the island centers, $j_{\Gamma}(\bar{r})$ describes the positions of the scatterers within an island of size Γ with respect to the center of the island and $*$ represents the convolution product. Combining Eqs. (A1) and (A2) gives

$$I(\bar{K}) = \left| \sum_{\Gamma} F\left[j_{\Gamma}(\bar{r})\right] \times F\left[l_{\Gamma}(\bar{r})\right]\right|^2 . \tag{A3}$$

Consider first the case where there is only one island size, Γ'. Then Eq. (A3) becomes

$$I(\bar{K}) = I_{\Gamma'}(\bar{k}) \times \left| F[l_{\Gamma'}(\bar{r})]\right|^2 \tag{A4}$$

where $I_{\Gamma'}(K) = \left| F[j_{\Gamma'}(\bar{r})]\right|^2$ is the intensity due to a single island of size Γ'. The second term on the right in Eq. (A4) is equal to the Fourier transform of the autocorrelation function of $l_{\Gamma'}(\bar{r})$

$$\left| F[l_{\Gamma'}(\bar{r})]\right|^2 = F[l_{\Gamma'}(\bar{r}) * l_{\Gamma'}(\bar{r})] \tag{A5}$$

where $*$ indicates the correlation product,

$$l_{\Gamma'}(\bar{r}) * l_{\Gamma'}(\bar{r}) = \int l_{\Gamma'}(\bar{\tau}) l_{\Gamma'}(\bar{r} + \bar{\tau}) d\bar{\tau} \ .$$

Defining the positions of the islands as the set $\bar{a}_i$,

$$l_{\Gamma'}(\bar{r}) = \sum_{i=1}^{N} \delta(\bar{r} - \bar{a}_i)$$

where N is the number of islands, the correlation product is

$$\int \sum \delta(\bar{\tau} - \bar{a}_i) \sum \delta(\bar{r} + \bar{\tau} - \bar{a}_i) d\bar{\tau} = \int [\delta(\bar{\tau} - \bar{a}_1)\delta(\bar{r} + \bar{\tau} - \bar{a}_1)$$

$$+ \delta(\bar{\tau} - \bar{a}_1)\delta(\bar{r} + \bar{\tau} - \bar{a}_2) + \cdots + \delta(\bar{\tau} - \bar{a}_N)\delta(\bar{r} + \bar{\tau} - \bar{a}_N)] d\bar{\tau}.$$

This equation simplifies to give

$$l_{\Gamma'}(\bar{r}) * l_{\Gamma'}(\bar{r}) = \sum_{i=1}^{N} \sum_{j=1}^{N} \delta(\bar{r} + \bar{a}_i - \bar{a}_j) = N\delta(\bar{r}) + \sum_{i \neq j}^{N} \sum \delta(\bar{r} + \bar{a}_i - \bar{a}_j) \quad \text{(A6)}$$

Taking the Fourier transform gives

$$F[N\delta(\bar{r})] = N$$

for the first term, and

$$\int e^{i\bar{k}\cdot\bar{r}} \sum_{i \neq j}^{N} \sum \delta(\bar{r} + \bar{a}_i - \bar{a}_j) d\bar{r} = \sum_{i \neq j}^{N} \sum e^{i\bar{k}\cdot(\bar{a}_i - \bar{a}_j)}$$

for the second. For $N \to \infty$, the second term will be zero for $\bar{k} \neq 0$, and N(N - 1) for $\bar{k} = 0$. Therefore,

$$|F[l_{\Gamma'}(\bar{r})]|^2 = N + N(N-1)\delta(\bar{K}) \quad \text{(A7)}$$

and

$$I(\bar{K}) = I_{\Gamma'}(\bar{K}) \times [N + N(N-1)\delta(\bar{K})] \quad \text{(A8)}$$

In the case where there are islands of different sizes present, expansion of Eq. (A3) will give a 'self' term like Eq. (A4) for each value of Γ, as well as cross terms of the form

$$F[j_\Gamma(\bar{r})F^*[j_{\Gamma'}(\bar{r})]F[l_\Gamma(\bar{r})]F^*[l_{\Gamma'}(\bar{r})] \ ,$$

which can be written as

$$F[j_{\Gamma'}(\bar{r}) * j_\Gamma(\bar{r})] \times F[l_\Gamma(\bar{r}) * l_{\Gamma'}(\bar{r})] \ .$$

If each set of $l_\Gamma(\bar{r})$ represents a random distribution, then the 'self' terms give

$$I^{self}(\bar{k}) = \sum_\Gamma I_\Gamma(\bar{k})(N_\Gamma + N_\Gamma(N_\Gamma - 1)\delta(\bar{k})) \qquad \text{(A9)}$$

where N_Γ is the number of islands of size Γ. If, in addition to being random, the sets $l_\Gamma(\bar{r})$ are *independent of one another*, then the correlation product of l_Γ and $l_{\Gamma'}$, which appears in the cross terms,

$$l_\Gamma(\bar{r}) * l_{\Gamma'}(\bar{r}) = \sum_{i=1}^{N_{\Gamma'}} \sum_{j=1}^{N_\Gamma} \delta(\bar{r} + a_j - a_i')$$

has no special behavior at j = i. Therefore, no special term in $\delta(r)$ arises and by the reasoning leading to Eq. (A7), the cross terms have the form

$$F[j_\Gamma(\bar{r}) * j_{\Gamma'}(\bar{r})] \times [N_\Gamma N_{\Gamma'}\delta(\bar{K})] \ ,$$

and contribute intensity only in the specular direction as indicated by the factor $\delta(\bar{K})$. The total intensity is the sum of Eq. (A9) and all cross terms and thus is

$$I(\bar{K}) = \sum_\Gamma N_\Gamma I_\Gamma(\bar{K}) + \text{specular scattering} \ . \qquad \text{(A10)}$$

This result is the same as Eq. (4). It is valid for an island distribution for

which the distribution of positions of islands of each size is random and independent of the distributions of islands of other sizes.

Acknowledgments

We gratefully acknowledge A. C. Sobrero for helpful discussions in the course of preparation of this manuscript. This research was supported by the Army Research Office under Grant No. DAAG29-79-C-0132. The research reported in this paper made use of the Dreyfus-NSF Theoretical Chemistry Computer which was funded through grants from the Camille and Henry Dreyfus Foundation, the National Science Foundation (Grant No. CHE78-20235), and the Sloan Fund of the California Institute of Technology.

References

1. H. Pfnür, P. Feulner, H. A. Engelhardt and D. Menzel, Chem. Phys. Letters *59*, 481 (1978).
2. J. M. Hoffman, A. Ortega, H. Pfnür, D. Menzel and A. M. Bradshaw, J. Vacuum Sci. Technol. *17*, 239 (1980).
3. M. G. Lagally, T.-M. Lu and G.-C. Wang, in *Ordering in Two Dimensions*, ed. S. Sinha, Elsevier, 1980, and references therein.
4. L. D. Roelofs, T. L. Einstein, P. E. Hunter, A. R. Kortan, R. L. Park and R. M. Roberts, J. Vacuum Sci. Technol. *17*, 231 (1980).
5. A. Crossley and D. A. King, Surface Sci., in press (1980).
6. M. G. Lagally, T.-M. Lu and D. G. Welkie, J. Vacuum Sci. Technol. *17*, 223 (1980).
7. J. C. Tracy and J. M. Blakely, in *The Structure and Chemistry of Solid Surfaces*, ed. G. A. Somorjai, John Wiley and Sons, Inc., New York, 1969.
8. C. S. McKee, D. L. Perry and M. W. Roberts, Surface Sci. *39*, 176 (1973).
9. J. E. Houston and R. L. Park, Surface Sci. *21*, 209 (1970).
10. J. E. Houston and R. L. Park, Surface Sci. *26*, 269 (1971).
11. G. Ertl and J. Küppers, *Low Energy Electrons and Surface Chemistry*, Verlag Chemie, Weinham, 1974.
12. M. Henzler, in *Electron Spectroscopy for Surface Analysis*, ed. H. Ibach, Springer-Verlag, Berlin, 1977, p. 117.
13. M. Henzler, Surface Sci. *73*, 240 (1978).
14. T.-M. Lu, S. R. Anderson, M. G. Lagally and G.-C. Wang, J. Vacuum Sci. Technol. *17*, 207 (1980).
15. T.-M. Lu, G.-C. Wang and M. G. Lagally, Surface Sci., in press (1981).

16. W. Moritz, in *Electron Diffraction* 1927–77, eds. P. J. Dobson, J. B. Pendry and C. J. Humphreys, The Institute of Physics, London, 1977, p. 261.

17. R. L. Park, J. E. Houston and D. G. Schreiner, Rev. Sci. Instrum. *42*, 60 (1971).

18. G.-C. Wang and M. G. Lagally, Surface Sci. *81*, 69 (1979).

19. J. Mathews and R. L. Walker, *Mathematical Methods of Physics*, W. A. Benjamin, Inc., Menlo Park, CA, 1970, p. 377.

20. E. D. Williams and W. H. Weinberg, in *Proc. Fourth Internat. Conf. Solid Surfaces*, p. 311 (1980).

21. M. G. Lagally, G.-C. Wang and T.-M. Lu, CRC Crit. Rev. Sol. State Mat. Sci. *1*, 233 (1978).

Figure Captions

Fig. 1: Creation of an overlayer with an excluded area about each island site. x's represent intial random locations of adatoms. Arrows show motion of nearby adatoms to a mean site which becomes the island position. Circles show islands centered at the resulting locations. $\underline{r}$ is the vector between nearest neighbor islands.

Fig. 2: The probability of finding the nearest neighbor island at a distance, r, in any direction, for overlayers of three densities created on 4000 x 4000 lattices. (a) r_{min} = 70 substrate lattice spacings (l.s.), number of islands = 983 ± 15; (b) r_{min} = 35 l.s., number of islands = 3551 ± 25; (c) r_{min} = 21 l.s., number of islands = 8953 ± 51. Each histogram has been normalized so that $\int_0^\infty p_1(r)dr = 1$.

Fig. 3: Beam profile for a one-dimensional array of ordered islands based on the distribution of Fig. 2(c). All islands are the same size, containing six scatterers, one on every third substrate site. The approximate absolute coverage (number of adatoms per substrate atom) is Θ = 0.23, the approximate relative coverage (fully ordered overlayer corresponds to Θ = 1.0) is Θ = 0.69. Dashed line is the profile for the array, solid line is the profile for a single island. The reciprocal space vector, b^*, is in units of reciprocal substrate lattice spacings, $(l.s.)^{-1}$.

Fig. 4: Beam profiles for arrays of uniform island size, compared with the profile of a single island of the same size. (a) Average of profiles from 36 overlayers with position distribution as in Fig. 2(a). Islands are 62 substrate lattice spacings (l.s.) in diameter, Θ = 0.071; Θ = 0.21. (b) Average of 36 as per Fig. 2(b), islands 31

l.s. in diameter, $\Theta = 0.066$; $\Theta = 0.20$. (c) Average of 16 as per Fig. 2(c), islands 21 l.s. in diameter, $\Theta = 0.071$; $\Theta = 0.21$ b^* is the $(\sqrt{3} \times \sqrt{3})R3$ 0° reciprocal space vector. The units are in terms of reciprocal substrate lattice spacings, $(l.s.)^{-1}$.

Fig. 5: Beam profiles for arrays of mixed island size. The position distributions correspond to those in Fig. 2(a). (a) Islands of diameter 35, 38, 42, 45 and 48 l.s. occurring with equal probability. (b) Islands of diameter of 48, 55 and 62 l.s. occurring with probabilities 0.2, 0.6 and 0.2, respectively.

Fig. 6: Intensity as a function of coverage for island growth via a ball-in-urn model. Circles, O, no instrumental broadening; x's instrumental width 0.010 $(l.s.)^{-1}$; squares, ▪ , instrumental width 0.030 $(l.s.)^{-1}$; triangles, Δ, instrumental width 0.050 $(l.s.)^{-1}$. Each curve has been normalized independently to unity at $\Theta = 0.137$.

Fig. 7: FWHM as a function of coverage for island growth via a ball-in-urn model. Symbols as in Fig. 6.

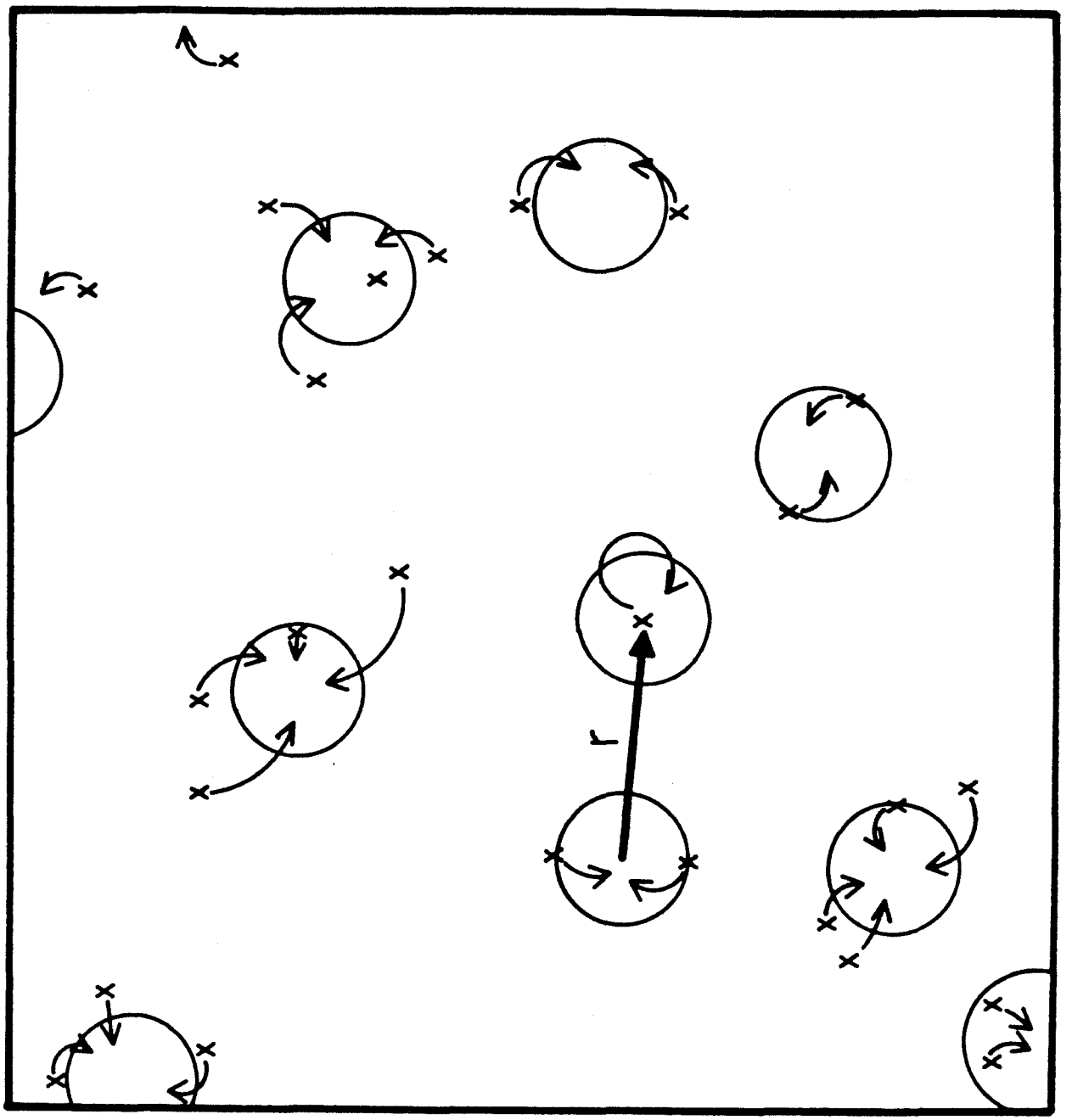

Figure 1

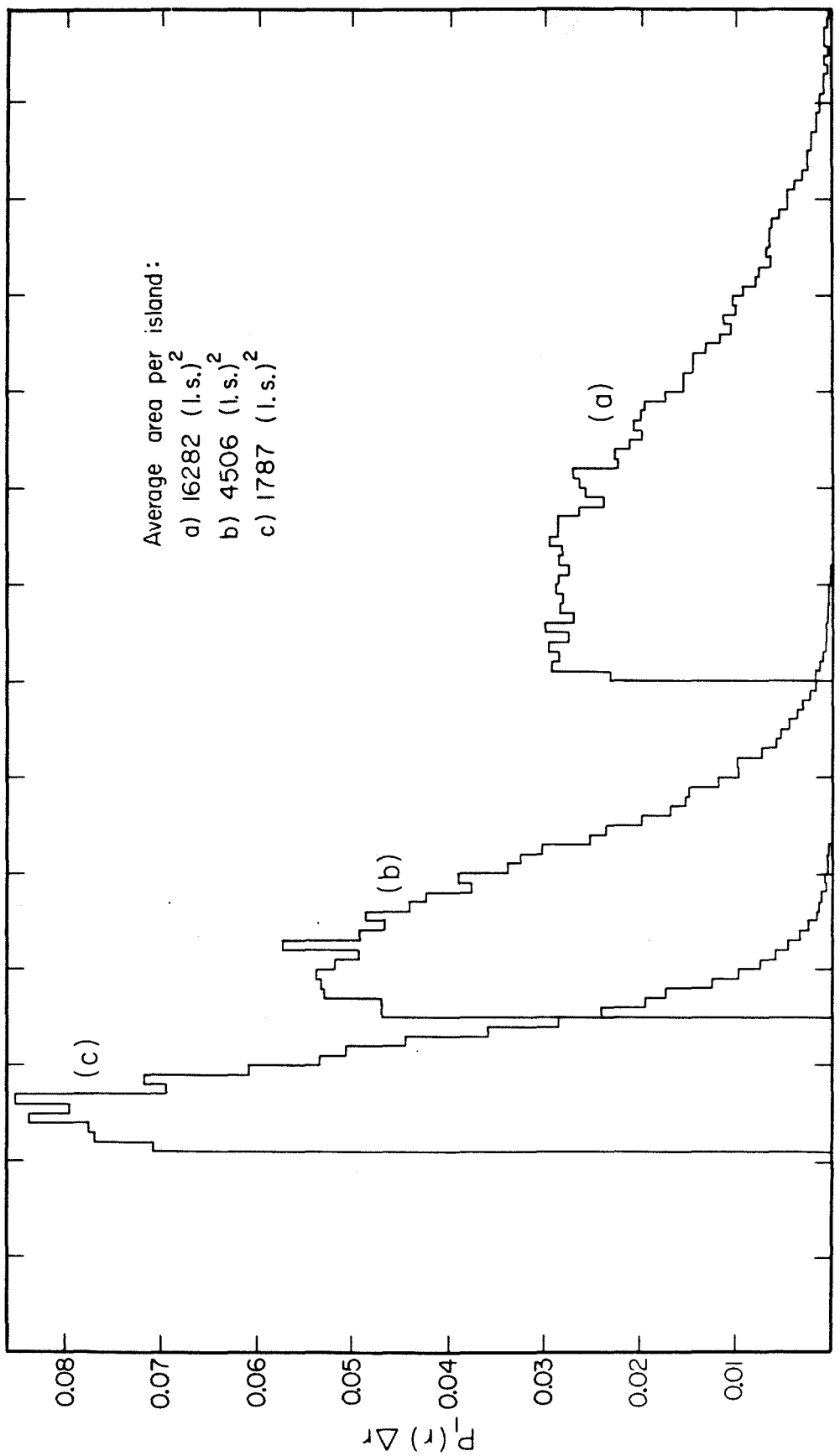
Average area per island:
a) 16282 (l.s.)^2
b) 4506 (l.s.)^2
c) 1787 (l.s.)^2
(a)
(b)
(c)
$\bar{P}_1(r)\,\Delta r$
0.08
0.07
0.06
0.05
0.04
0.03
0.02
0.01
10
20
30
40
50
60
70
80
90
100
110
120
130
Distance to nearest neighbor island, l.s.

Figure 2

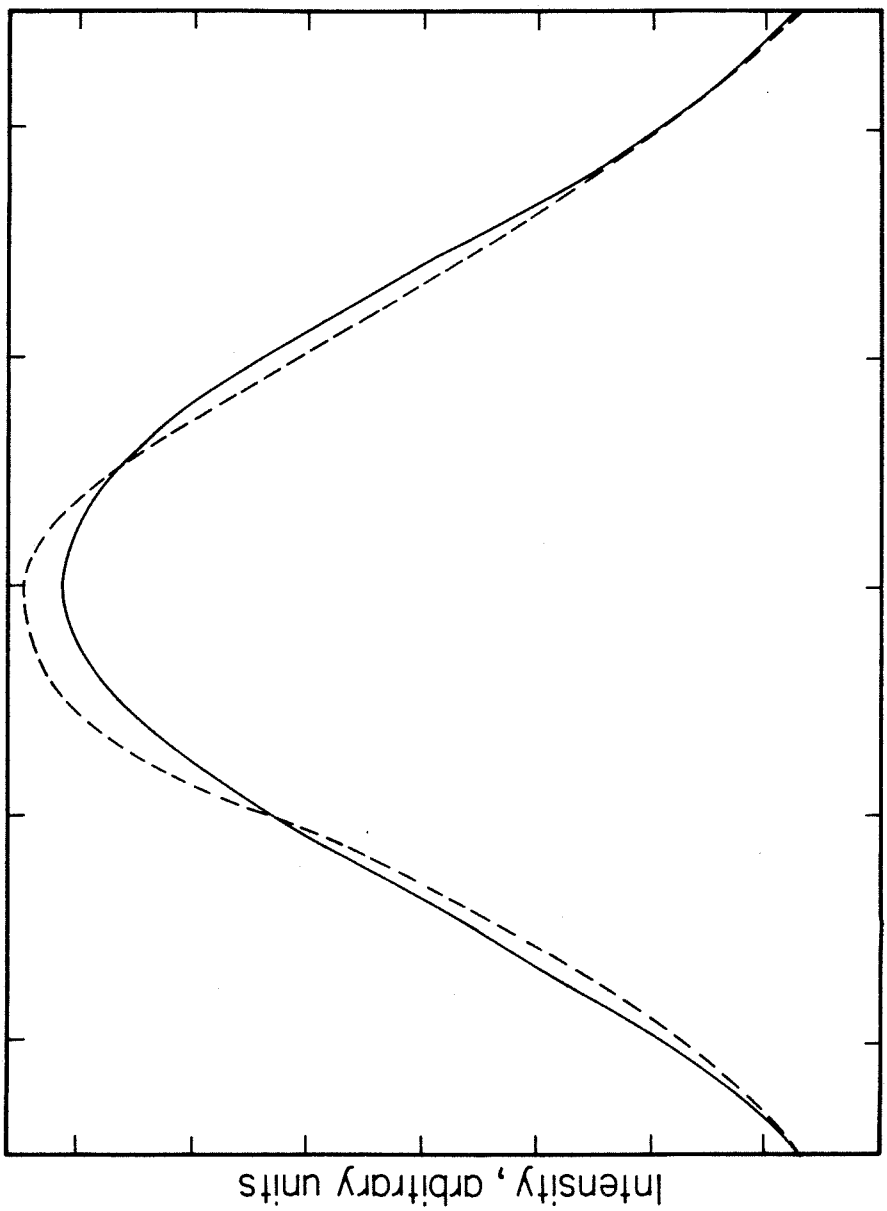

Figure 3

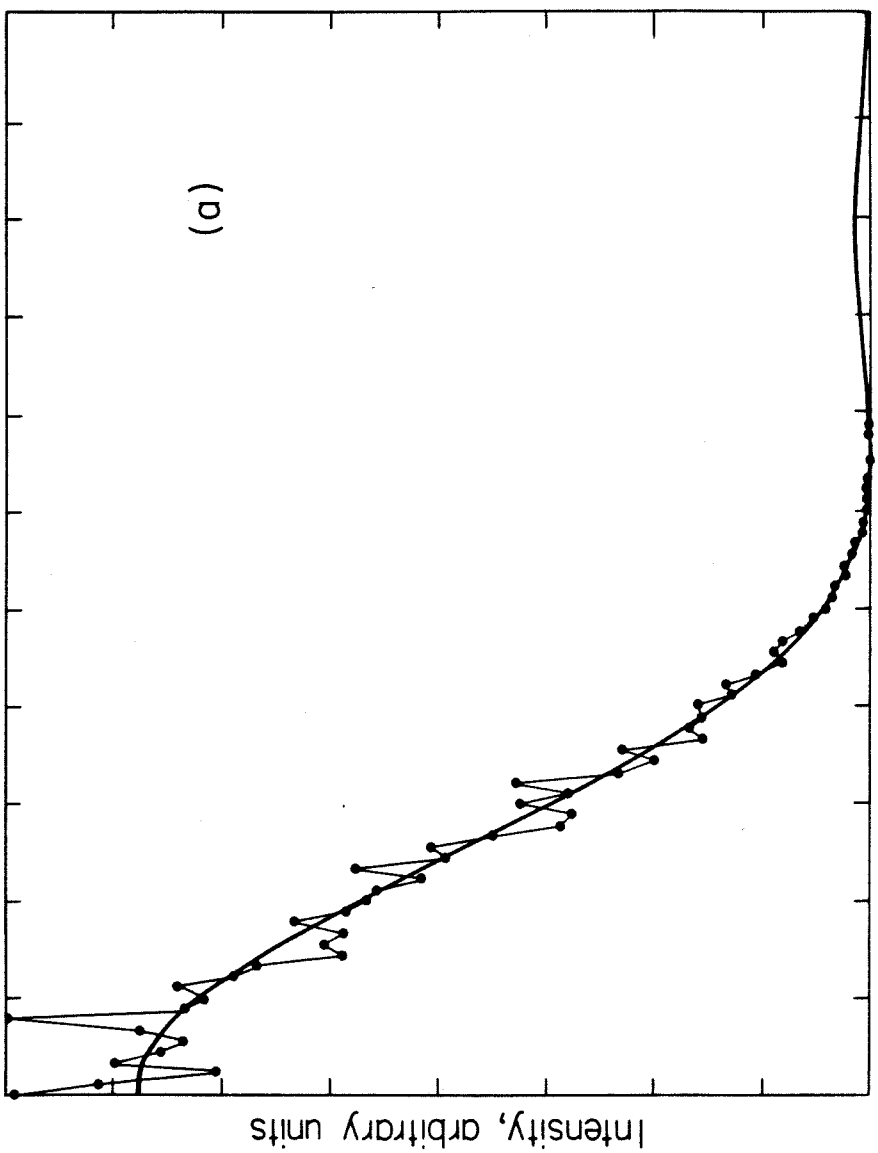
(a)
Intensity, arbitrary units
0.006
0.012
0.018
0.024
0.030
Δb^*, (l.s.)$^{-1}$

Figure 4a

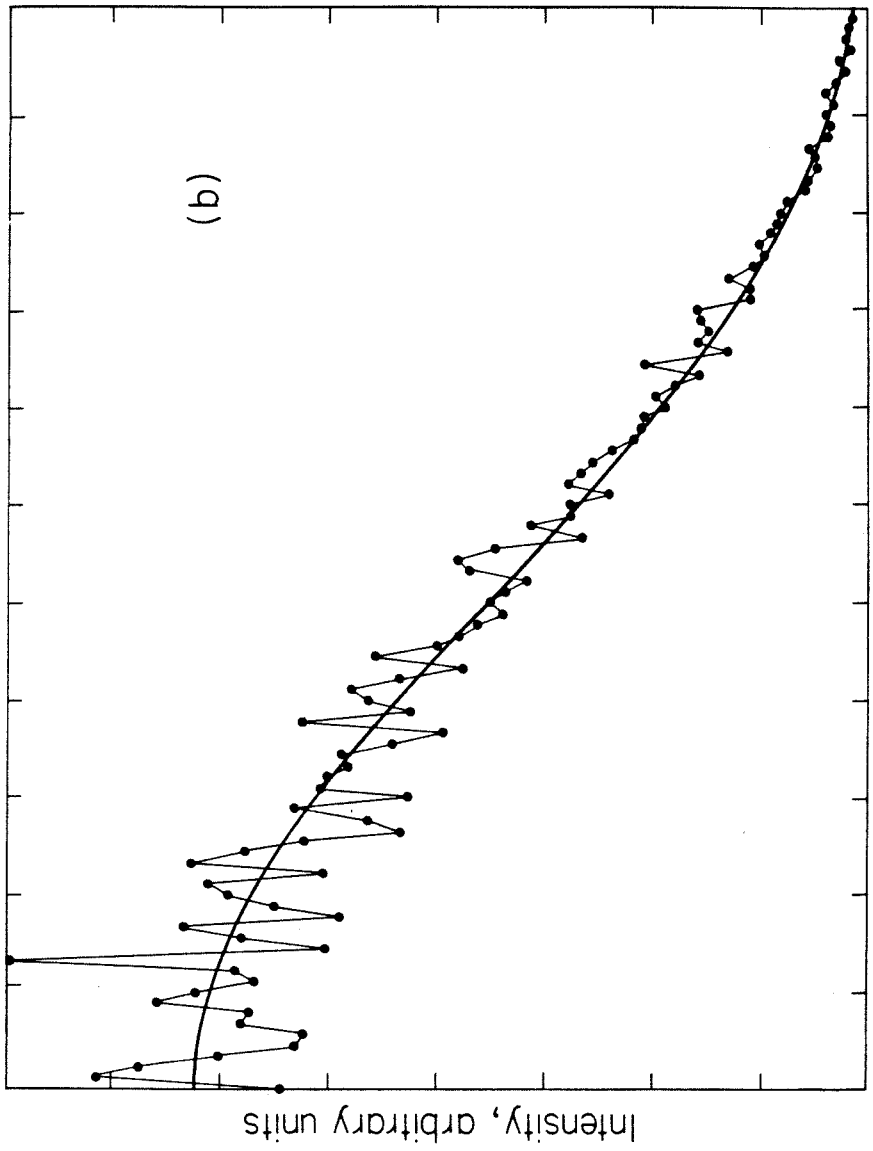
(b)
Intensity, arbitrary units
0.006
0.012
0.018
0.024
0.030
Δb^*, (l. s.)$^{-1}$

Figure 4b

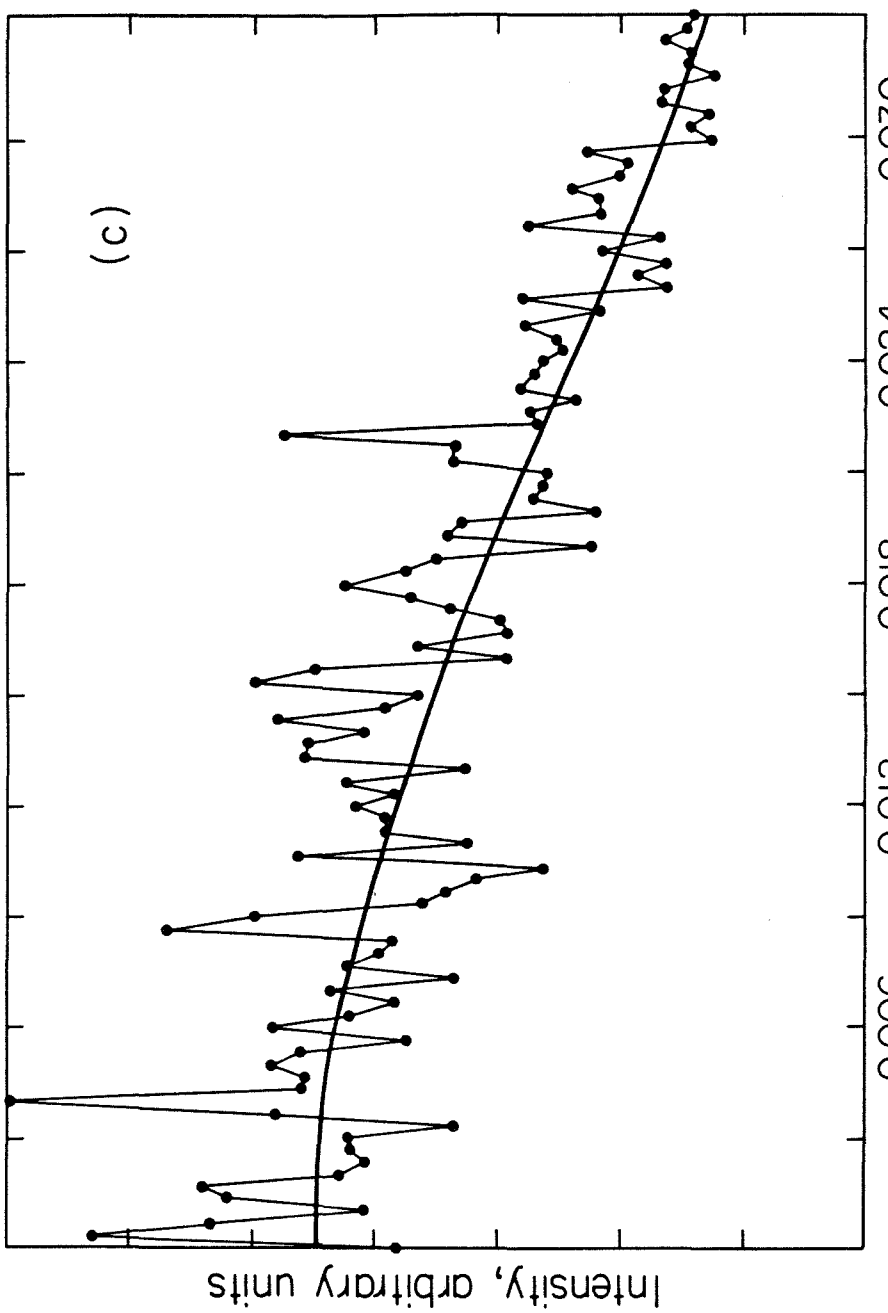

Figure 4c

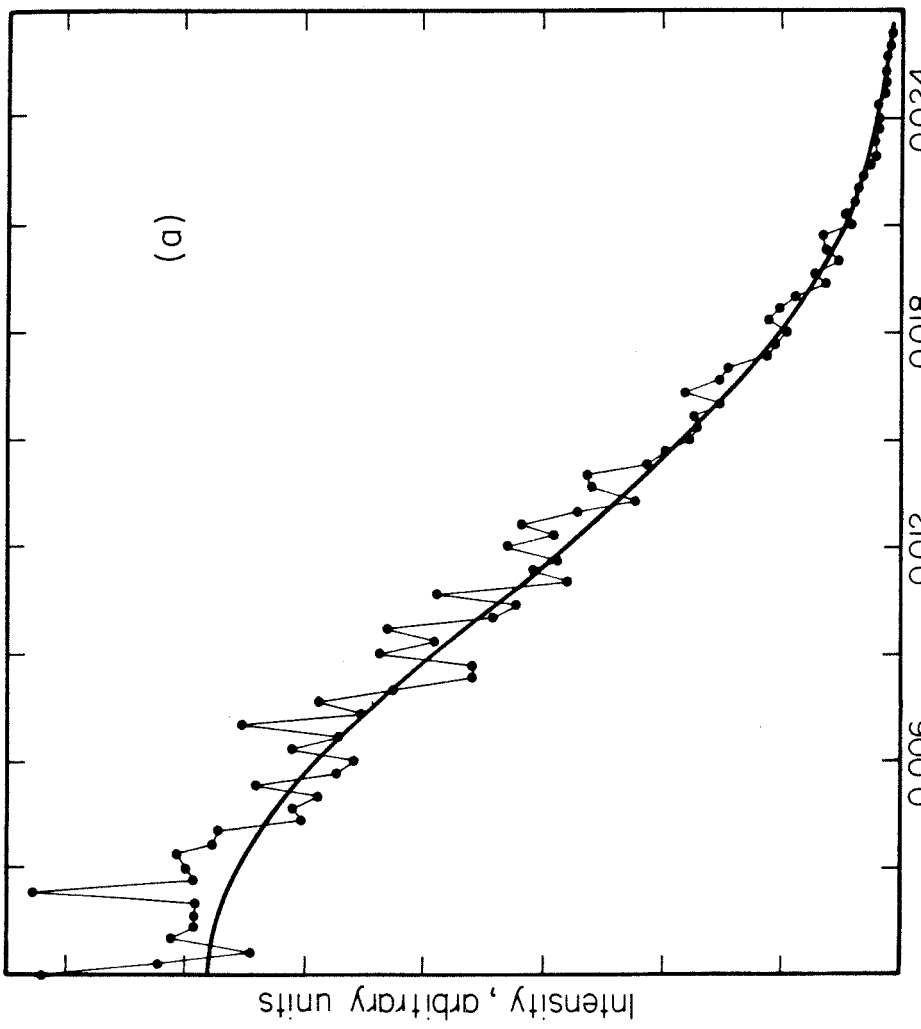

Figure 5a

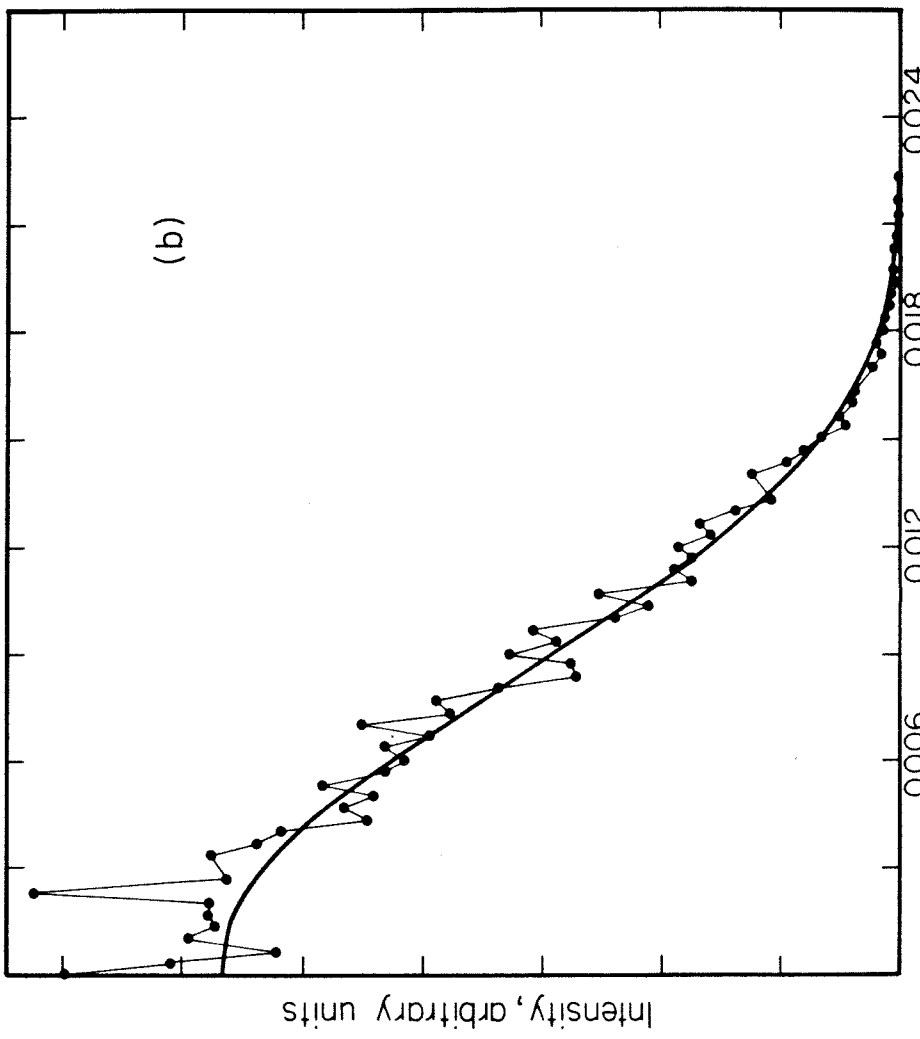

Figure 5b

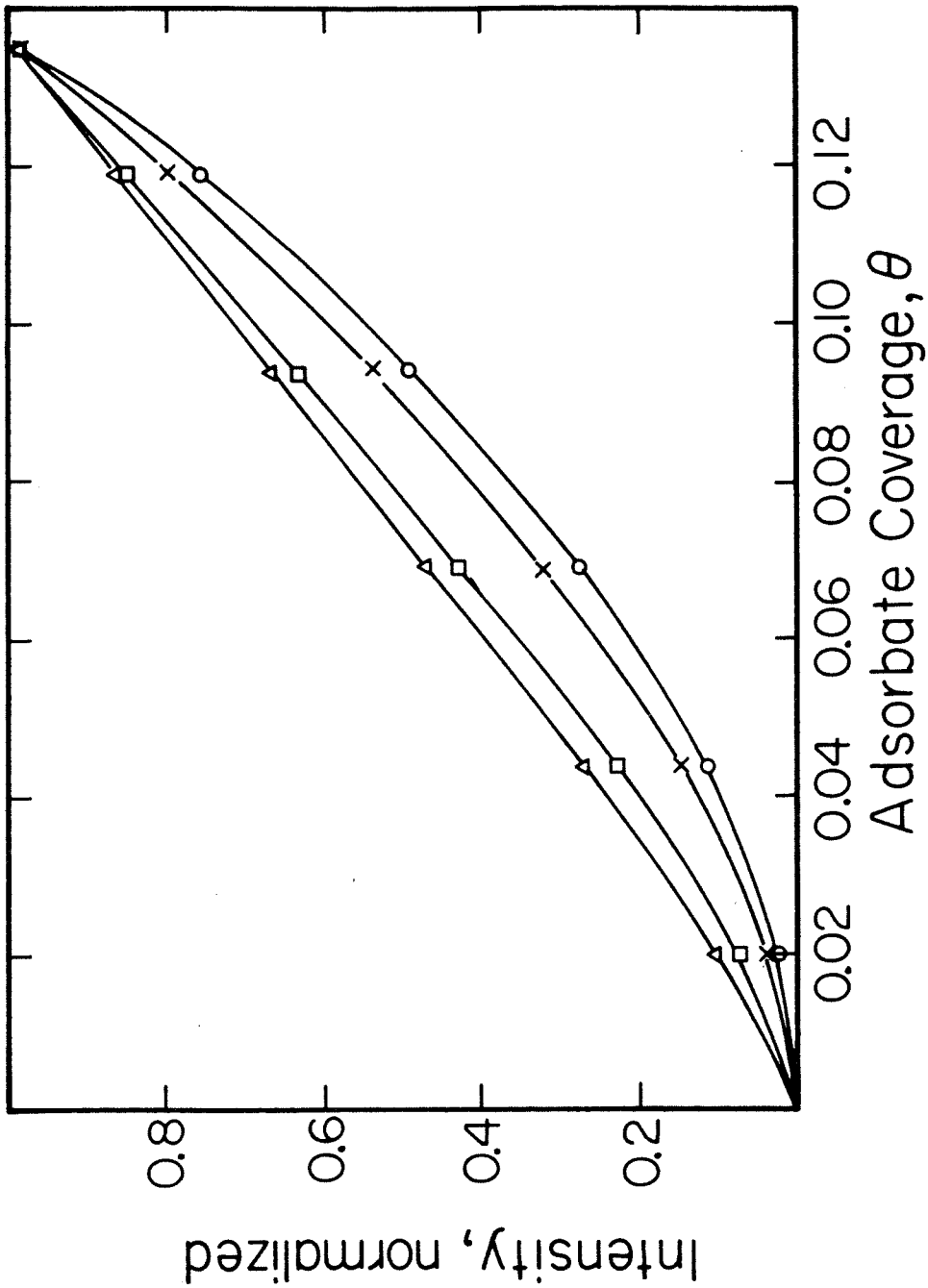
Intensity, normalized
0.2
0.4
0.6
0.8
Adsorbate Coverage, θ
0.02
0.04
0.06
0.08
0.10
0.12

Figure 6

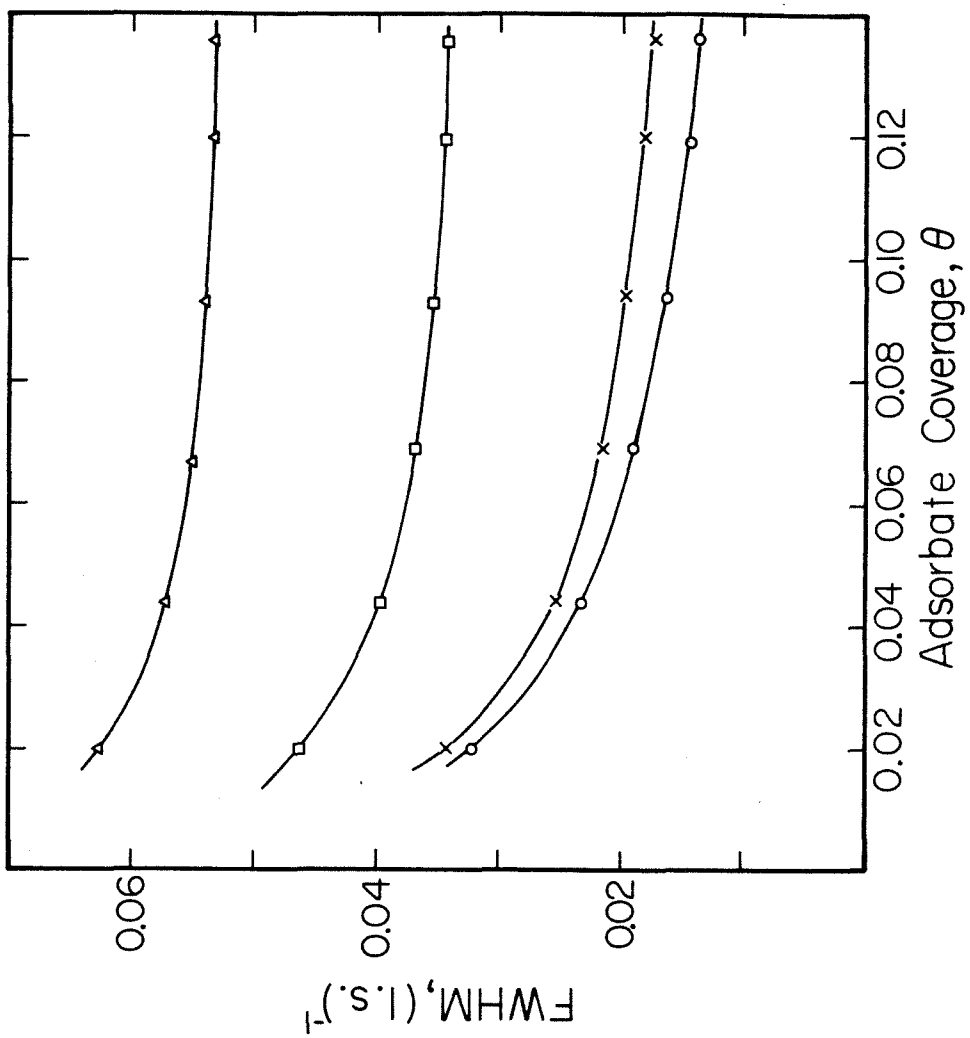
FWHM, (l.s.)⁻¹
0.06
0.04
0.02
0.02
0.04
0.06
0.08
0.10
0.12
Adsorbate Coverage, θ

Figure 7

Section VI

CO on Ru(001): Island Formation and Disordering

1. Introduction

2. Experimental Methods

3. Experimental Results

   A. Instrument Response and Step Density
   B. Beam Profiles of the CO Overlayer
   C. Temperature Dependence of the CO Overlayer

4. Analysis and Discussion

   A. Island Sizes
   B. Disordering and Island Size
   C. Comparison with Phase Diagrams

5. Conclusions

Abstract

Low energy electron diffraction (LEED) has been used to study the influence of steps and of temperature variation on the formation of ordered islands of CO on the (001) surface of ruthenium. The clean surface was found to have steps two atoms (one hcp unit cell) high separated by terraces of average width 270 Å or 135 Å (depending on the model used for analysis). Widths of the beam profiles for the CO overlayer were measured as a function of coverage at 100 K and 310 K. It was not possible to fit the coverage dependence of the beam width using a step limited model of island formation. The temperature dependence of the overlayer was measured also. The frequency of the frustrated translational motion of the CO admolecules parallel to the surface is estimated to be 45 cm^{-1}. At fractional coverages up to 1/6, the ordered islands of CO begin to disorder below the desorption temperature. The disordering behavior is inconsistent with a step-limited model of island formation. For nonstep-limited islands, the disordering behavior depends strongly on the distribution of sizes of islands in the overlayer. The correct distribution was determined and used to calculate the mean size of islands on the surface as a function of coverage.

1. Introduction

The interactions among chemically adsorbed molecules are of both practical and theoretical interest. In practical terms, lateral interactions clearly affect the diffusion and reaction of chemically adsorbed molecules **(1)**. The theoretical interest in lateral interactions arises because they represent a type of molecular interaction not observed in homogeneous systems. Interactions among chemically adsorbed molecules can arise as a result of a perturbation of the electrons of the metal near the surface or an elastic distortion of the surface by the adsorbed species **(2-9)**. The effects of lateral interactions are manifest in vibrational spectra of chemisorbed overlayers **(10,11)**, in thermal desorption mass spectrometry **(12,13)**, and, most strikingly, in low-energy electron diffraction (LEED) **(14)**. Each of these measurements offers a different potential for the determination of lateral interaction energies. Only qualitative information is available via vibrational spectroscopies. Proper analysis of thermal desorption mass spectra allows the estimation of net attractive and repulsive interaction energies in overlayers. LEED, however, offers the possibility of determining both the size and directional dependence of the microscopic lateral interactions between chemisorbed species.

When molecules adsorb onto the regular array of binding sites of a single crystal surface, they often form ordered overlayers, observable by LEED, which have a periodicity greater than that of the substrate. This is a direct consequence of lateral interactions. The geometry of the overlayer provides immediate qualitative information concerning the interactions. Repulsive interactions tend to cause vacancies in sites adjacent to an occupied site, thus increasing the periodicity of the overlayer. Attractive interactions allow the molecules to cluster into islands of ordered structure even at very low

surface coverages if the temperature is sufficiently low. Increasing the temperature causes the ordered superstructure to disorder, resulting in a disappearance of the LEED pattern. This is a physical realization of the two-dimensional order-disorder transition that has been employed widely in theoretical studies of phase transitions **(15)**. The techniques and results of these studies therefore are directly applicable to an analysis of the ordered overlayers that form as a result of lateral interactions at surfaces **(16,17)**. LEED studies of order-disorder phenomena in overlayers have been carried out for a limited number of chemisorbed systems. Among the most thoroughly studied systems have been oxygen adatoms on W(110) **(18-26)**, hydrogen adatoms on Ni(111) **(27-30)** and oxygen adatoms on Ni(111) **(31-34)**.

An additional effect of lateral interactions, island formation, is accessible to study by LEED. Results from the adsorption of oxygen on W(110) **(24,25,35)** have shown that the oxygen adatoms cluster into many small islands, rather than forming one large island as would be expected from energetic considerations alone. It is reasonable to assume that the formation of small islands arises as the result of limitations on the diffusion of atoms or molecules across the surface. For the case of oxygen atoms on W(110), it appears that steps on the surface may act as barriers to diffusion, isolating the adatoms on distinct terraces. In other systems, it is possible that islands form as a result of a limited mobility of the adspecies. In either case, the mechanism of island formation will determine the distribution of sizes of islands at any given coverage. Therefore, quantitative studies of the size of ordered islands can provide information on the limitations of diffusion of molecules across the surface. Furthermore, it is well known **(36-38)** that finite size effects can influence strongly the nature of phase

transitions. Detailed information concerning the dimensions of ordered structures on the surfaces thus may be crucial to a thorough understanding of order-disorder phenomena in chemisorbed overlayers.

In the following, we will discuss the results of a LEED investigation of the island formation and order-disorder behavior of CO on Ru(001). It is known that CO adsorbs molecularly in the on-top site on Ru(001) **(10,40)**. At fractional coverages up to $\vartheta = 1/3$ (one CO per three surface Ru atoms, or 5.26 x 10^{14} CO/cm^2), the adsorbed molecules order into a $(\sqrt{3} \times \sqrt{3})R30°$ superstructure (hereafter referred to as the $\sqrt{3}$ structure) **(40-42)**. The formation of the $\sqrt{3}$ structure, in which nearest neighbor sites are unoccupied, indicates a repulsive first neighbor interaction. Results of thermal desorption **(43)** and infrared spectroscopic **(10)** measurements on this system indicate that there is an attractive second neighbor interaction between CO molecules which gives rise to island formation at low temperatures. The $\sqrt{3}$ structure with first and second neighbor interactions, J_1 and J_2, is shown in Fig. 1. The experimental techniques used to study this system with LEED are described in the following section. In Section 3, we present experimental data concerning island size, and change in island size with temperature. A detailed analysis of the data and the corresponding discussion are presented in Section 4. Section 5 contains a summary of our major conclusions.

2. Experimental Methods

The experiments were carried out in an ion-pumped stainless steel ultrahigh vacuum system equipped also with liquid nitrogen cooled titanium sublimation pumping. The base pressure, following bakeout, was below 1 x 10^{-10} Torr. The system contains a quadrupole mass spectrometer and a single pass cylindrical mirror Auger electron spectrometer as well as four grid

LEED optics and a movable Faraday cup for beam intensity measurements. The Faraday cup contains an einzel lens which is negatively biased to accept only those electrons of energy within about 0.5 eV of the energy of the incident beam. It also has been modified by replacement of the original collector cup by a channel electron multiplier **(44,45)**. A 0.13 mm diameter aperture on the Faraday cup was used in these experiments.

The Ru surface was oriented, cut and polished to within 1° of the (001) plane using standard methods. The polished crystal was spotwelded to two parallel 0.025 cm diameter Ta heating wires which were clamped in a Cu holder which was part of a rotary manipulator assembly. Thermocouple leads of 5% Re/95% W and 26% Re/74% W were spotwelded together and then spotwelded to a small piece of Ta foil (approximately 1 mm^2 surface area) on the surface to make the junction. The crystal could be cooled to 100 K using liquid nitrogen refrigeration, and it could be heated resistively to above 1600 K. The thermocouple calibration of Sandstrom and Withrow **(46)** was used below 273 K. Cleaning procedures established previously **(42)** were used to keep the surface free of contaminants.

LEED beam profiles were measured by positioning the Faraday cup on the center of the profile and varying the energy of the electron beam to sweep the profile across the cup aperture **(47)**. Profiles measured in this way were corrected for the intensity variation of the beam with energy by division by the I-V curve. It was assumed in making this correction that there was no variation in beam width over the energy range of the beam profile. The energy width (FWHM) of the substrate beams ranged from approximately 1.5 eV at 37 eV to 3.4 eV at 95 eV. The FWHM of the $(\sqrt{3} \times \sqrt{3})R30°$ overlayer beams ranged from 1.5 eV for the most narrow beam measured to 2.7 eV for the widest. Transformation of the beam profiles as functions of energy to

functions of wave vector was done using

$$\frac{\partial k}{\partial E}|_{\vartheta} = \frac{1}{2}\frac{\sin\vartheta}{\sqrt{150.4}} E^{-\frac{1}{2}} \qquad (1)$$

where ϑ is the angle of the diffracted beam with respect to the surface normal, E is the electron energy in eV and k is the parallel component of the wave vector in Å^{-1} **(47)**. The bulk value of 2.7058 Å was used for the nearest neighbor Ru-Ru distance on the surface in calculating the values of k at the center of the diffracted beam profiles**(48)**.

The overlayers of CO were prepared by adsorption at 350 K followed by cooling to either 100 K or 310 K. This procedure was followed since it has been shown that direct adsorption at low temperature leads to a large density of defects (domain boundaries) in the overlayer at ϑ = 1/3 **(49)**. To calibrate the coverage, the LEED intensity due to the $\sqrt{3}$ structure was measured as a function of exposure to CO at 330 K. The exposure at which a maximum in intensity occurs represents optimum ordering of the $\sqrt{3}$ structure and thus a coverage of ϑ = 1/3. The known constancy of the probability of adsorption of CO at room temperature up to ϑ = 1/3 **(41,50,51)** was then used to relate lower coverages to exposure.

Measurements of the $\sqrt{3}$ beam profiles were carried out at an incident energy of 28 eV. One set of measurements was duplicated at an energy of 49 eV to confirm that multiple scattering effects did not change the measured width **(52)**. Incident beam fluxes of 1-10 nA/mm^2 were used to minimize electron stimulated desorption or dissociation of the CO **(53)**. Variation of intensity of the $\sqrt{3}$ beam with temperature was measured by monitoring the intensity of the beam while cooling from 400 K (desorption of CO begins above 400 K). Ordering and disordering of the overlayer with temperature

was completely reversible: the intensity and width of the beam profile at 100 K remained unchanged following multiple heating and cooling cycles. The widths of the beam profiles are quite sensitive to the presence of oxygen on the surface. Even small amounts of oxygen contaminant cause substantial beam broadening. Care therefore was taken to keep the surface rigorously free of oxygen by techniques established previously **(42)**.

3. Experimental Results

Three distinct sets of experiments were performed in this study of the adsorption of CO on Ru(001). First, profiles of the first-order LEED beams of the Ru(001) surface were measured as a function of electron energy to determine the instrument response function and the step density of the surface. Then, beam profiles for the $\sqrt{3}$ structure of the CO overlayer were measured for a variety of coverages at 100 K and 310 K. Finally, the disordering of the $\sqrt{3}$ structure at temperatures up to 400 K was studied at three coverages by monitoring the LEED intensity as a function of temperature. Each of these sets of experiments is described below.

A. Instrument Response and Step Density

The parameters determining the instrument response function are the energy spread of the electron beam, ΔE, the diameter of the Faraday cup aperture, d, the effective width of the electron beam, D, and the angular spread (source extension) of the beam, γ **(47,54)**. For this instrument, ΔE was determined to be 1.2 eV, using the einzel lens in the Faraday cup as a retarding field energy analyzer. The cup aperture is 0.13 mm, and the true beam width is approximately 1 mm, as estimated by moving the crystal across the beam. However, this width may be modified to a different effective

width by a focusing action of the einzel lens. The source extension was not determined independently, but values of approximately 0.01 radian have been found for other instruments **(47,54)**.

To determine the values of D and γ, and to measure the step density, the width of the first-order substrate beams was measured at energies between 35 and 90 eV. For a surface with a distribution of terraces of different sizes separated by steps, the beam profiles will become broader and narrower with changing energy **(54-57)**. The smallest measured width corresponds to the instrumental width **(54)**. Henzler **(55)** has derived a relationship for the energies at which broadening and narrowing should be observed for the (001) surface of an hcp lattice with steps of height equal to the lattice constant along the hexagonal axis (4.28 Å for Ru). These energies are indicated by arrows in Fig. 2 along with the experimentally determined values of the beam width. It is clear that the measured values are consistent with a model of the surface containing a distribution of steps of height 4.28 Å.

The degree of broadening of the beam profile is determined by the average distance between steps. The relative reduced width (the deconvoluted FWHM divided by the value of k for the beam) of the broadened beams shown in Fig. 2 is 1.0± 0.3 %. Depending on the model used for the distribution of terrace sizes, this indicates either terraces of width 100 lattice spacings (270 Å) **(57)** or of width 50 lattice spacings (135 Å) **(58)**.

The minima in the measured widths in Fig. 2 represent the width of the instrument response function. Using the known values of ΔE and d, these minima were used to determine the values of D and γ. The optimized values for these parameters were found to be D = 0.05 mm and γ = 0.006 radian. The small value of the effective width indicates that the einzel lens in the

Faraday cup acts to discriminate against electrons not moving orthogonally to the detector. A collecting lens used by Park and co-workers **(47)** also reduced the effective beam diameter by essentially increasing the distance between the sample and the collector. For this instrument, the instrumental resolution is limited by the energy spread, ΔE, at low electron energies and by the source extension, γ, at higher energies.

Because the $\sqrt{3}$ beam occurs at a smaller angle than the substrate beam for the same electron energy, the width of the instrument response is narrower for the $\sqrt{3}$ beam. Using the experimentally determined values for ΔE, d, D and γ, the width of the instrument response for the $\sqrt{3}$ beam is 0.0060 Å^{-1} at 28 eV and 0.0057 Å^{-1} at 49 eV. An uncertainty of $\pm$ 0.0006 Å^{-1} is assigned to these values by comparison with the uncertainties in the widths of the substrate beam profiles.

B. Beam Profiles of the CO Overlayer

Beam profiles of the $\sqrt{3}$ structure formed by CO were measured at 100 K and 310 K for a range of coverages as described in Section 2. Profiles measured at 100 K for coverages of $\vartheta = 1/3$ and $\vartheta = 0.10$ are shown in Fig. 3. At $\vartheta = 1/3$, the FWHM of the beam profile is 0.064 Å^{-1}, only slightly broader than the instrument response function. At $\vartheta = 0.10$, the FWHM is 0.0132 Å^{-1}. This increased width indicates that the CO molecules are present in ordered regions of limited extent called islands.

The measured profiles were corrected for the broadening due to the instrument response by a Fourier transform deconvolution. Since the measured profile, $I_m(k)$, is the convolution product of the instrument response function, T(k), and the true beam profile, $I_t(k)$ **(47)**, the true profile can be

recovered from the measured profile using the equation

$$I_t(k) = F^{-1}\left\{\frac{F[I_m(k)]}{F[T(k)]}\right\} \qquad (2)$$

where F and F^{-1} are the forward and reverse Fourier transforms, respectively. The average of two $\sqrt{3}$ beam profiles that had the correct FWHM (0.006 Å^{-1}) was used for the instrument response function, T(k). The measured beam profiles were symmetrized by averaging about their center prior to deconvolution. The application of Eq. (2) was quite sensitive to truncation of the profiles and to noise. Therefore, profiles were smoothed and their wings extended prior to taking the Fourier transforms.

The widths of profiles measured at 100 K for coverages from $\vartheta = 0.10$ to $\vartheta = 1/3$ are shown in Fig. 4 before and after deconvolution. The width increases steadily as the coverage decreases. This shows that, as might be expected, smaller islands form at lower coverages. Values of the widths shown in Fig. 4 as well as widths measured at 310 K are listed in Table 1. The standard deviation in the widths of the deconvoluted profiles was calculated using the error propagation equation appropriate for the deconvolution of two Gaussians.

At $\vartheta = 1/3$, the optimum coverage for the $\sqrt{3}$ structure, there is no difference between the FWHM at 100 K and that at 310 K. For lower coverages, $\vartheta = 1/6$ and $\vartheta = 0.14$, the FWHM increases with the temperature. This indicates a decrease in island size which must be due to loss of CO molecules from the islands. For $\vartheta = 0.12$, the beam profile is so weak and broad at 310 K as to be unmeasurable. At lower coverages still, no intensity due to the $\sqrt{3}$ structure can be seen at all. The good agreement between the deconvoluted widths of the profiles measured at 28 eV and 49 eV indicates that the use of

the kinematic (single scattering) approximation is adequate for the present analysis.

C. Temperature Dependence of the CO Overlayer

Changes in the CO overlayer with temperature were first monitored by measuring the temperature dependence of the intensity of the beam profile at its center. The results for three different coverages are shown in Fig. 5. At $\vartheta = 1/3$, there is only about a 20% decrease in intensity between 100 K and 400 K. At $\vartheta = 1/6$ and $\vartheta = 0.14$, however, there is a dramatic decrease in intensity with increasing temperature.

Some decrease in intensity with temperature is expected due to the displacement of the CO molecules from their optimum positions on the surface as a result of vibrational motion. The expected intensity variation is **(59)**

$$I = I_o e^{-2W} \quad , \tag{3}$$

where

$$2W = (2\pi)^2 \sum_q |\Delta s \cdot u_q|^2 \quad , \tag{4}$$

Δs is the change in the electron beam wave vector, and u_q is the displacement in the q direction. The vibrational frequencies of CO are 2021 cm^{-1} for the carbon-oxygen stretch **(10)**, 445 cm^{-1} for the metal-carbon stretch **(39)**, in the range of 400 cm^{-1} to 600 cm^{-1} for the frustrated rotational motion **(60-61)**, and between 34 cm^{-1} and 126 cm^{-1} for the frustrated translational motion parallel to the surface **(60-62)**. Of these, only the frustrated translational modes are sufficiently low in frequency to cause a measurable change in the mean displacement of CO between 100 K and 400 K. Hosemann and Bagchi **(59)** have derived the mean square displacement with temperature of a three-dimensional harmonic oscillator. A similar derivation for a two-

dimensional harmonic oscillator gives

$$|u_{||}|^2 = \frac{h}{8\pi^2 \nu m}\left\{\frac{1}{2} + \frac{1}{e^{h\nu/kT}-1}\right\} \qquad (5)$$

where $u_{||}$ is the displacement parallel to the surface, ν is the vibrational frequency and m is the mass of the CO molecule, which has been treated as a single particle. Equations (4) and (5) were used to calculate the intensity variation with temperature for a range of values of ν. The most satisfactory fit to the experimental data was obtained for ν = 45 cm^{-1}. The calculated intensity variation is shown by the solid curve in Fig. 5. Up to approximately 220 K, the observed decrease in intensity at ϑ = 1/3 can be attributed to vibrational motion. Above that temperature, an additional type of disorder must occur. Site disorder, in which CO molecules occupy "incorrect" sites in the lattice with respect to the $\sqrt{3}$ structure, is the obvious example. It seems likely that site disorder at ϑ = 1/3 will begin at domain boundaries, only becoming prevalent throughout the overlayer at high temperature.

From measurements at 310 K, it is known that the beam profiles at ϑ = 1/6 and ϑ = 0.14 broaden with increasing temperature. To monitor this change in shape, the intensity at different points on the profile was measured as a function of temperature. As a profile broadens, the intensity in the wings of the profile will decrease less rapidly than the intensity at the center. This behavior is illustrated for ϑ = 0.14 in Fig. 6. Three intensity-temperature curves are plotted together: one was measured at the center of the profile, and the other two at quarter-maximum intensity. Each curve was normalized independently. The slower decrease in intensity at the quarter-maximum points, which indicates broadening, is apparent. The ratio of the intensity at quarter-maximum to that at the center, hereafter referred to as the width ratio, shows the broadening with temperature even

more clearly. The onset of an increase in the width ratio is abrupt, occurring at a temperature of 195 ± 5 K. The same type of behavior is observed at ϑ = 1/6, with the onset of broadening at 240 ± 10 K. The temperatures at which the width ratio begins to change are indicated with arrows in Fig. 4. At ϑ = 1/3, the width ratio is constant up to 400 K. This confirms the previous observation that the FWHM of the beam at ϑ = 1/3 is the same at 100 K and 310 K.

The abrupt onset of beam broadening, which occurs after the intensity has decreased by approximately 20%, is somewhat surprising. Intuitively, one would expect the profile to begin to broaden gradually as the intensity decreases, as has been observed for oxygen adatoms on W(110) **(24)**. An explanation of this behavior is presented in Section 4B.

4. Analysis and Discussion

An analysis of the results presented in the preceding section is divided into two categories that initially appear to be distinct. The first category is the analysis of the widths of the beam profiles to determine the size, and possibly the mechanism of formation of the islands. The second category is the analysis of the ordering and disordering of the islands with temperature to determine the CO-CO lateral interaction energies and to compare with theoretical phase diagrams. However, during the analysis, it will become apparent that the island size distribution and the order-disorder behavior are strongly related. In the following subsection, we shall describe first the analysis of the island size distributions insofar as it can be carried out without reference to the order-disorder behavior. In the second subsection, the order-disorder behavior and its relationship to the island size distribution are discussed. Finally, the results are compared with theoretical phase

diagrams for the $\sqrt{3}$ structure in the third subsection.

A. Island Sizes

In principle, the mechanism of formation of the islands determines the distribution of island sizes **(63)**. There are two possible reasons for the formation of small islands. The first is step-limitation of adatom diffusion **(35)**. If steps act as a barrier to diffusion, then adatoms will be trapped on the terrace on which they initially are adsorbed. The size distribution of the islands thus will be determined by the size distribution of the terraces. Except at extremely low coverages, this model requires that there be a constant number of islands which vary in size directly with coverage. A second possible reason for the formation of small islands is a limited adatom diffusion distance. In this model, adatoms which initially are adsorbed near one another merge to form small islands. Once formed, the configuration with many small islands may represent a local minimum in the free energy, with an activation barrier to the formation of a single large island.

In practice, only for the step-limited model of island formation have size distributions been predicted **(35,57)**. The experimental beam widths were analyzed using these distributions as well as three semi-empirical size distributions. The relation **(64)**

$$I(k) = N \sum_{M} P(M) I_M(k) \quad , \tag{6}$$

where N is the number of islands, P(M) is the probability of occurrence of an island containing M molecules, and $I_M(k)$ is the beam profile due to a single island with M molecules, was used to calculate beam profiles for comparison with experiment given a distribution of sizes, P(M). A set of 34 $I_M(k)$ was calculated for values of M ranging from 59 to 4955, with the molecules arranged

in round islands. The 34 island sizes were chosen to represent constant increments in the value of the diameter of the islands. Thus, the increments in M are smaller at smaller values of M where the width of the beam profile varies more rapidly with island size. The summation in Eq. (6) was carried out over this set of values of M, with P(M) replaced by P(M)ΔM. The results of the analysis for each of the five size distributions is described below.

(1) Geometrical Distributions

Lu and co-workers **(35,58)** have developed a geometrical distribution for terrace widths, Γ,

$$P(\Gamma) \sim (1-\gamma)^{\Gamma-1}\gamma \tag{7}$$

where γ is the probability of encountering a step between two surface atoms in a given direction, and Γ is the width of the terrace in the number of surface atoms. An analysis of the step distribution for the surface used in this study indicates that the mean terrace width is 50 Ru atoms (Section 3A). This corresponds to a value of $\gamma = 0.02$. If the islands are step-limited, the size of an island will be determined by the overall coverage and the size of the terrace on which it resides by

$$M = \vartheta\Gamma^2 \tag{8}$$

where M is the number of molecules in the island, and where it has been assumed that on the average, terraces will have uniform widths in two dimensions. Using this model, the calculated FWHM of the beam profile varies only slightly (from 0.0040 Å^{-1} to 0.0042 Å^{-1} between $\vartheta = 1/6$ and $\vartheta = 0.10$. It is apparent that using a constant average terrace width, this model cannot predict the rapid change in FWHM with coverage at intermediate coverages that is observed experimentally. Only if the mean terrace width is

allowed to vary substantially with coverage can the experimental values be reproduced. Curve (a) in Fig. 7 shows the island size distribution (with γ = 0.022) that gives the correct FWHM for $\vartheta = 1/6$ at 100 K.

(2) Henzler's Distribution

Henzler **(57)** has proposed a distribution for the terrace width distribution given by

$$\Gamma P(\Gamma) \propto \Gamma \exp\left\{-\left(\frac{\Gamma}{w}\right)^E - \left(\frac{w}{\Gamma}\right)^E\right\} \qquad (9)$$

where $E \simeq 0.8$ and w is an adjustable parameter determining the mean terrace width. Based on this distribution, the mean terrace width on the Ru surface was found to be 100 Ru atoms, as discussed in Section 3A. A value of w = 40 in Eq. (9) gives this mean terrace width. Eq. (8) again was used to relate M to Γ, so that Eq. (9) could be used to predict island size distributions. As with the geometrical distribution, the requirement of islands limited by terrace size results in a very slow variation of FWHM with coverage between $\vartheta = 1/6$ and $\vartheta = 0.10$. (The range of the value of the FWHM was 0.0036 $\mathring{A}^{-1}$ at $\vartheta = 1/6$ to 0.0037 $\mathring{A}^{-1}$ at $\vartheta = 0.10$.) A fit to the experimental data requires a different mean terrace width at each coverage. The distribution that corresponds to the correct beam profile width at $\vartheta = 1/6$ (w = 17 and mean terrace width = 41 Ru atoms) is shown by curve (b) in Fig. 7.

(3) Ball-In-Urn Distribution

If there is a fixed number of nucleation sites, N, for islands, then an island size distribution can be determined from the number of ways of distributing n adsorbates among those sites. The result is **(64)**

$$P(M) \propto \frac{\Omega'(N,n,M)}{N\Omega(N,n)} \qquad (10)$$

where

$$\Omega(N,n) = \frac{(N-1+n)!}{(N-1)!n!}$$

and

$$\Omega'(N,n,M) = N\frac{(N-2+n-M)!}{(N-2)!(n-M)!} \quad .$$

A different number of nucleation sites had to be used for each coverage to fit the experimental data with this distribution. This is consistent with the results of the prior two analyses, that the experimental values are incompatible with a model that requires a fixed number of islands at all coverages. Curve (d) in Fig. 7 shows the ball-in-urn distribution (N = 2100 and n = 2,666,667 for a 4000 x 4000 Ru atom surface) which gives the value of the FWHM measured for ϑ = 1/6 at 100 K.

(4) Distance Distribution

A computer simulation based on a very simple model of diffusion-limited island nucleation was used to generate probability distributions for the nearest neighbor distance between island centers, r, that are Gaussian in r **(64)**. The width of the distributions increases approximately linearly with the mean distance r_o. Assuming that the number of molecules in an island is related to the distance to its nearest neighbor by $M = \vartheta r^2$, distributions of island sizes were generated using this model. A decreasing value of r_o with decreasing coverage was required to fit the measured values of the FWHM. This rather unphysical result indicates that the model used to generate this distribution is too simple to describe the overlayer correctly. Curve (e) in

Fig. 7 represents the distance distribution (r_o = 106 Ru atoms) for ϑ = 1/6 at 100 K.

(5) Delta Function Distribution

For comparison with the other distributions, a distribution in which there is only one island size was also considered. The delta function distribution for ϑ = 1/6 is shown by curve (f) of Fig. 7.

Figure 7 amply demonstrates that knowledge of the width of a beam profile only is insufficient to determine the island sizes. In addition, use of the delta function distribution to analyze the size does not give the mean size in any sense, but at best an upper limit to the mean size as discussed elsewhere **(64)**. Knowledge of the coverage dependence of the beam width can be used to test specific models for the size distribution. In this case, models that require a fixed number of islands fail to fit the experimental data because they cannot generate the rapid change in full-width with coverage that is observed. This indicates that both a step-limited model and a defect-nucleation model are not correct for this system. The distance-distribution also seems to be incorrect since it requires larger diffusion distances at larger coverages. However, this distribution is the result of a rather crude simulation and hence cannot be used to rule out a diffusion-limited model for island formation.

B. Disordering and Island Size

As shown in Figs. 5 and 6, no change in the width of the low coverage beam profiles with increasing temperature is observed until the intensity has decreased by approximately 20%. This seems a somewhat surprising result. The I-T behavior at ϑ = 1/3 indicates that there is no site disorder within the

$\sqrt{3}$ structure below approximately 220 K. Thus the loss of intensity must be due to loss of CO molecules from the islands. But as CO molecules leave the islands, the islands become smaller and the FWHM larger. Therefore, it might be expected that changes in intensity and FWHM would occur simultaneously. This has in fact been observed for oxygen adatoms on W(110) **(24)**. However, it is possible that the size distribution of the islands could modify this simple prediction. Since the height of a beam profile is proportional to the square of the number of molecules in the island, large islands overwhelmingly dominate in determining the overall profile [Eq. (6)]. On the other hand, the FWHM is inversely proportional to the diameter of the island, so that the FWHM changes very rapidly with size for small islands and more slowly for large islands. Using these considerations, it can be seen that if small islands totally dissolve it will tend to decrease the FWHM. If at the same time large islands lose some fraction of their molecules, the intensity will decrease, and the FWHM will increase slightly. For the correct distribution of island sizes, it is possible that the two influences on the FWHM will cancel until the intensity has dropped appreciably. To test this hypothesis, a simple model of the disordering process was considered for step-limited and nonstep-limited models of island formation.

The disordered phase of CO was treated as a two-dimensional ideal gas, and the $\sqrt{3}$ structure as a 2-d solid. The chemical potentials of the two phases were calculated and equated to determine the number density of disordered CO molecules as a function of temperature. The partition function for the 2-d gas is

$$Q_g = \frac{1}{N_g!}\left[\frac{2\pi mkT}{h^2}A_g\right]^{N_g} q_{int}^{N_g} \qquad (11)$$

where N_g is the number of 2-d gas molecules, m is the mass, A_g is the surface

area available to the molecules (total area minus the area covered by islands), and q_{int} is the internal partition function of a single molecule. In the 2-d solid, it is assumed that all the molecules are ordered in the $\sqrt{3}$ structure, i.e. there is no occupancy of nearest neighbor sites. If the vibrational modes of the CO remain independent in the 2-d solid (the CO-CO distance is 4.7 Å), the partition function for an island for which the edge molecules are a negligible fraction of the total is

$$Q_s = e^{\frac{-6N_sJ_2}{2kT}} q_{int}^{N_s} \tag{12}$$

where N_s is the number of molecules in the 2-d solid, and J_2 is the interaction energy for CO molecules in second nearest neighbor sites. In both Eqs. (11) and (12), the zero of energy has been taken as the minimum of the potential energy well for binding of a CO molecule to the surface. Equating the chemical potential for the solid and gas gives

$$\vartheta_g = \frac{N_g}{A_g} = \left(\frac{2\pi mkT}{h^2}\right)\left(\frac{q_{int,g}}{q_{int,s}}\right) e^{\frac{6J_2}{2kT}} \tag{13}$$

The internal partition functions for molecules in the gas and solid were taken to be the same, except for a minor difference due to the different carbon-oxygen stretching frequencies **(10)**.

For a finite size island the energy will be less than $6J_2N_s/2$ since the molecules at the edge of the island have a coordination less than six. The number of molecules at the edge of the island will be proportional to the square root of the number in the island, so that the total energy is

$$E = \frac{6J_2N_s}{2} - cJ_2\sqrt{N_s} \tag{14}$$

where c is a constant taking into account the coordination of the edge molecules and the proportionality of $\sqrt{N_s}$ to the number at the edge. Using

this value of E in the partition function for the solid, the new value for the 2-d gas phase density is

$$\vartheta_g' = \vartheta_g \, e^{\frac{-cJ_2}{\sqrt{N_s}kT}} \quad . \tag{15}$$

In a step-limited model of island formation, each island is located on a terrace, isolated from all other islands. Thus, Eq. (15) can be used directly to calculate the 2-d gas phase density on each terrace as a function of temperature. Once ϑ_g' is known, the change in size of the island follows immediately, and the beam profile can thus be calculated as a function of temperature. In comparison with experiment, the calculated profiles are numerically convoluted with a Gaussian "instrument response function" of width 0.006 Å^{-1}. This calculation was carried out for distributions (a), (c), (d), (e) and (f) in Fig. 7. The calculation was quite successful in duplicating the sudden onset of change in the width ratio. However, for none of the size distributions did the intensity drop by more than 10% before the width ratio began to change. In addition, only a 10 K difference between the intensity curves at $\vartheta = 1/6$ and $\vartheta = 0.014$ was calculated, in contrast to the observed difference of 30 K or more (Fig. 4).

If the islands are not step-limited, then all the islands in the overlayer should be considered in calculating the partition function for the 2-d solid. A direct approach to this problem was not attempted. Instead, an approximate method was used. The overall 2-d gas density was calculated using Eq. (13). It was then assumed that all islands lose CO molecules from their edges at the same rate, with a correction term for the higher energy of smaller islands as in Eq. (15), until the correct overall 2-d gas density was reached. Inclusion of the energy correction term causes small islands to lose molecules from their edges at a greater rate than large islands. Omission of

this term causes a distribution to act like a distribution with a slightly larger mean island size. Beam profiles were calculated as for the step-limited model. It was found that for different distributions of island sizes the onset of change of the width ratio was shifted to higher temperatures as the mean island size became smaller. This is in agreement with our qualitative argument concerning the relative effects of a loss of CO molecules from small and large islands in the FWHM. For the ball-in-urn distribution, the intensity decreased by 10% before beam broadening was observed. For the geometrical distribution, the profile actually became more narrow with increasing temperature as the large number of small islands in that distribution preferentially disordered. Therefore, a distribution intermediate in shape between these two was sought. An empirical distribution of the form

$$P(M) \propto (1-b)^{M^{3/4}} \qquad (16)$$

where b is an arbitrary constant, was found to give the correct relative behavior of intensity and width with temperature. The distribution used at ϑ = 1/6 is shown in curve (c) of Fig. 7. The calculated intensity and width ratio for J_2 = -1.28 kcal/mole is compared with the experimental data in Fig. 8. The calculation reproduces the delayed onset of broadening quite successfully, although the shape of the calculated intensity curve is not correct. Also, the more rapid increase in width with temperature at ϑ = 0.14 than at ϑ = 1/6 is predicted by the calculation. However, as for the step-limited model, the observed difference in temperature between the two intensity curves is not reproduced. The best fit to both sets of data (ϑ = 1/6 and ϑ = 0.14) therefore occurs with J = -1.20 kcal/mole which places the calculated curves for ϑ = 1/6 approximately 10 K too low and those for ϑ = 0.14 approximately 10 K too high in temperature.

Three major approximations were made in deriving the partition functions for the 2-d gas and 2-d solid [Eqs. (11) and (12)]. The first two were 1) treating the disordered phase as an ideal gas and 2) equating the internal partition functions of molecules in the two phases. Modification of these two approximations causes the calculated intensity and width ratio curves to change mainly by a shift along the temperature axis. Thus, these two approximations affect the estimate of J_2 most strongly. The third approximation, that site-disorder does not occur within the islands, is best at low temperature. Inspection of the intensity-temperature curve at $\vartheta = 1/3$ (Fig. 6) shows that this is a rather reasonable approximation over the temperature range for which the calculations were performed. The relative behavior of the intensity and the width ratio are not influenced greatly by these approximations. Therefore, conclusions based on calculations of these two quantities can be given a rather high degree of credence.

It was not possible to fit the experimental intensity and width ratio curves using a step-limited model for island growth in which the density of the disorderd phase about an island is due to loss of CO molecules from that island alone. If the number of CO molecules lost from each island is proportional to the number of molecules at the edge of the island (and this is a very reasonable approximation), it is possible to fit the experimental curves only with one model for the island size distribution. It is therefore concluded that the curve of Fig. 7(c) represents the physical distribution of island sizes, although Eq. (16), used to describe it, is only an empirical equation. Therefore, the mean island sizes have been determined by varying the parameter b in Eq. (16) to produce profiles of the widths measured at 100 K. The results are compared with the values calculated using the delta function distribution in Table 2. In making these calculations, it has been assumed that the

width measured at 100 K is the most narrow width that will occur at each coverage. This has been shown to be correct experimentally for $\vartheta = 1/6$ and $\vartheta = 0.14$. Extrapolating the behavior at $\vartheta = 1/6$ and $\vartheta = 0.14$, it appears that the onset of broadening at $\vartheta = 0.12$ is near 100 K, and at $\vartheta = 0.10$, it is probably below 100 K. Therefore, the calculated island sizes are correct for $\vartheta = 1/6$, 0.14 and 0.12, and probably somewhat small for $\vartheta = 0.10$.

Both the coverage dependence of the beam widths and the behavior of intensity and width with temperature show that a step-limited model for island growth is not correct for CO on Ru(001). In addition, analysis of the disordering behavior of the islands has shown that the size distribution must be of the shape of curve (c) in Fig. 7, which can be described by Eq. (16).

C. Comparison with Phase Diagrams

The dissolution of ordered islands into a disordered phase is a first-order transition. In these experiments, the disordering was monitored under conditions of constant 2-d density (coverage). For these conditions, the disordering will take place over a range of temperature, and the transition temperature will be that at which the ordered phase disappears completely. This point is observable by LEED as the temperature at which the integrated intensity in the overlayer beam profile effectively goes to zero **(26)**. Quantitative measurements of these temperatures were not made in this study. However, they can be estimated from the experiments that were performed, in order to make a qualitative comparison with calculated phase diagrams. At $\vartheta = 1/6$ and $\vartheta = 0.14$ for CO on Ru(001), the transition temperatures have been estimated by extrapolating the intensity curves of Fig. 6 to the point of intersection with the background and the width ratio curves to unity. The transition temperatures are, very approximately, 650 K at $\vartheta = 1/6$ and 550 K at $\vartheta =$

0.14. At ϑ = 0.12, there is only a very weak profile observable at 310 K. Therefore an estimate of the transition temperature is approximately 400 K. At ϑ = 0.10, no beam profile is observable at room temperature, so the transition temperature is $\leq$ 300 K. The error bars on these estimates are at least $\pm$ 50 K.

Phase diagrams have been calculated for overlayers on a triangular substrate such as Ru(001), with attractive second and repulsive first nearest neighbor interactions in the ratios $\frac{J_2}{J_1} = -1$ **(65)** and $\frac{J_2}{J_1} = 0$ **(66-69)**. In the case where the second neighbor interaction is zero, no ordered structure forms at any temperature below a coverage of about 0.28 **(66,67)**. Above that coverage, an ordered structure does form and disorders with increasing temperature via a second order phase transition. The maximum transition temperature occurs at ϑ = 1/3 and has a value of $\frac{kT}{J_1} = 0.35$ **(68,69)**. When the attractive second neighbor interaction is added, the transition temperature at ϑ = 1/3 is increased to a value of $\frac{kT}{J_1} = 1.4$ **(65)**. In addition, a coexistence region in which the ordered and disordered phases are in equilbrium is added to the phase diagram. The coverage range over which island formation has been observed for CO on Ru(001) falls within the theoretically predicted coexistence region.

For CO on Ru(001), the magnitude of the second neighbor interaction should be considerably smaller than that of the first. From thermal desorption measurements, a value of $\frac{J_2}{J_1} = -1/4$ has been estimated **(43)**. Therefore a direct comparison of the experimental transition temperatures with the calculated values is not feasible. However, a qualitative comparison reveals an interesting disparity between the theory and experiment. The

experimental values of the transition temperature, although determined only approximately, show a clear trend of rapidly decreasing transition temperature with coverage. The experimental transition temperature appears to drop by a factor of approximately two between $\vartheta = 1/6$ and $\vartheta = 0.10$. In contrast, the theoretical transition temperature drops by only ten percent between the two coverages.

This discrepancy may be the result of the small island sizes of the CO overlayer (see Table 2). Renormalization group calculations have shown that finite size effects can transform a flat phase boundary to one in which the transition temperature increases with coverage **(38)**. While the boundary conditions used in the calculation are almost certainly not the same as those which determine island size in the experimental system, the results indicate that finite size effects have the potential to perturb the phase diagram as observed experimentally.

5. Conclusions

The major conclusions of this work are summarized below.

1. The Ru(001) surface contains steps that are one hcp unit cell (two Ru atoms) in height. The step density on the surface used in these experiments is, depending on the model used for step distributions, either one step every 50 Ru atoms or one step every 100 Ru atoms.

2. The temperature dependence of the fully ordered $(\sqrt{3} \times \sqrt{3})R30°$ CO overlayer indicates that the frequency of the frustrated translational motion of CO parallel to the surface is approximately 45 cm^{-1}.

3. The coverage dependence of the widths of the $\sqrt{3}$ beam profiles is inconsistent with a step limited model of island formation for CO on Ru(001).

4. The distribution of island sizes can have a pronounced effect on the change in the beam width during island dissolution. Using this effect, it was possible to determine the island size distribution for CO on Ru(001) and thus the mean island size as a function of coverage [see Eq. (16) and Table 2].

5. The order-disorder behavior of CO on Ru(001) at low coverages appears to be affected strongly by the finite size of the islands.

Acknowledgments

This research was supported by the Army Research Office under Grant No. DAAG29-79-C-0132. The research reported in this paper made use of the Dreyfus-NSF Theoretical Chemistry Computer which was funded through grants from the Camille and Henry Dreyfus Foundation, the National Science Foundation (Grant No. CHE78-20235), and the Sloan Fund of the California Institute of Technology.

References

1. T. Engel and G. Ertl, J. Chem. Phys. **69**, 1267 (1978).

2. T. B. Grimley and M. Torrini, J. Phys. C **6**, 868 (1973).

3. T. L. Einstein and J. R. Schrieffer, Phys. Rev. B **7**, 3629 (1973).

4. K. H. Lau and W. Kohn, Surface Sci. **65**, 607 (1977).

5. A. M. Stoneham, Solid State Commun. **24**, 425 (1977).

6. T. L. Einstein, Phys. Rev. B **16**, 3411 (1977).

7. K. H. Lau, Solid State Commun. **28**, 757 (1978).

8. V. Hartung, Z. Physik B **32**, 307 (1979).

9. A. M. Brodskii and M. I. Urbakh, Surface Sci. **105**, 196 (1981).

10. H. Pfnur, F. M. Hoffmann, A. Ortega, D. Menzel and A. M. Bradshaw, Surface Sci. **93**, 431 (1980).

11. A. Crossley and D. A. King, Surface Sci. **95**, 131 (1980).

12. D. L. Adams, Surface Sci, **42**, 12 (1974).

13. P. K. Johansson, Chem. Phys. Letters **65**, 366 (1979).

14. E. Bauer, in *Phase Transitions in Surface Films*, Eds. J. G. Dash and J. Ruvalds, Plenum Press, New York, 1980.

15. H. E. Stanley, *Introduction to Phase Transitions and Critical Phenomena*, Oxford University Press, New York, 1971.

16. K. Binder and D. P. Landau, Surface Sci. **61**, 577 (1976).

17. D. P. Landau, in *Monte Carlo Methods in Statistical Physics*, Ed. K. Binder, Springer Verlag, New York, 1979.

18. J. C. Buchholz and M. G. Lagally, Phys. Rev. Letters **35**, 442 (1975).

19. T. Engel, H. Niehus and E. Bauer, Surface Sci. **52**, 237 (1975).

20. G. Ertl and D. Schillinger, J. Chem. Phys. **66**, 2569 (1977).

21. T.-M. Lu, G.-C. Wang and M. G. Lagally, Phys. Rev. Letters **39**, 411 (1977).

22. E. D. Williams, S. L. Cunningham and W. H. Weinberg, J. Chem. Phys. **68**, 4688 (1978).

23. W. Y. Ching, D. L. Huber, M. G. Lagally and G.-C. Wang, Surface Sci. **77**, 550 (1978).

24. G.-C. Wang. T.-M. Lu and M. G. Lagally, J. Chem. Phys. **69**, 479 (1978).

25. T.-M. Lu, G.-C. Wang and M. G. Lagally, Surface Sci. **92**, 133 (1980).

26. M. G. Lagally, T.-M. Lu and G.-C. Wang, in *Ordering in Two Dimensions*, Ed. S. Sinha, Elsevier, Amsterdam, 1980.

27. R. J. Behm, K. Christmann and G. Ertl, Solid State Commun. **25**, 763 (1978).

28. R. C. Kittler and K. H. Bennemann, Solid State Commun. **32**, 403 (1979).

29. K. Christmann, R. J. Behm, G. Ertl, M. A. Van Hove and W. H. Weinberg, J. Chem. Phys. **70**, 4168 (1979).

30. E. Domany, M. Schick and J. S. Walker, Solid State Commun. **30**, 331 (1979).

31. A. R. Kortan, P. I. Cohen and R. L. Park, J. Vacuum Sci. Technol. **16**, 541 (1979).

32. L. D. Roelofs, T. L. Einstein, P. E. Hunter, A. R. Kortan, R. L. Park and R. M. Roberts, J. Vacuum Sci. Technol. **16**, 478 (1979).

33. L. D. Roelofs, A. R. Kortan, T. L. Einstein and R. L. Park, Phys. Rev. Letters **46**, 1465 (1981).

34. A. R. Kortan and R. L. Park, Phys. Rev. B (to be published).

35. T.-M. Lu, G.-C. Wang and M. G. Lagally, Surface Sci. **107**, 494 (1981).

36. M. E. Fisher, in *Proceedings of the Enrico Fermi International School of Physics*, Academic Press, New York, 1971.

37. D. P. Landau, Phys. Rev. B. **13**, 2997 (1976).

38. S. Ostlund and A. N. Berker, Phys. Rev. Letters **42**, 843 (1979).

39. G. E. Thomas and W. H. Weinberg, J. Chem. Phys. **70**, 1437 (1979).

40. J. T. Grant and T. W. Haas, Surface Sci. **21**, 76 (1970).

41. T. E. Madey and D. Menzel, Japan J. Appl. Phys, Suppl. 2, Pt. 2, 229 (1974).

42. E. D. Williams and W. H. Weinberg, Surface Sci. **82**, 93 (1979).

43. H. Pfnur, P. Feulner, H. A. Engelhardt and D. Menzel, Chem. Phys. Letters **59**, 481 (1978).

44. S. P. Weeks, C. D. Ehrlich and E. W. Plummer, Rev. Sci. Instrum. **48**, 190 (1977).

45. S. P. Weeks, private communication.

46. D. R. Sandstrom and S. P. Withrow, J. Vacuum Sci. Technol. **14**, 748 (1977).

47. R. L. Park, J. E. Houston and D. G. Schreiner, Rev. Sci. Instrum. **42**, 60 (1971).

48. International Tables for X-Ray Crystallography, Vol. III, The Kynoch Press, Birmingham, England, 1962.

49. P. Feulner, H. A. Englehardt and D. Menzel, Appl. Phys. **15**, 355 (1978).

50. J. C. Fuggle, T. E. Madey, M. Steinkelberg and D. Menzel, Surface Sci. **52**, 521 (1975).

51. J. A. Schwarz and S. R. Kelemen, Surface Sci. **87**, 510 (1979).

52. W. Moritz, in *Electron Diffraction 1927-77*, Eds. P. J. Dobson, J. B. Pendry and C. J. Humphreys, The Institute of Physics, London, 1977, p. 261.

53. J. C. Fuggle, E. Umbach, P. Feulner and D. Menzel, Surface Sci. **64**, 69 (1977).

54. G.-C. Wang and M. G. Lagally, Surface Sci. **81**, 69 (1979).

55. M. Henzler, Surface Sci. **22**, 12 (1970).

56. M. Henzler, in *Electron Spectroscopy for Surface Analysis*, Ed. H. Ibach, Topics in Current Physics, Vol. 4, Springer-Verlag, Berlin, 1977.

57. M. Henzler, Surface Sci. **73**, 240 (1978).

58. T.-M. Lu, S. R. Anderson, M. G. Lagally and G. C. Wang, J. Vacuum Sci. Technol. **17**, 207 (1980).

59. R. Hosemann and S. N. Bagchi, *Direct Analysis of Diffraction by Matter*, North Holland, Amsterdam, 1962.

60. T. E. Madey, Surface Sci. **79**, 575 (1979).

61. N. V. Richardson and A. M. Bradshaw, Surface Sci. **88**, 255 (1979).

62. C. O. Quicksall and T. G. Spiro, Inorg. Chem. **7**, 2365 (1968).

63. M. G. Lagally, G.-C. Wang and T.-M. Lu, CRC Crit. Rev in Solid State Mat. Sci. **1**, 233 (1978).

64. E. D. Williams and W. H. Weinberg, Surface Sci. **110**, 000 (1981).

65. B. Mihura and D. P. Landau, Phys. Rev. Letters **38**, 977 (1977).

66. L. K. Runnels and L. L. Combs, J. Chem. Phys. **45**, 2482 (1966).

67. D. S. Gaunt, J. Chem. Phys. **46**, 3237 (1967).

68. B. D. Metcalf, Phys. Letters **45A**, 1 (1973).

69. M. Schick, J. S. Walker and M. Wortis, Phys. Letters **58A**, 479 (1976).

Table Captions

Table 1: Widths of beam profiles in $\mathring{A}^{-1}$ for $\sqrt{3}$ structure at different coverages and temperatures. $FWHM_m$ and σ_m are the measured width and standard deviation. $FWHM_t$ and σ_t are the width and standard deviation following deconvolution to correct for the instrument response. Values for $\vartheta = 1/3$ at 100 K and 310 K are combined as they are identical. *Value measured at 49 eV incident energy. All other values measured at 28 eV incident energy.

Table 2: Mean island size and diameter for the correct distribution described in Section 4B and the delta function distribution. b is the value of the parameter used in Eq. (16).

Table 1

T	ϑ	$FWHM_m$	σ_m	$FWHM_t$	σ_t
100 K	1/3	0.0064	0.0005	0.0028	0.0021
	1/6	0.0079	0.0002	0.0041	0.0008
	0.14	0.0088	0.0008	0.0046	0.0012
	0.14*	0.0090	0.0002	0.0049	0.0007
	0.12	0.0103	0.0007	0.0063	0.0010
	0.10	0.0132	0.0007	0.0090	0.0009
310 K	0.20	0.0068	0.0006	0.0030	0.0017
	1/6	0.0089	0.0005	0.0058	0.0009
	0.14	0.0155	0.0015	0.0115	0.0016

Table 2

	Correct Distribution			Delta Function Distribution	
ϑ	b	$\overline{M}$	$\overline{d}$, Å	M	d, Å
1/6	0.008	1020	138	2700	255
0.14	0.014	515	96	1720	218
0.12	0.019	325	77	1100	163
0.10	0.032	160	54	560	115

Figure Captions

Fig. 1: The $(\sqrt{3} \times \sqrt{3})R30°$ structure of CO on Ru(001). Arrows indicate the repulsive first neighbor interaction, J_1, and the attractive second neighbor interaction, J_2.

Fig. : FWHM of the first-order diffraction beams of the clean Ru(001) as a function of energy. Error bars represent the standard deviation determined from repeated measurements. Arrows represent the energies at which maxima (down-arrows) and minima (up-arrows) are expected in the width [Ref. (55)]. The solid curve is the instrumental width. The dashed curve is drawn empirically to show the broadening.

Fig. 3: Averaged beam profiles for the $\sqrt{3}$ structure at absolute coverages $\vartheta = 1/3$ and $\vartheta = 0.10$ measured at 100 K. The profile for $\vartheta = 1/3$ is the average of nine measured profiles, that at $\vartheta = 0.10$ is the average of five. Measurements were made with an incident electron energy of 28 eV. $\Delta k = 0$ is the center of the $\sqrt{3}$ beam profile, at k $= 0.2464\ \text{Å}^{-1}$.

Fig. 4: FWHM of the $\sqrt{3}$ beam profile as a function of coverage, at 100 K. Circles, ○ ,measured widths at incident eletron energy of 28 eV. Triangles, Δ, widths corrected for instrument response by deconvolution. Error bars on FWHM are the standard deviation determined from repeated measurements. Error bars on the coverage are estimated.

Fig. 5: The variation with temperature of the intensity at the center of the $\sqrt{3}$ beam profile for $\vartheta = 1/3$, 1/6 and 0.14. The variation of the background intensity at $\vartheta = 1/6$, x's and at $\vartheta = 0.14$, ○ ,

is also shown. Arrows indicate the temperatures at which the beams begin to broaden. The smooth curve is the calculated decrease in intensity due to frustrated translational motion of the CO parallel to the surface with a frequency of 45 cm^{-1}.

Fig. 6: The variation with temperature of the intensity at three different positions on the beam profile. The position for each curve is illustrated schematically in the inset. Each curve has been normalized independently to unity at 100 K. The ratio of the curves measured in the wings of the profile to the curve measured at the center is also shown for the same points.

Fig. 7: Probability of observing an island containing M molecules as a function of M for (a) geometrical distribution, (b) Henzler's distribution, (c) empirical distribution (described in Section 4B), (d) ball-in-urn distribution, (e) distance distribution, and (f) delta function distribution. Each distribution gives rise to a beam profile of width 0.0041 $\mathring{A}^{-1}$ as observed for $\vartheta = 1/6$ at 100 K.

Fig. 8: Comparison of calculated (solid curves) and experimental (circles) intensity and width ratio as functions of temperature. An arbitrary size distribution (see text) and a value of J_2 = -1.28 kcal/mole were used in the calculation. The calculated intensity has been multiplied by exp(-2W) [see Eq. (4)].

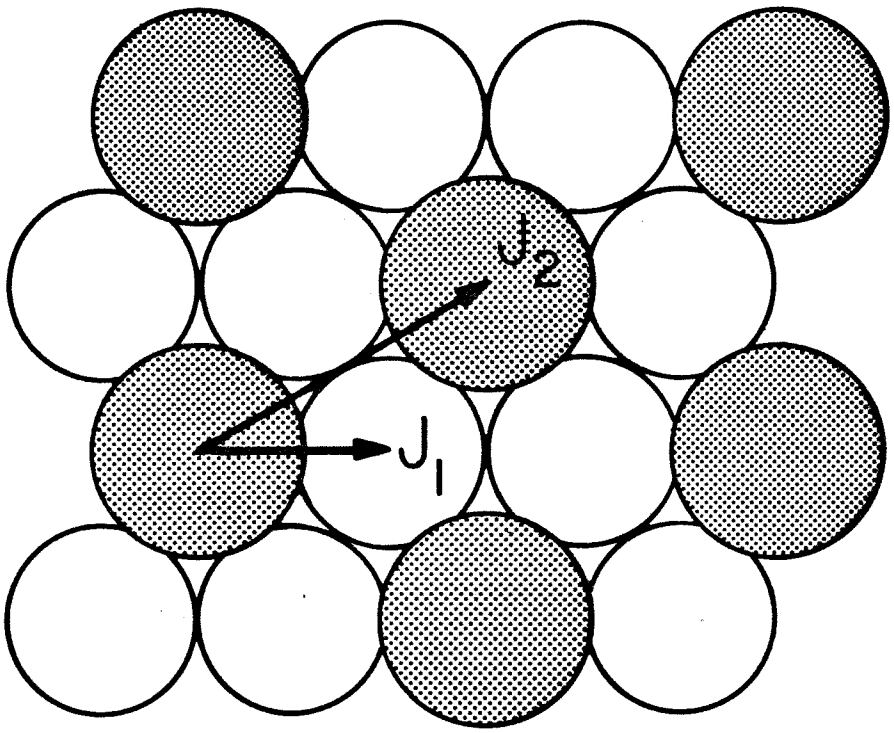

Figure 1

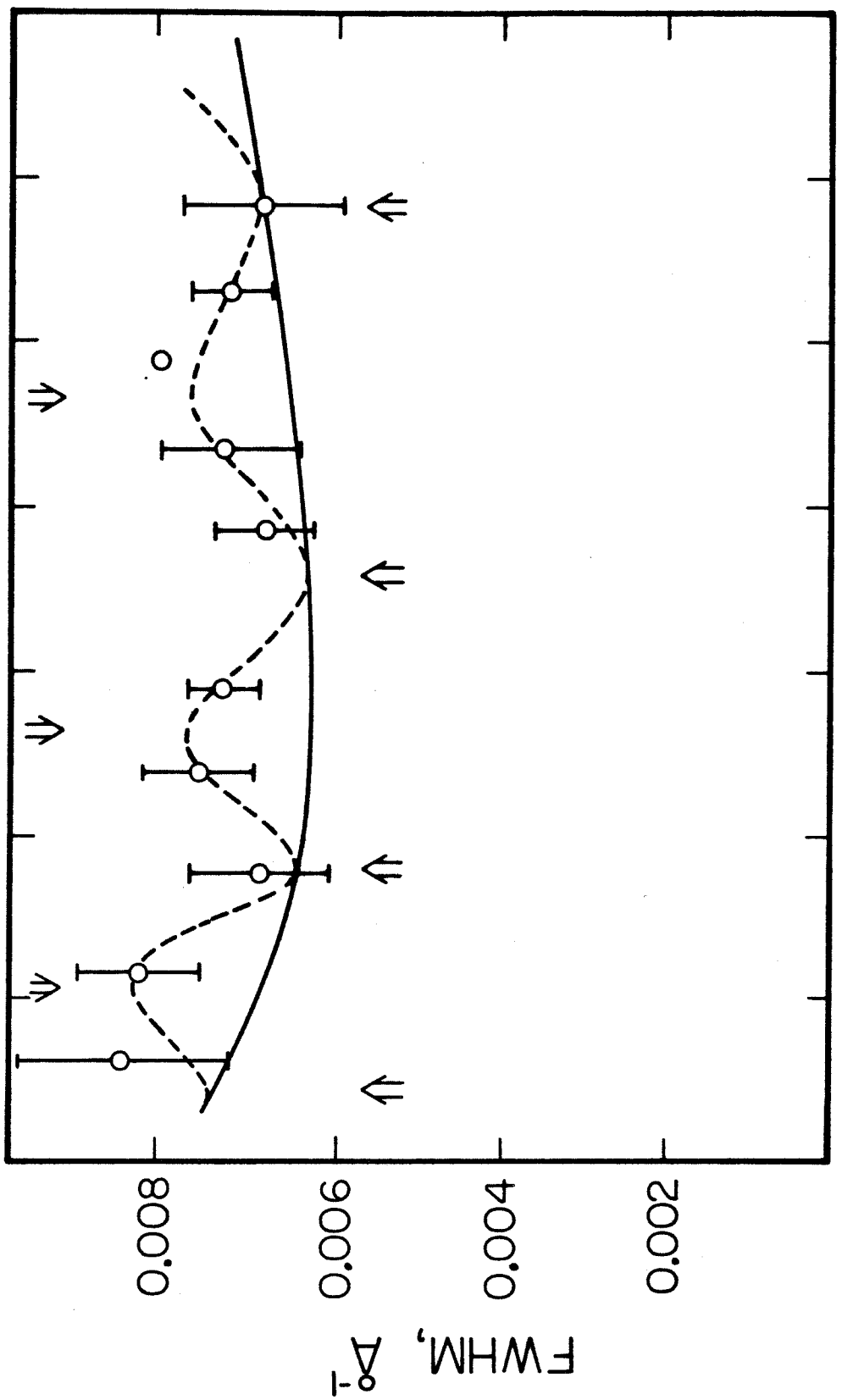
FWHM, Å⁻¹
0.008
0.006
0.004
0.002
40
50
60
70
80
90
Electron Energy, eV

Figure 2

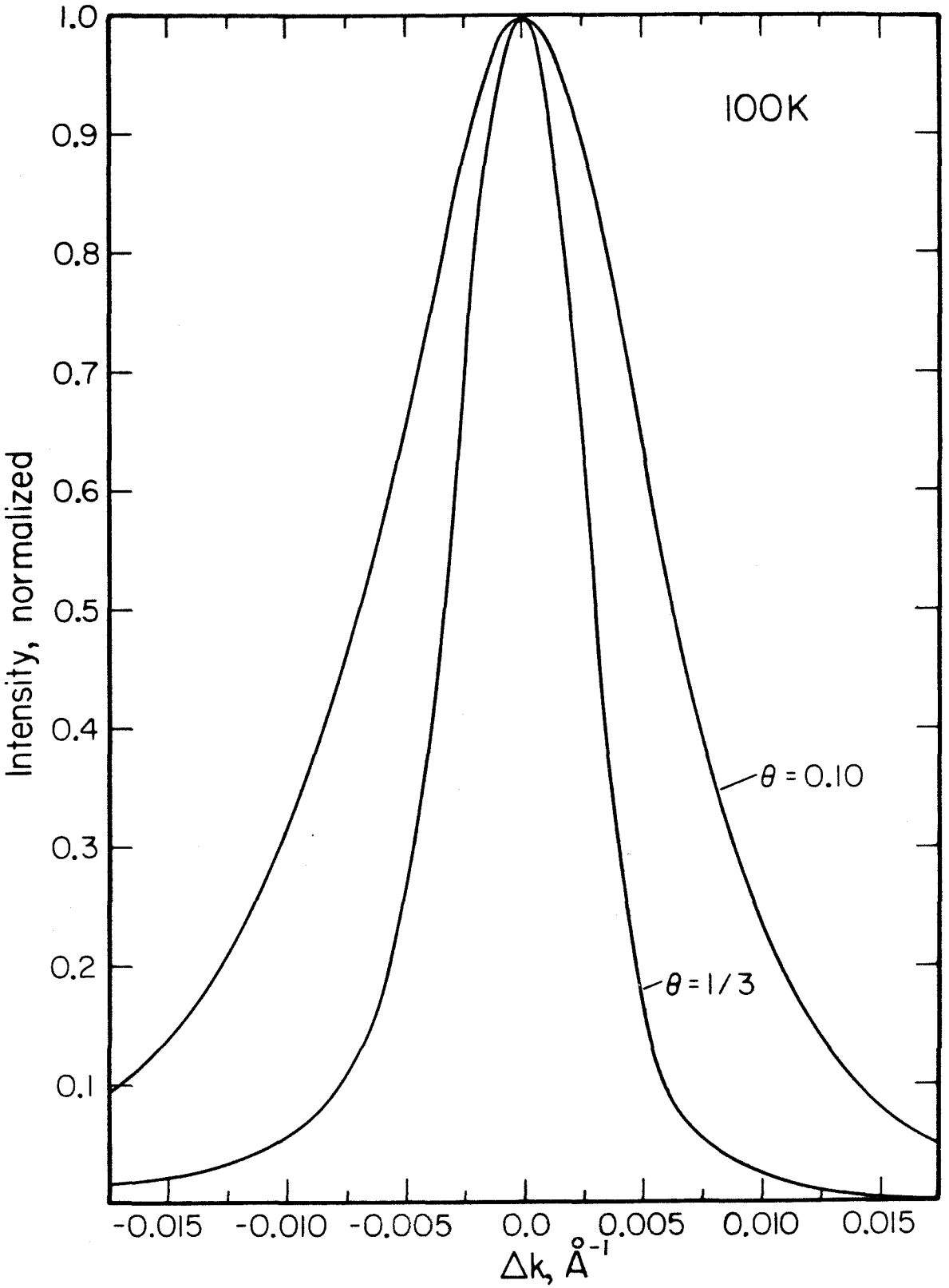
1.0
0.9
0.8
0.7
0.6
0.5
0.4
0.3
0.2
0.1
Intensity, normalized
100K
θ = 0.10
θ = 1/3
-0.015
-0.010
-0.005
0.0
0.005
0.010
0.015
Δk, Å⁻¹

Figure 3

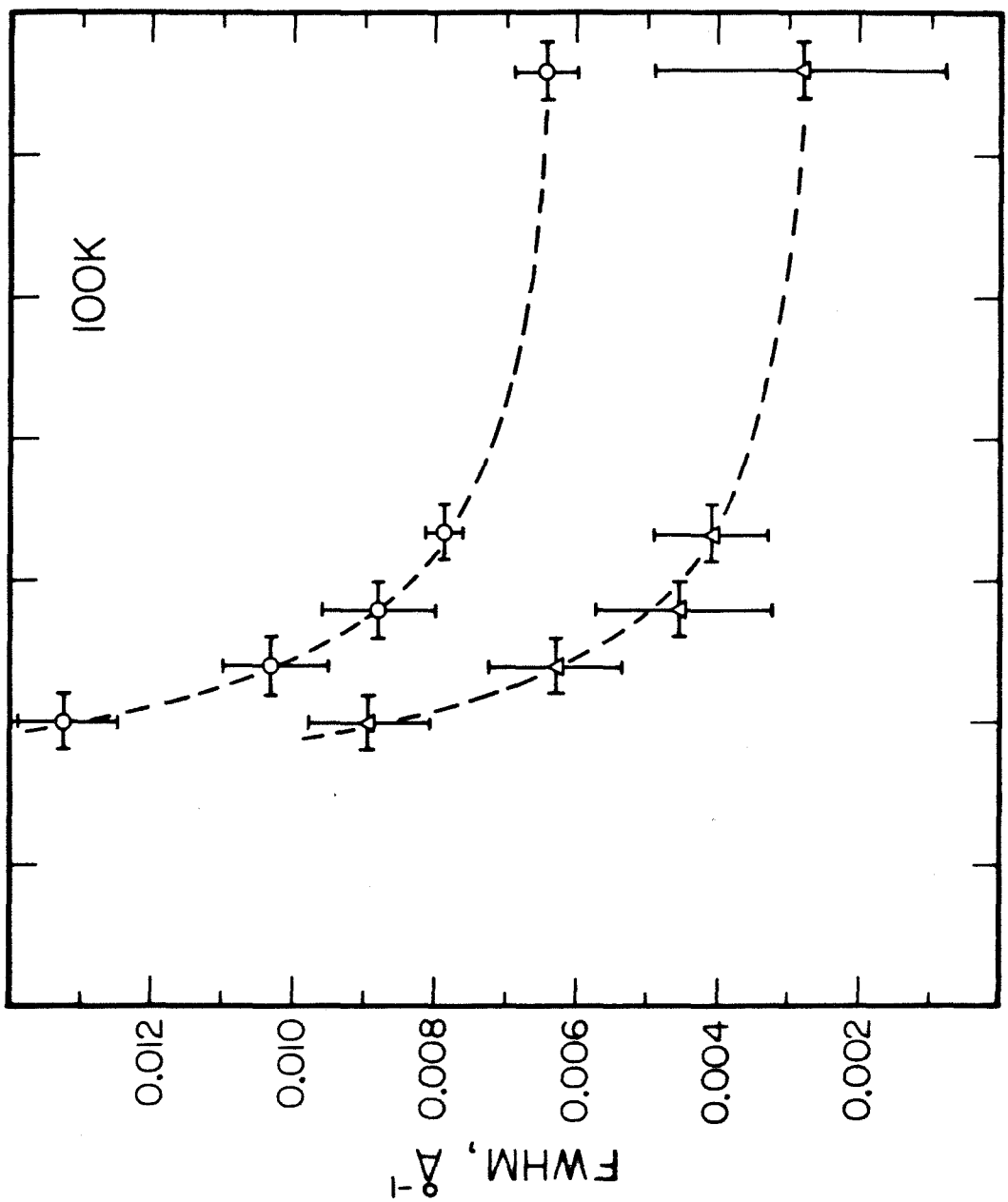
100K
FWHM, Å⁻¹
0.012
0.010
0.008
0.006
0.004
0.002
0.05
0.10
0.15
0.20
0.25
0.30
θ

Figure 4

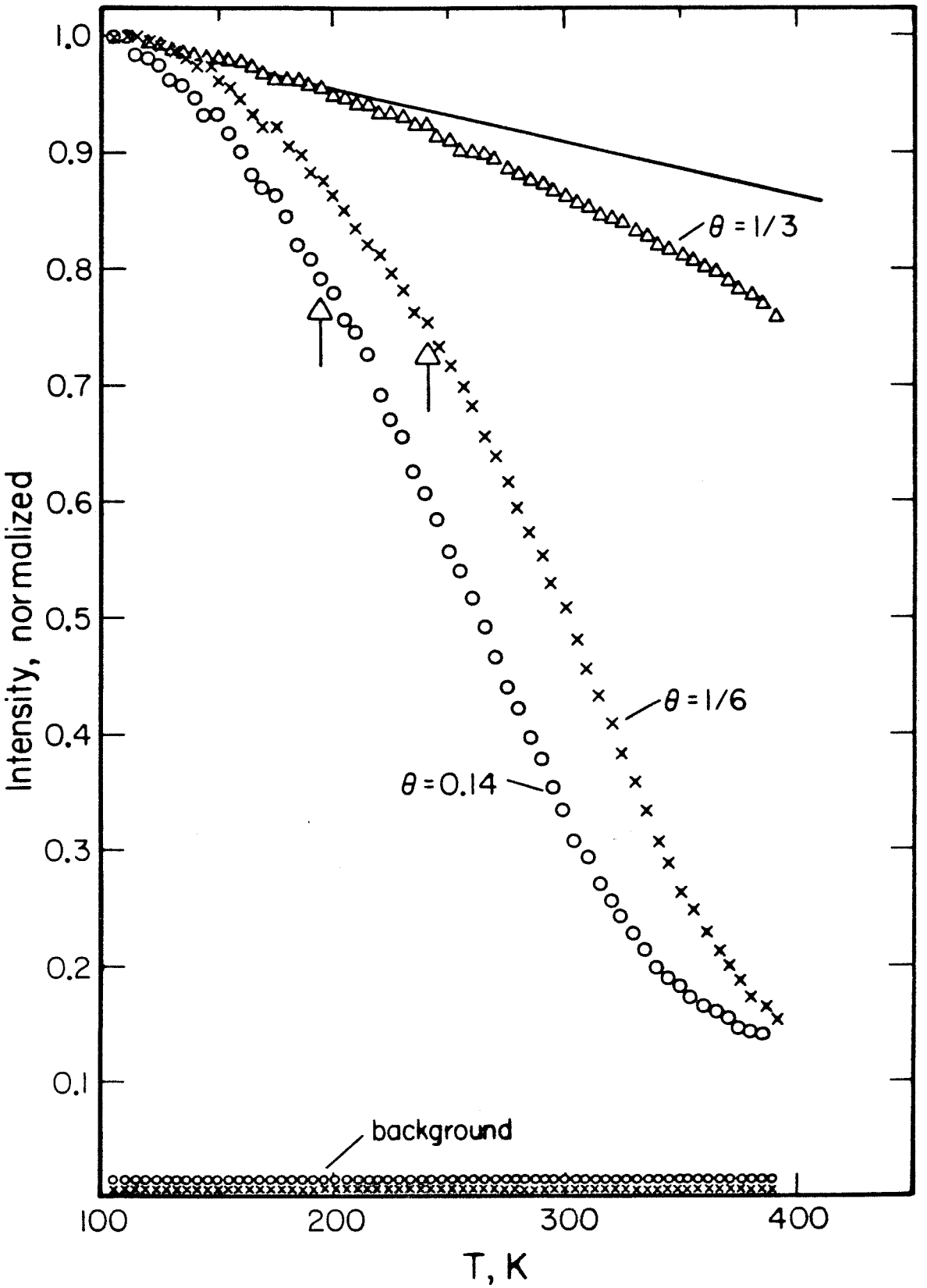
1.0
0.9
0.8
0.7
0.6
0.5
0.4
0.3
0.2
0.1
Intensity, normalized
θ = 1/3
θ = 1/6
θ = 0.14
background
100
200
300
400
T, K

Figure 5

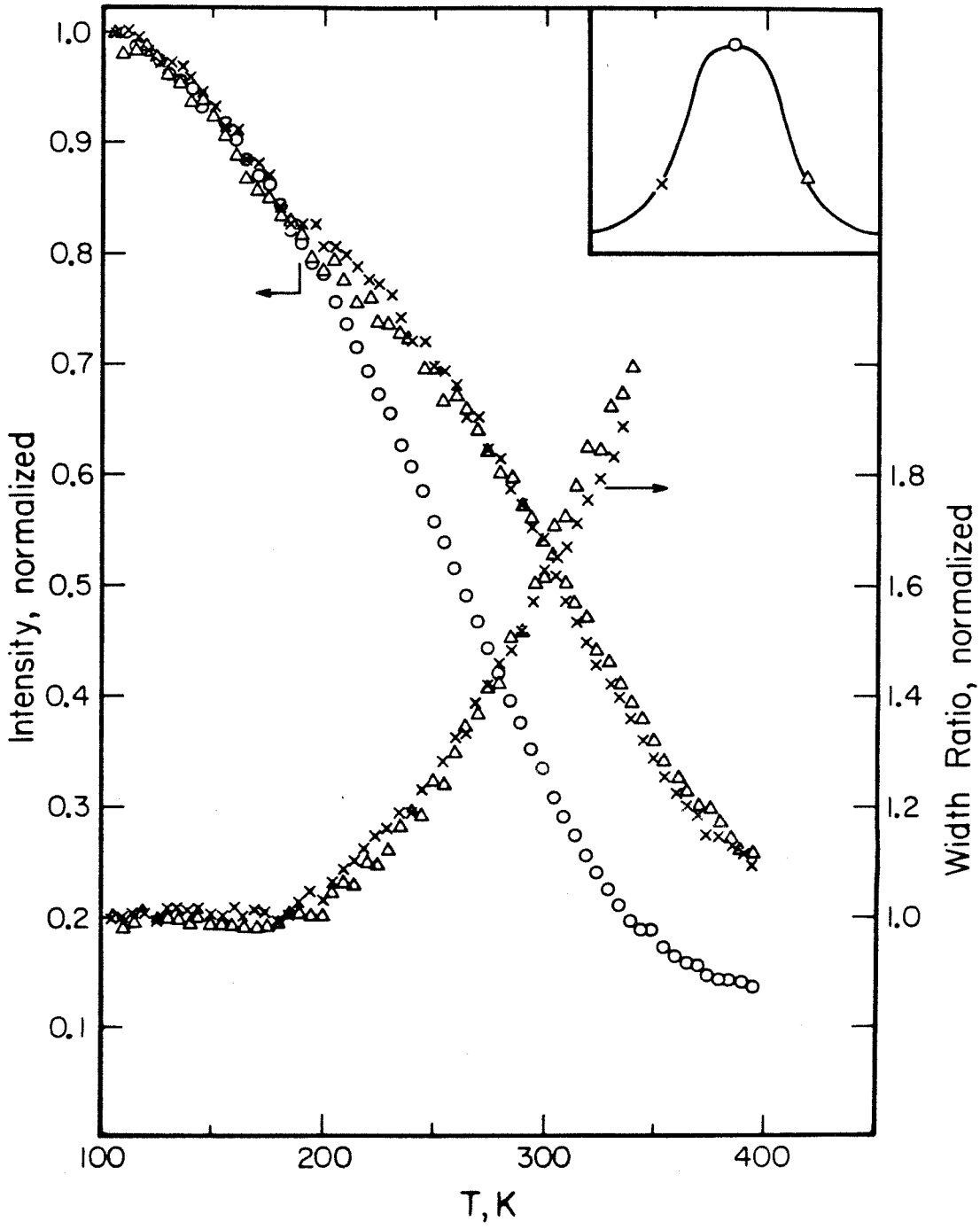
1.0
0.9
0.8
0.7
0.6
0.5
0.4
0.3
0.2
0.1
Intensity, normalized
1.8
1.6
1.4
1.2
1.0
Width Ratio, normalized
100
200
300
400
T, K

Figure 6

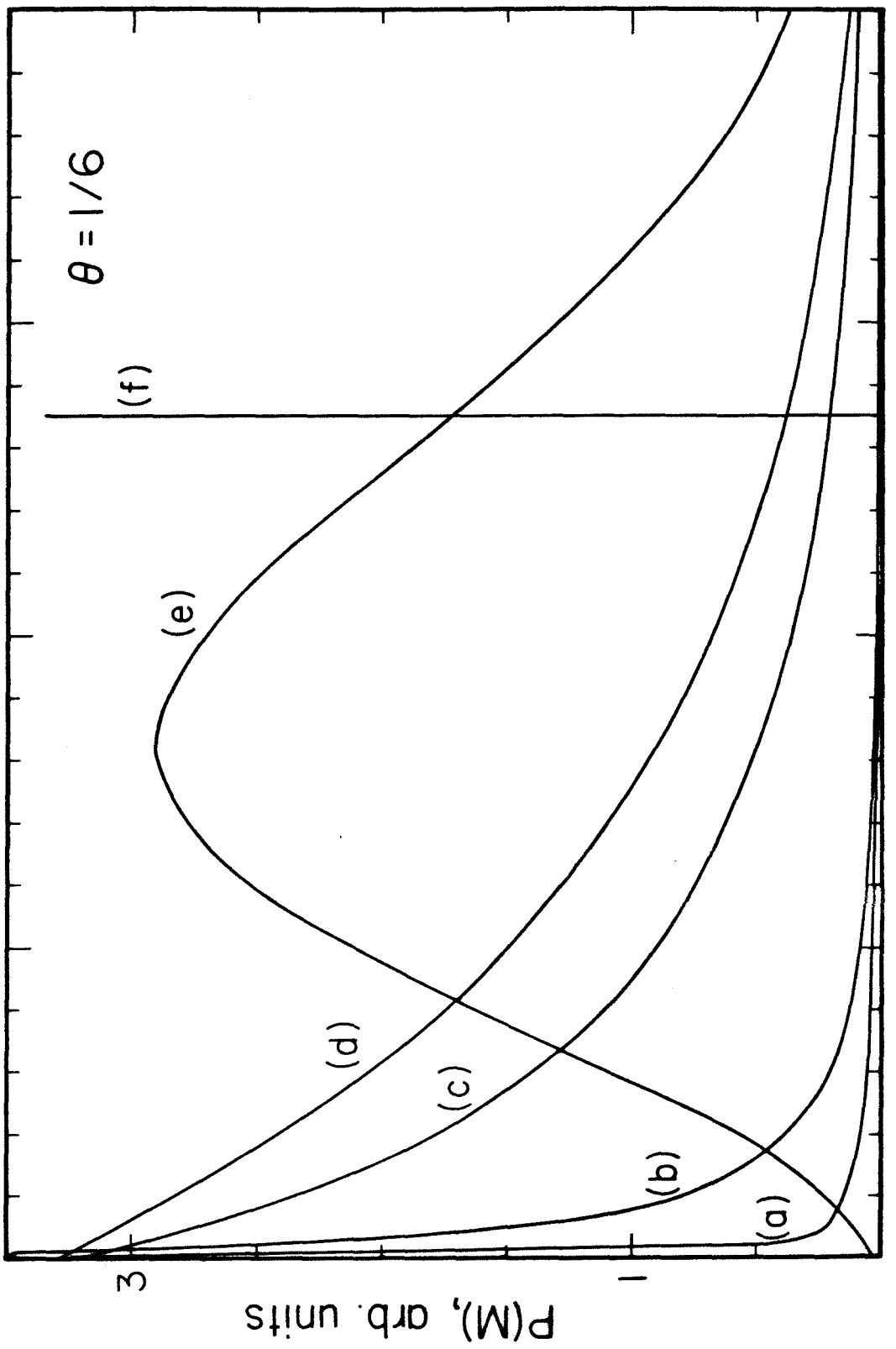

Figure 7

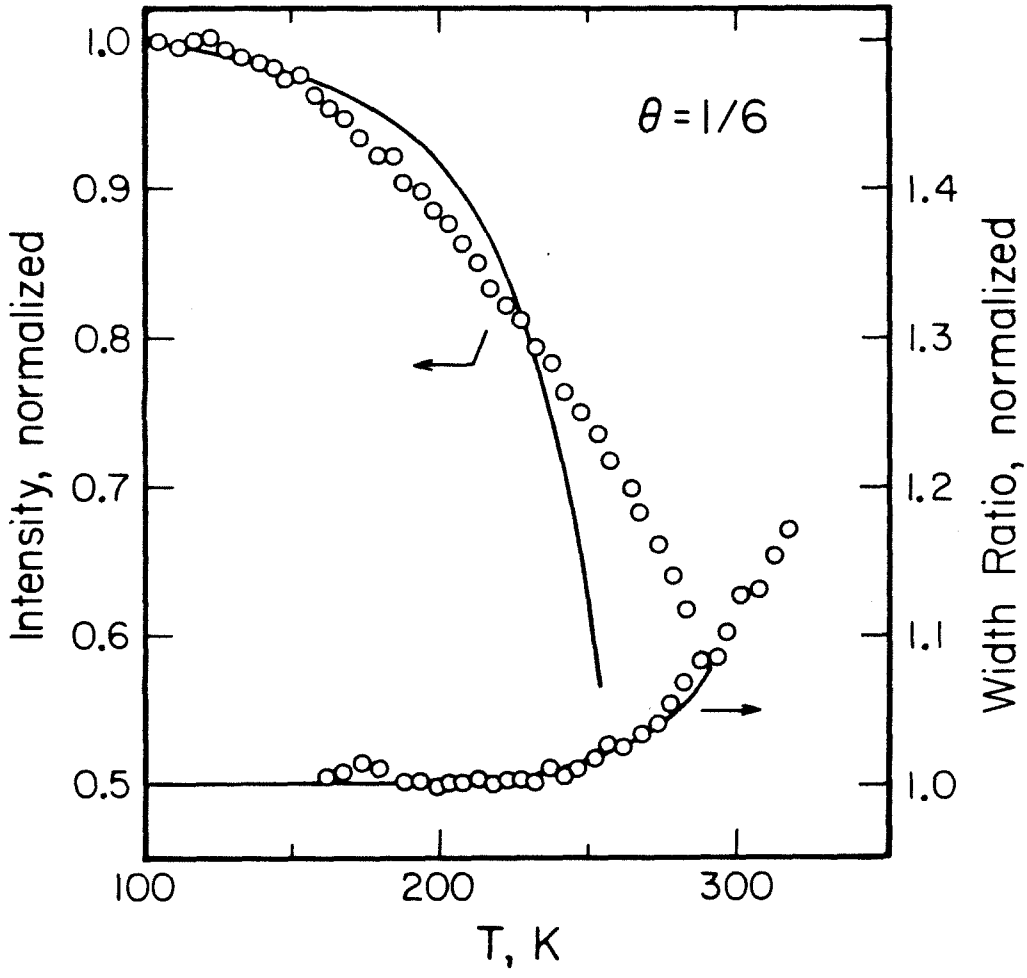
θ = 1/6
Intensity, normalized
Width Ratio, normalized
T, K
1.0
0.9
0.8
0.7
0.6
0.5
1.4
1.3
1.2
1.1
1.0
100
200
300

Figure 8

Section VII.

Conclusions

Low-energy electron diffraction has been used to study overlayer order in a variety of chemically adsorbed systems. Experimental studies have been performed for S/Ir(110), H + CO/Rh(111), and CO/Ru(001). Computational studies have been performed for O/W(110) and for a generalized island-forming system. The results of each study are summarized in the following.

A Monte Carlo simulation of the order-disorder behavior of oxygen on W(110) was performed. Oxygen forms a (2x2) overlayer beginning at very low coverages on W(110). This indicates that ordered islands form as the result of an attractive interaction. The binding site of oxygen on this surface is known from dynamical LEED calculations. A set of three interaction energies, consistent with the symmetry of the overlayer and binding site and with the observation of island formation, was chosen for the Monte Carlo calculation. The simulation was performed to model the experimental order-disorder behavior of O/W(110) at coverages of 1/4 and 1/2. It was not possible to make a unique determination of the three interaction energies on the basis of the two experimentally determined transition temperatures. However, two equations relating the three interaction energies to the transition temperatures were derived. In addition, representative curves of the internal energy, the heat capacity and the entropy as functions of temperature through the transition were calculated.

The co-adsorption of hydrogen and CO on Rh(111) was studied by LEED and thermal desorption mass spectrometry. CO forms a series of three LEED patterns with increasing coverage when it is adsorbed alone. Hydrogen adsorbed alone causes no observable changes in the clean surface LEED pattern. Addition of hydrogen to a CO overlayer causes the LEED pattern to change to one corresponding to a higher coverage of CO. If CO is added to a

surface with a hydrogen overlayer, all the clean surface LEED patterns form, but at lower coverages of CO. These results, combined with the thermal desorption mass spectrometric measurements, indicate that there is a strong repulsive interaction between the adsorbed hydrogen atoms and CO molecules, and that CO adsorbs via a mobile, physically adsorbed intermediate state. The repulsion between hydrogen atoms and CO molecules is effective over distances up to 2.7 to 3.1 angstroms, indicating that it is a through-metal interaction.

Overlayers of sulfur atoms were prepared on the reconstructed Ir(110)-(1x2) surface by exposing the crystal to hydrogen sulfide. A (2x2) LEED pattern with the ((2n+1)/2 0) beams missing was observed for low coverages of sulfur. More complex, and less well developed LEED patterns were observed at higher sulfur coverages. The missing beams in the (2x2) pattern indicate that the overlayer has either a p1g1 or a p2mg symmetry. This symmetry requires a coverage of one sulfur atom per reconstructed substrate unit cell. A possible structure for the overlayer is one in which the sulfur atoms are located in alternating three-fold sites in the troughs of the surface.

Calculations and computer simulations were performed to determine the effect on the LEED pattern of having a spatial distribution of small islands on the surface. It was shown that if the distribution of island positions is random, interference of electrons scattered from different islands will only contribute intensity to tne substrate beams. In this case, the overlayer beam profiles are the sum of the profiles due to the individual islands on the surface. To determine the effect of a non-random distribution of island positions on the beam profile, computer simulations of island-containing overlayers were performed. It was found that the result for a random distribution holds as long as there is no correlation between the domains of adjacent

islands.

Experimental studies of island formation and disordering for low coverages of CO on Ru(001) were performed. Measurements of the beam profile as a function of CO coverage were made at low temperature. The profiles increase in width rapidly with decreasing coverage. This indicates that smaller islands are present at lower coverages, as might be expected. The coverage dependence of the beam width is inconsistent with a step-limited model of island formation. This suggests that island formation is diffusion limited in this system. The disordering of the islands was monitored through changes in the LEED beam intensity and width. The disordering appears to be influenced strongly by the finite size of the islands. Through modeling of the island dissolution, it was found that only one distribution of island sizes is consistent with the observed behavior. Thus a unique determination of the island size as a function of coverage was possible.

Section VIII.

Appendices

1. Construction of an Ultraviolet Photoelectron Spectrometer.

2. Installation of an Electron Multiplier for Detection of Small LEED Signals.

Appendix 1

Construction of an Ultraviolet Photoelectron Spectrometer

An ultraviolet photoelectron spectrometer similar to that designed by Starbuck **(1)** has been constructed. It consists of a cold cathode noble gas resonance lamp with a differentially pumped, windowless light path into the UHV chamber. A standard Varian four-grid LEED optics will be used for measuring the energy distribution of the photoelectrons. With the addition of an electron multiplier to the Faraday cup which is mounted on the LEED optics (Appendix 2), it will also be possible to do angle-resolved UPS in this system **(2)**.

A. Components of the Spectrometer

A cross sectional drawing of the lamp and the light path is shown in Fig. 1. A high voltage is applied between the anode and cathode using a CVC 0 to 5000 volt DC power supply (model # SDC-100). The cathode is air cooled wth a small fan attached to the safety cage. The quartz discharge capillary is cooled by flowing water through a surrounding jacket as shown in Fig. 1. Two discharge capillaries were constructed, one with a 2 mm and the other with a 1 mm diameter internal bore. This will allow a determination of whether variation of the bore diameter can be used to improve the photon flux from the lamp. The light path consists of the copper anode, the first pumping gap, a segment of precision bore capillary (I.D. = 2 mm), the second pumping gap, and a second segment of capillary which leads into the UHV chamber. Great care was taken in the machining of the components and in the glass blowing to make sure that all segments of the light path are aligned. Also, the capillary that enters the UHV chamber was gold coated and connected to ground to prevent charging effects.

A Varian 5/8" straight-through valve (model #951-5052) is used so that the lamp can be sealed off from the UHV chamber when not in use. Other-

wise the diffusion pumps would have to be kept running at all times.

An overview of the lamp and the components of the differential pumping system is shown in Fig. 2. The diffusion pumps had to be located quite far from the pumping gaps to fit around other parts of the system. A Nupro O-ring sealed Butterfly Valve (model # 304-24VFO) is located between each pump and pumping gap to prevent vapor from the diffusion pump oil from getting into the lamp and light path when there is no liquid nitrogen in the traps. A Perkin-Elmer Ultek precision port aligner (model # 283-8510) between the straight-through valve and the UHV chamber allows the photon beam to be aimed precisely at the crystal. This is especially important in doing angle resolved photoemission. Two difficulties arose in installing the port aligner. The first was that the bolt holes on the aligner and on the system flange to which it is mounted are both tapped. This problem was surmounted by the construction of special bolts. The bolts were threaded on one end to fit the port aligner. The other end was milled to a small enough diameter to fit through the holes on the system flange, and its end was threaded to accept a nut. The port aligner thus was installed by threading the bolts into the port aligner, then bringing the port aligner to the system flange and sliding the six bolts through the flange holes and installing the nuts on the system side of the flange. The second difficulty arose in installing the nuts. As shown in Fig. 2, the port aligner is immediately adjacent to the system flange which holds the CMA. One of the nuts had to be installed in a very small space between the two. The use of a right angle wrench and a great deal of patience were needed to tighten the nut enough to achieve a vacuum tight seal. The same will be required (at least) if it is ever necessary to remove the port aligner. A support to keep the weight of the lamp off of the system flange and the port aligner is located below the straight-through

valve. In addition, a clamp attached to the CMA flange braces the straight-through valve from above. This is to prevent the application of torque to the delicate port aligner when opening and closing the valve. Photographs of the components of the lamp and light path are shown in Fig. 3.

The operation of this lamp has never been tested, however a similar lamp constructed at the same time has been used quite successfully **(3)**. Experience with that lamp has shown it is necessary to install a metering valve in the He line to control gas flow into the discharge tube. A Nupro valve (parts B-4SG and NY-1S-S6) has been purchased for that purpose. Details of lamp operation are described in Ref. 3.

B. Vacuum Calculations

A calculation of the pressure rise in the vacuum chamber during operation of the lamp was done for several commercially available diffusion pump-liquid nitrogen trap combinations. As shown below, a Varian M2 diffusion pump with a Varian 0325 cryotrap has sufficient pumping speed for this application.

The equations for determining conductance depend on the flow regime of the gas according to the equations **(4)**

$D/\lambda > 110$ viscous flow

$1 < D/\lambda < 110$ intermediate flow

$D/\lambda < 1$ molecular flow

where:

D = diameter of the pipe

ξ = diameter of the molecule

$$\lambda = (2.33 \times 10^{-10})T/\xi^2 P$$

To obtain a He(I) line the lamp will be operated with less than one torr of He in the discharge region. The value of D/λ for the anode can thus be calculated.

$\xi(He) = 1.86 \times 10^{-8}$ cm

$D = 0.2$ cm

$T \simeq 500$ K (estimate)

$D/\lambda = 6 \rightarrow$ intermediate flow

The length of the anode is 1.9 cm. Therefore using a standard equation (4), the conductance can be calculated to be

$$0.22\ l/s \leq C_{anode} \leq 0.29\ l/s\ .$$

If molecular flow is assumed in the rest of the pumping path, the conductances can be calculated using standard equations for pipes, rectangular pipes and pipes with elbows (4) for various segments of the pumping path.

Ignoring pumping from the second pump through the short capillary, the pressure in the first pumping gap, P_1, can be calculated as below. The pumping speed of the diffusion pump is

$$S_p = 175\ l/s\ .$$

The pumping speed in the discharge region is

$$S_D = 1/S_p + 1/C_a + \sum_i 1/C_i = 0.29\ l/s\ ,$$

where C_i indicates the conductance of a segment of the path between the anode and the first pump, and where $C_a = 0.29\ l/s$ has been used as the worst case.

The throughput is thus

$$Q = SP = (.29\ l/s)(1\ \text{torr}) = 0.29\ \text{torr-}l/s\ .$$

This is below the maximum throughput of the pump, 0.8 torr-l/s.

The pumping speed in the first pumping gap is

$$S_1 = 1/S_p + \sum_i 1/C_i = 31.3\ l/s\ .$$

Therefore the pressure in the first pumping gap is

$$P_1 = Q/S_1 = .0092\ \text{torr}\ .$$

Now the assumption of molecular flow can be checked:

$\lambda = 2.93$ cm (estimating T = 400 K)

$D = .64$ cm

$D/\lambda = .217$ → The assumption is good.

The pressure in the second pumping gap, P_2, can be calculated by ignoring any possible effect due to the pumps in the vacuum chamber pumping through the long capillary. The pumping speed in the first pumping gap due to the second pump is

$$S_{1,2} = 0.04\ l/s\ .$$

Therefore the throughput is

$$Q = (0.4\ l/s)(.0092\ \text{torr}) = 3.7 \times 10^{-4}\ \text{torr-}l/s\ .$$

And the pumping speed in the second gap is

$$S_2 = 31.8\ l/s$$

So that

$$P_2 = Q/S_2 = 1.2 \times 10^{-5}\ \text{torr}$$

The pumping speed of the ion pump in the UHV chamber for He is

$$S = 48\ l/s\ .$$

The conductance of the long capillary is

$$C = .014\ l/s\ .$$

The pumping speed in the second gap due to the pumps in the vacuum chamber is therefore

$$S = .014\ l/s\ .$$

The throughput is

$$Q = (.014\ \ell/s)(1.2 \times 10^{-5}\ \text{torr}) = 1.6 \times 10^{-7}\ \text{torr-}\ell/s\ .$$

Therefore the pressure rise in the UHV chamber due to operation of the lamp is

$$\Delta P = Q/S_p = 3.3 \times 10^{-9}\ \text{torr}\ .$$

C. Energy Analysis

As shown in Fig. 4, the UV lamp is positioned so that the beam of photons strikes the crystal when it is located at the center of curvature of the LEED optics. The modification of a standard Varian four-grid LEED optics to allow measurement of Auger electrons is a standard procedure **(5-8)**. A very similar modification allows the LEED optics to be used for energy analysis of the lower energy (0 to 35 eV) electrons generated in UPS **(1)**. The only major difference is that the retarding potential applied to the grids is swept over the small energy range needed for UPS rather than the large one needed for AES.

All the components necessary for a preliminary test of the spectrometer are available. The Varian CMA sweep generator can be used to supply the retarding voltage to the LEED grids. A Heath kit sine wave generator is available to apply a perturbing voltage to the crystal **(1)**. A PAR lock-in amplifier can be used to take the first derivative of the photoelectron current. For preliminary tests the lock-in can be operated with a long time constant, and the data recorded on an x-y recorder.

For actual acquisition of data, it will be necessary to obtain a good programmable power supply to provide a computer controllable retarding voltage. The signal-to-noise in the spectra could then be improved by averaging many energy scans using the laboratory computer.

The method of data acquisition when using the Faraday cup as a detector in angle-resolved photoemission has been discussed by Weeks *et al.* The Faraday cup is equipped with an einzel lens that can be used as a retarding field analyzer in the same way as the LEED grids.

References

1. James Edgar Starbuck, Masters Thesis, Cornell University, 1974.

2. S. P. Weeks, C. D. Ehrlich and E. W. Plummer, Rev. Sci. Instrum. **48**, 190 (1977).

3. P. A. Thiel, PhD Thesis, California Institute of Technology, 1981.

4. A. Roth, *Vacuum Technology*, North Holland Publishing Company, New York, 1976.

5. P. W. Palmberg, J. Appl. Phys. **38**, 2137 (1967).

6. R. E. Wever and W. T. Peria, J. Appl. Phys. **38**, 4355 (1967).

7. P. W. Palmberg, Appl. Phys. Lett. **13**, 183 (1968).

8. N. J. Taylor, Rev. Sci. Instrum. **40**, 792 (1969).

Figure Captions

Fig. 1: Cross sectional view of resonance lamp, light path and straight-through valve.

Fig. 2: Top view of the lamp and differential pumping system.

Fig. 3: Photographs of components of the lamp and light path.

a. Support pieces for water cooled discharge capillary, water cooled discharge capillary and cathode.

b. Cathode and water cooled discharge capillary assembled, with phenolic rods in place.

c. T-piece with copper anode visible.

d. T-piece, discharge capillary and cathode assembled, with thermistor gauge in place.

e. Modified straight-through valve, with the inset piece that holds the short capillary. Rods attached to inset piece are for insertion and removal.

f. End-on view of the straight-through valve showing the long capillary, with the port aligner, and special bolts for installation of port aligner.

Fig. 4: Schematic drawing of the UHV chamber showing the positions of the LEED optics, crystal and beam of photons.

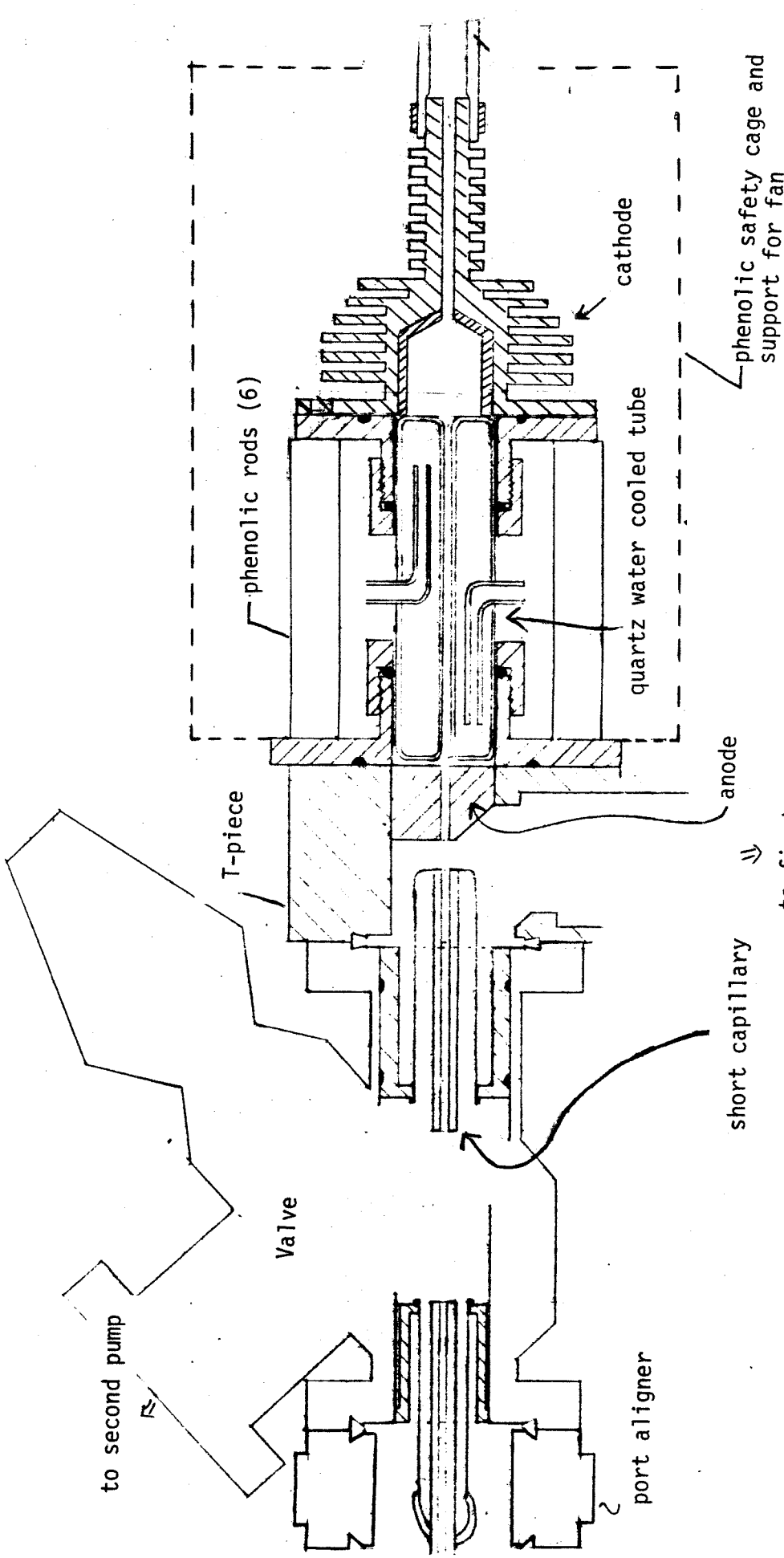
phenolic safety cage and support for fan
cathode
phenolic rods (6)
quartz water cooled tube
anode
T-piece
to first pump
short capillary
Valve
to second pump
port aligner

Figure 1

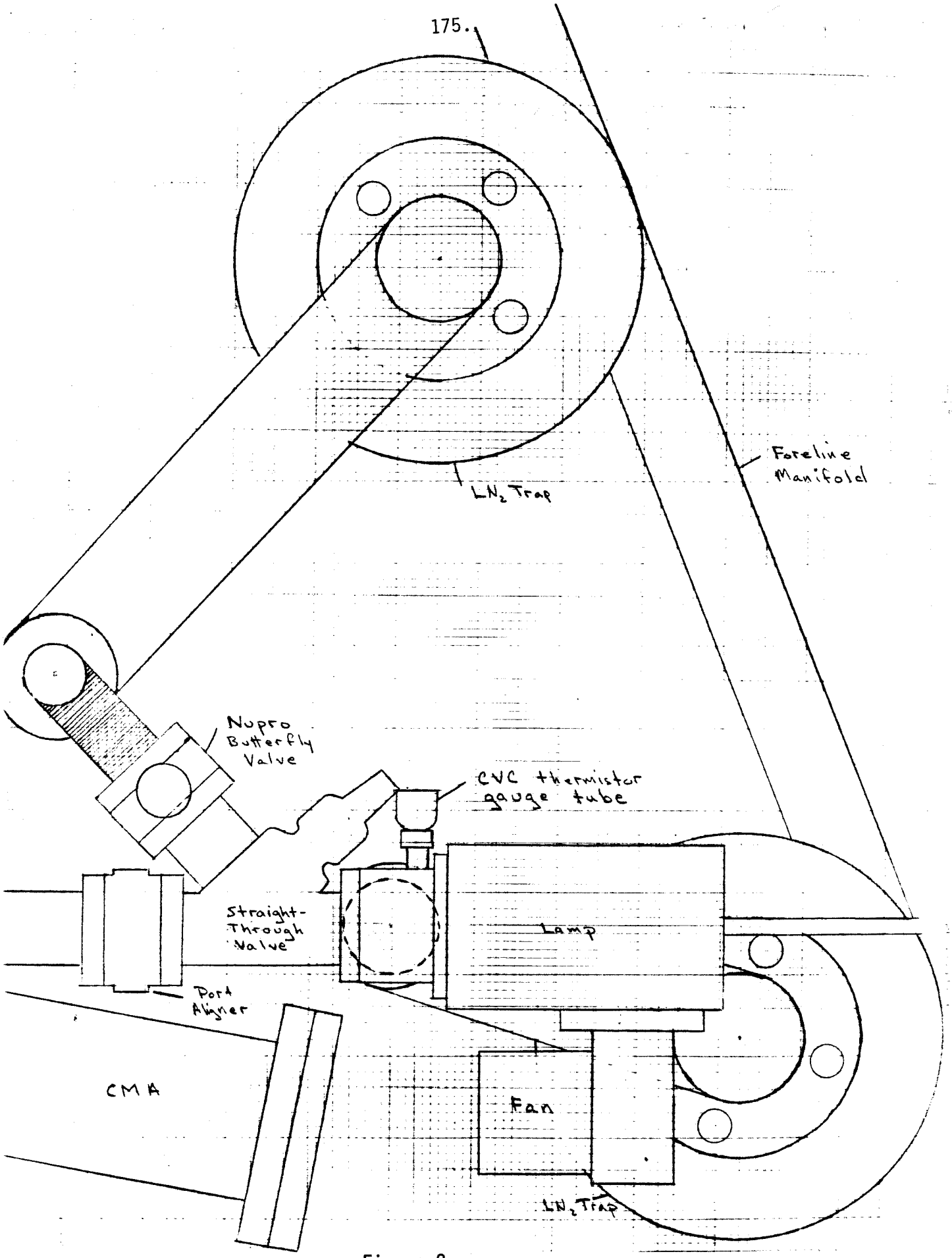
Foreline Manifold
LN_2 Trap
Nupro Butterfly Valve
CVC thermistor gauge tube
Straight-Through Valve
Lamp
Port Aligner
CMA
Fan
LN_2 Trap

Figure 2

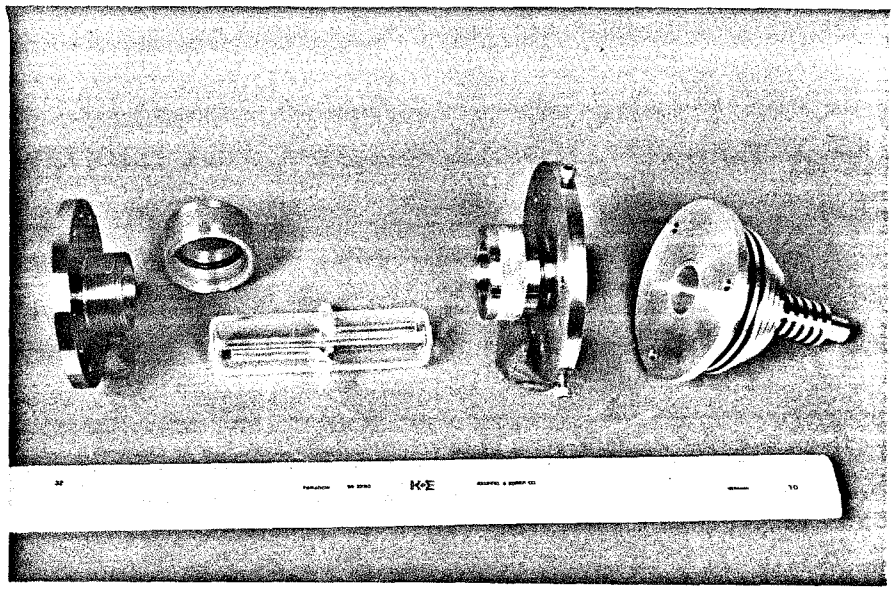

(a)

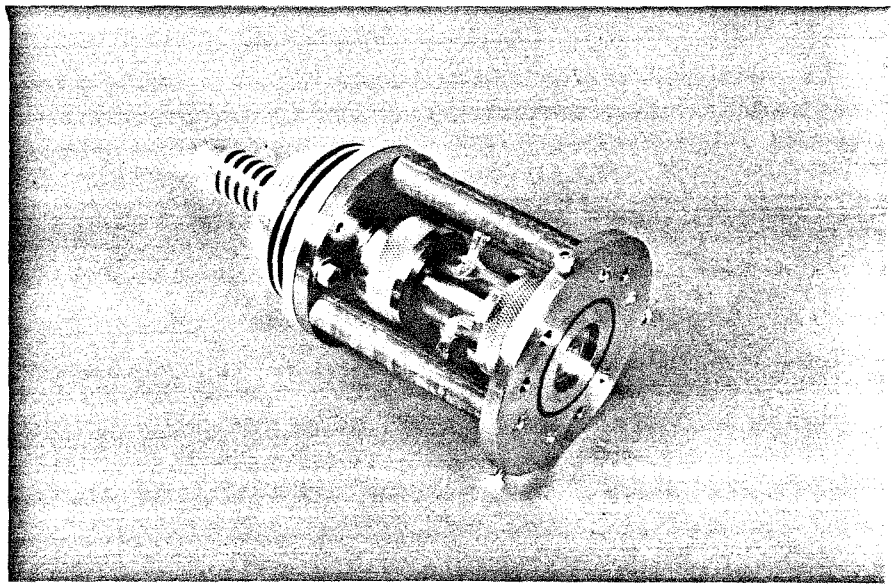

(b)

Figure 3

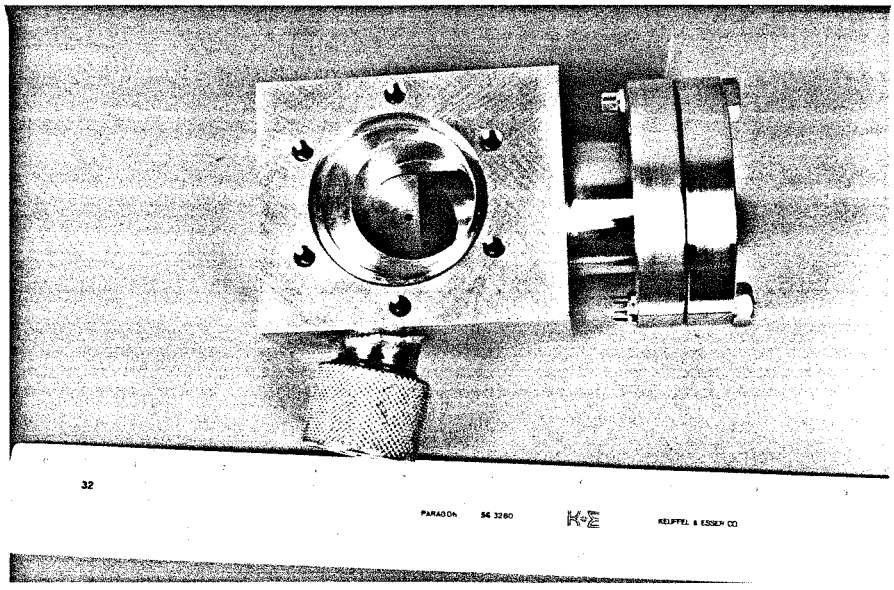

(c)

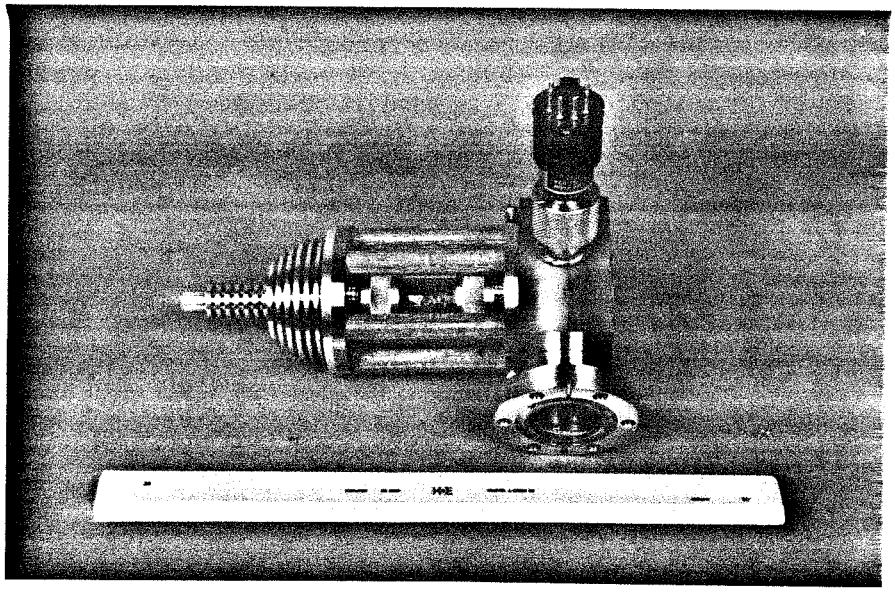

(d)

Figure 3

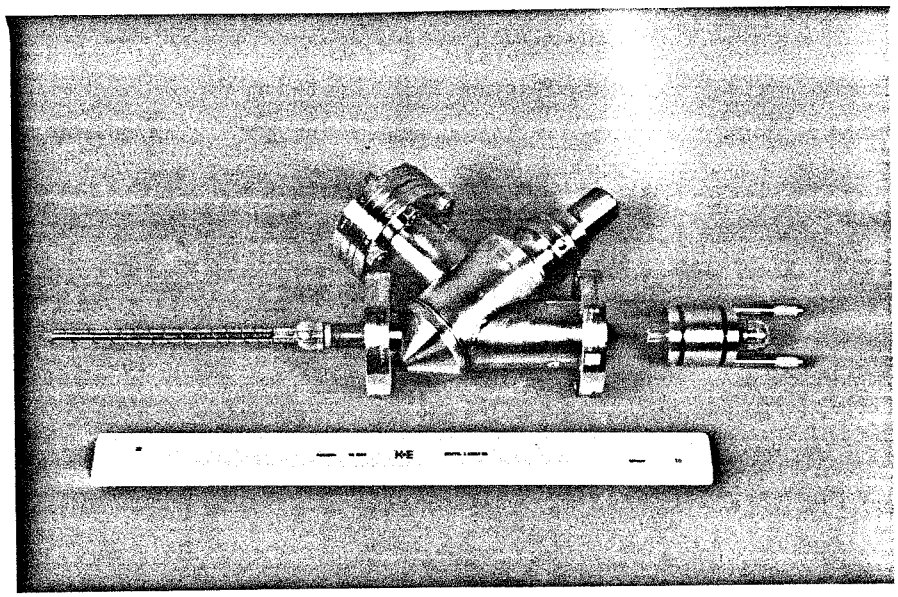

(e)

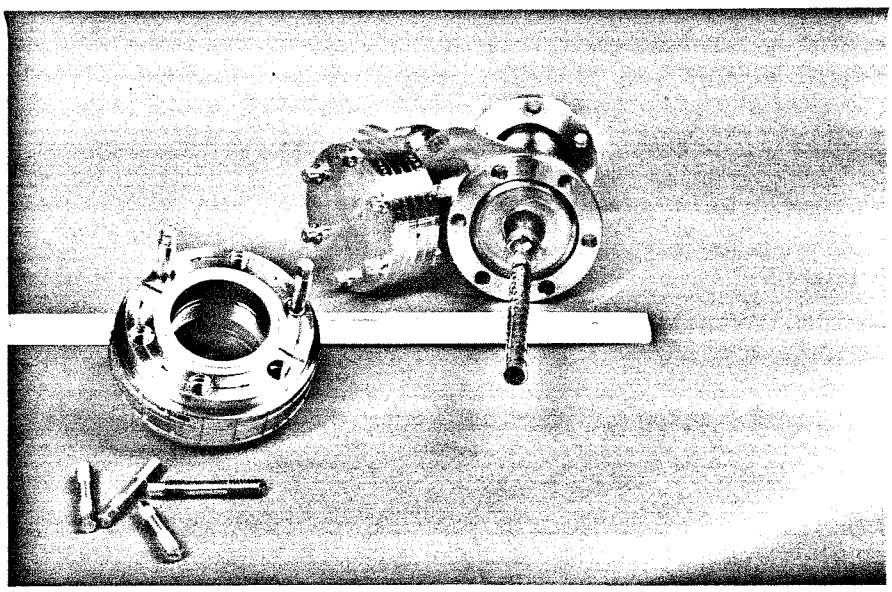

(f)

Figure 3

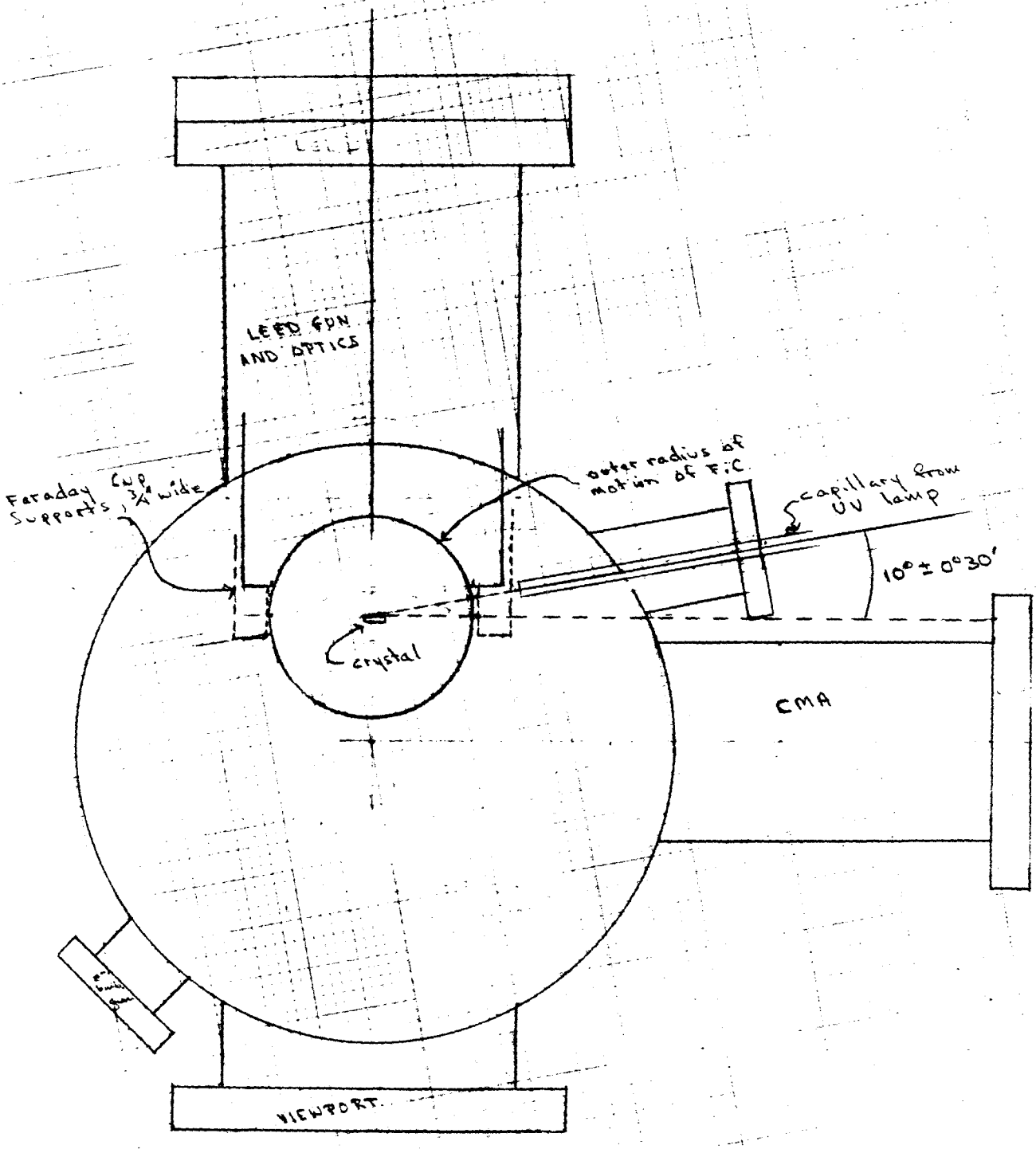
LEED GUN AND OPTICS
Faraday Cup Supports, 3/4 wide
outer radius of motion of F.C
capillary from UV lamp
10° ± 0°30'
crystal
CMA
VIEWPORT.

Figure 4

Appendix 2

Installation of an Electron Multiplier for Detection of Small LEED Signals

I. Introduction

A standard Varian LEED system is equiped with a movable Faraday cup which can be used to measure the intensity of diffracted electron beams. For an incident electron beam current of 10^{-6} A, a typical diffracted beam will have an intensity of about 10^{-9} A. Such currents can be measured directly with a picoammeter without difficulty. However, for molecular overlayers, incident beam currents of about a microamp are sufficient to cause electron stimulated desorption (ESD) **(1)**, and thus destruction of the system being observed. At lower incident beam currents ESD is reduced, but detection of the diffracted beam becomes difficult. Therefore some type of signal amplification becomes necessary if quantitative studies of molecular overlayers are to be done using LEED.

Weeks *et al.* **(2)** modified a Varian LEED system by installation of a channel electron multiplier (CEM) in the Faraday cup to do angle resolved photoemission. A similar modification is the obvious solution to the problem of detection of small currents in LEED. In the following two sections are discussed first the details of the installation of the CEM and second the measurement of diffracted beams using the CEM.

II. Installation of the CEM

A drawing of the unmodified Faraday cup is shown in Fig. 1. The cup is mounted on two arms, through each of which runs an electrical connection. One connection is used to supply a retarding voltage to an einzel lens in the Faraday cup. The other carries the current from the collector cage in the cup. To install the CEM, it was necessary to remove the collector cage and enlarge the Faraday cup by addition of a "housing". Also, a third electrical connection had to be made to supply the high voltage to the CEM.

A side view of the modified Faraday cup is shown in Fig. 2. The new housing extends above the original Faraday cup and is held in place by the screws that held the original back plate of the cup. The side plates of the new housing are clamped on with two brackets fastened by set screws, and thus are easily removable. One of the side plates contains a hole in which is mounted a Macor ceramic insulator. This is the electrical feedthrough for the signal from the CEM. The signal is collected on a piece of tantalum foil which is supported by a copper wire. The wire runs through the ceramic insulator. Outside the housing, the wire is insulated with ceramic beads and shielded electrically with a copper sheath taken from an RG-59 cable. This cable is tied to the arm of the Faraday cup and run out to a high voltage feedthrough (Ceramaseal model # 808B8880-1) on a port to one side of the LEED optics. The cable hangs loose to allow motion of the Faraday cup.

A hole was cut in the top of the original Faraday cup to accommodate the CEM. The multiplier is held in position by its two electrical connections. A 15 mil tantalum wire is attached to the tab at the back of the CEM and grounded by a spotweld to the top of the original cup. A second wire, insulated with ceramic beads, runs from the high voltage tab at the end of the CEM through the hole in the original housing to the feedthrough originally used for carrying the current from the collector cage. A top view of the modified Faraday cup is shown in Fig. 3. The electrical connection to the einzel lens was left unchanged. The other feedthrough was surrounded by a painfully machined ceramic insulator, so that a stainless steel "hairpin" could be positioned for electrical contact by a pressure fit. (The ceramic insulator cracked during installation and will probably disintegrate if it is ever removed.) The tantalum wire from the high voltage tab of the CEM was spotwelded to the "hairpin". Finally, the original aperture plate was replaced

with a plate with a 0.005" diameter aperture. This allows greater spatial resolution in the measurement of diffracted beams. Shop drawings of all new parts are in the "System Modifications" notebook in the laboratory.

Two initial difficulties were encountered in operating the CEM. The first was arcing in some of the Varian connections running back through the LEED optics when the high voltage was applied. This problem was circumvented by replacing some of the original insulators with larger ones. No arcing now occurs for voltages up to at least 2000 V. At the higher voltages that would be required for angle resolved photoemission **(2)**, it is possible that the insulators would fail again. If this occurs, the best solution would be to abandon the original connection all together, and make a new connection through the other side plate of the new housing. The second difficulty was the pickup of stray electrons in the system by the collector circuitry which is also at high positive voltage. A piece of tantalum foil was spotwelded over the gap between the old and new housing of the Faraday cup shown in Fig. 2. In addition, a cap with a hole in it was pressure fit into the port holding the collector feedthrough and the collector cable was passed through the hole. These two electrical shields reduced the background currents to quite acceptable levels.

III. Operation of the CEM

The channel electron multiplier (Galileo, part # 3556182) is of an unusual shape because of space limitations, but otherwise conforms to the specifications of the standard Galileo CEM. The multiplier is operated by grounding its front end and applying a high positive voltage, V, to the back end. A collector plate, biased to about V +200, is positioned 1 mm behind the CEM. The gain of the CEM is determined by the value of V. The maximum

output current is $V/10^{10}\ \Omega$ for a linear response.

Measurement of the signal from the CEM was done in simple analog mode using a floating electrometer (Keithley, model 601). A diagram of the circuitry **(3)** used to apply the high voltage, V, to the CEM, and V +200 to the collector through the electrometer, using only one high voltage power supply is shown in Fig. 4. The UHV feedthrough for the CEM is on the flange holding the LEED optics. The feedthrough for the collector is on a 2 ¾" flange immediately to one side of the LEED optics. When using the elecrometer in the configuration of Fig. 4, the case ground and low must be connected using the pins on the back of the electrometer. A lucite box was constructed to hold the electrometer, which is floating at V +200 during measurements. An isolation amplifier (Analog Devices model # 273J) is used so that the 0-1 V output of the electrometer can be monitored with an x-y recorder, or by the laboratory computer. The electrometer is a well-designed instrument that is very easy to operate. Only two modes of failure have been observed: (1) Battery failure (this is easy to confirm using the battery check switch), and (2) Failure of the low current ranges while the high (μA) current ranges remain accurate. This is due to degradation of the precision mega-ohm resistors. These resistors are quite inaccessible, so return to Keithley for repair is recommended. The repair is inexpensive (less than $100 in 1979) and relatively fast (2-3 weeks).

The incident electron beam current from the Varian LEED gun can be reduced by adjusting the filament voltage. The current monitor on the control unit is not useful below currents of 0.1 μA, so the current-to-ground through the crystal was measured to determine the gun current. At a filament voltage setting of about 1½ turns, the gun current is about 1 nA. Lower currents are possible, but with increasing noise levels, so 1 nA was the

lowest current used for experiments. At this incident beam current, with a 0.005" aperture, about 0.1 pA maximum of current can be expected to reach the CEM. To avoid overloading the CEM at this incident current, it is necessary to work at rather low gains. For work on overlayers of CO, voltages of 1500 V to 2000 V at the collector were used, giving a collector current of 1-10 nA. An approximate curve of gain versus collector voltage is shown in Fig. 5.

IV. Conclusion

The modified Faraday cup has been used successfully in quantitative measurements of LEED beams as described in an earlier chapter. In addition, it could be used with the photoemission lamp described in Appendix 1 for angle resolved photoemission. This would only require minor modifications of the apertures **(2)**.

References

1. T. E. Madey, Surface Sci. **79**, 575 (1979).

2. S. P. Weeks, C. D. Ehrlich and E. W. Plummer, Rev. Sci. Instrum. **48**, 190 (1977).

3. John Yehle, California Institute of Technology (1980).

Figure Captions

Fig. 1: Unmodified Faraday cup.

Fig. 2: Side view of the modified Faraday cup. Scale 5:1. The top piece and one of the side plates of the new housing can be removed without breaking any electrical connections.

Fig. 3: Top view of the modified Faraday cup. Scale 5:1. The position of the new insulator at the high voltage feedthrough is indicated by the dashed lines.

Fig. 4: Circuit used for measurement of signal from CEM (Ref. 3).

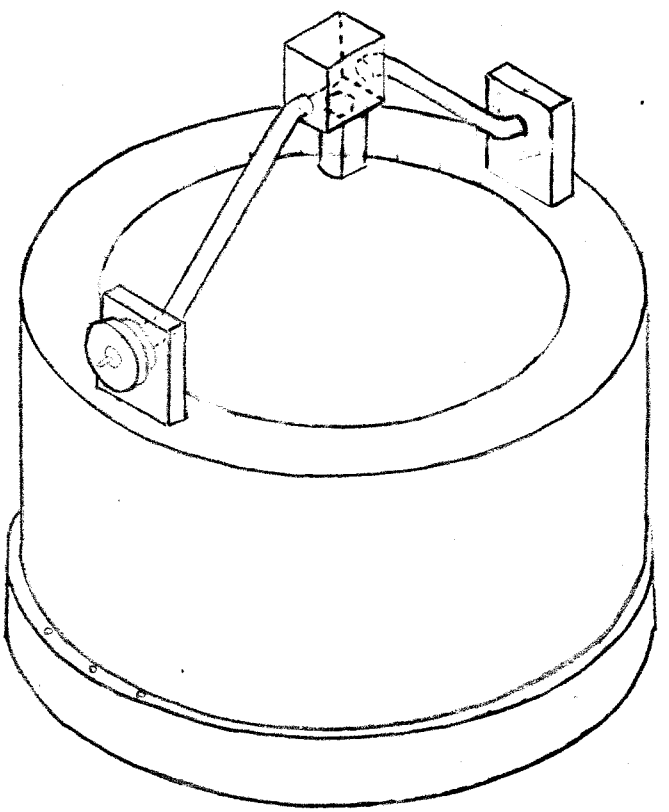

Figure 1

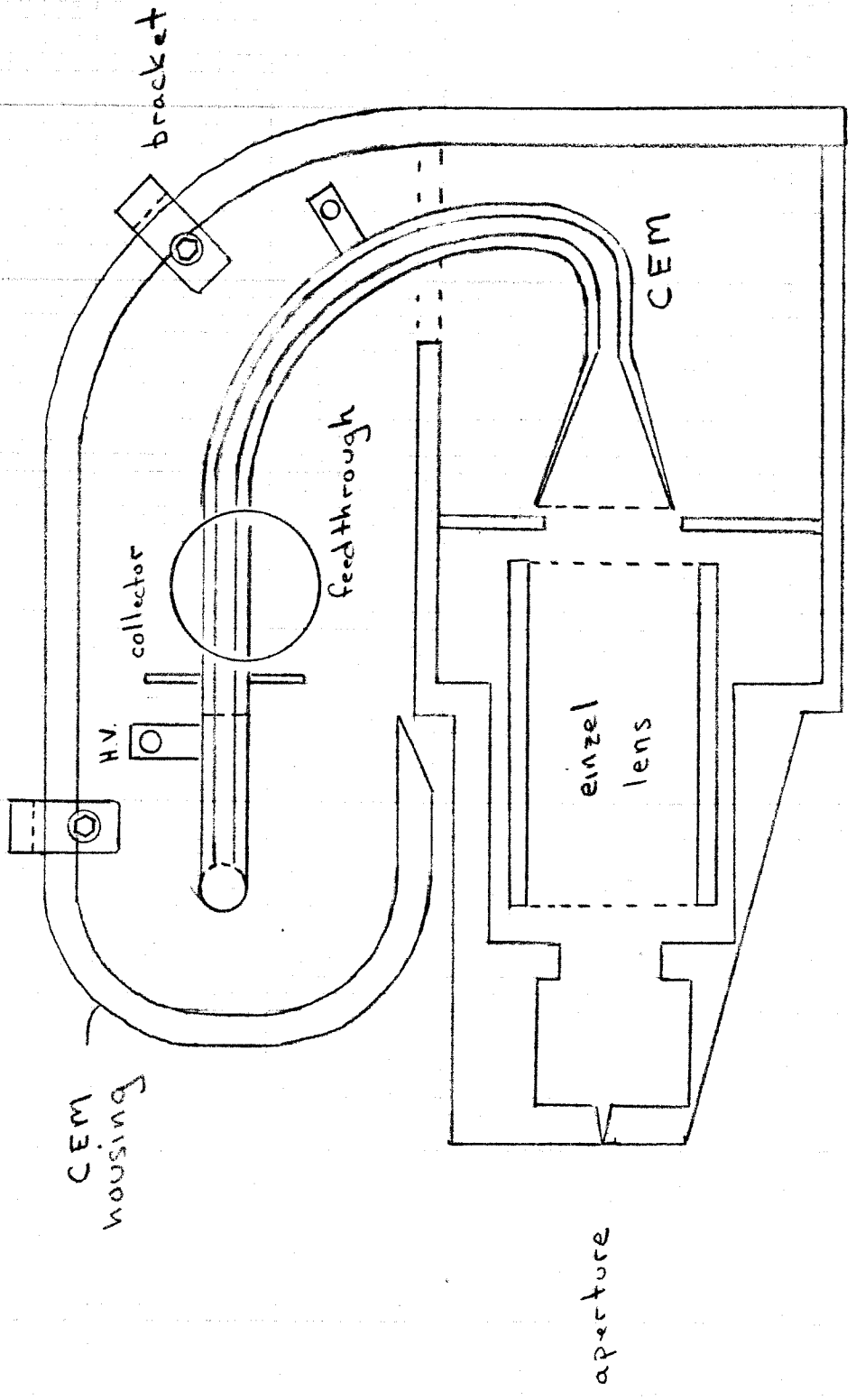
bracket
CEM
feedthrough
collector
H.V.
einzel
lens
CEM
housing
aperture

Figure 2

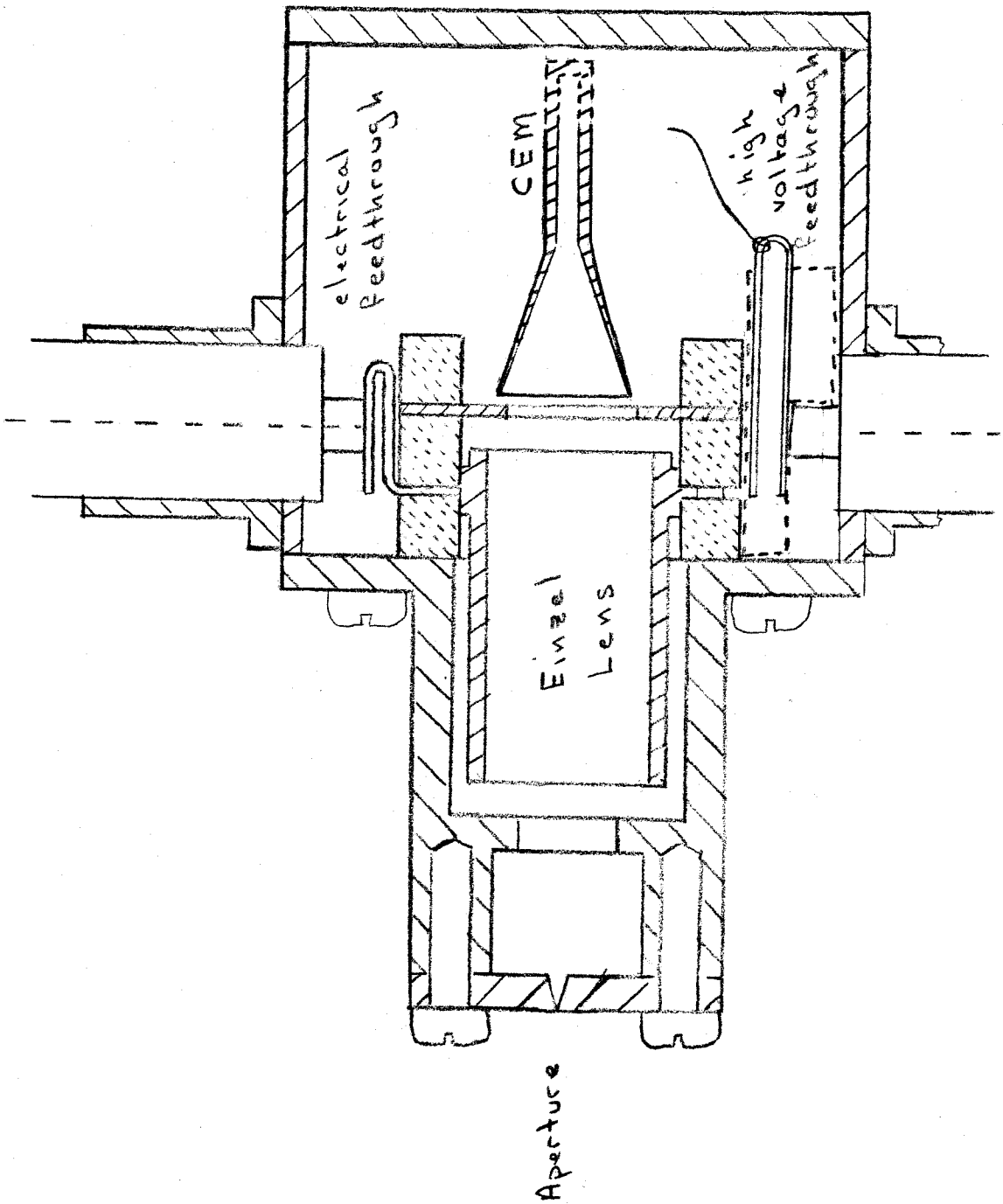
electrical feedthrough
CEM
high voltage feedthrough
Einzel Lens
Aperture

Figure 3

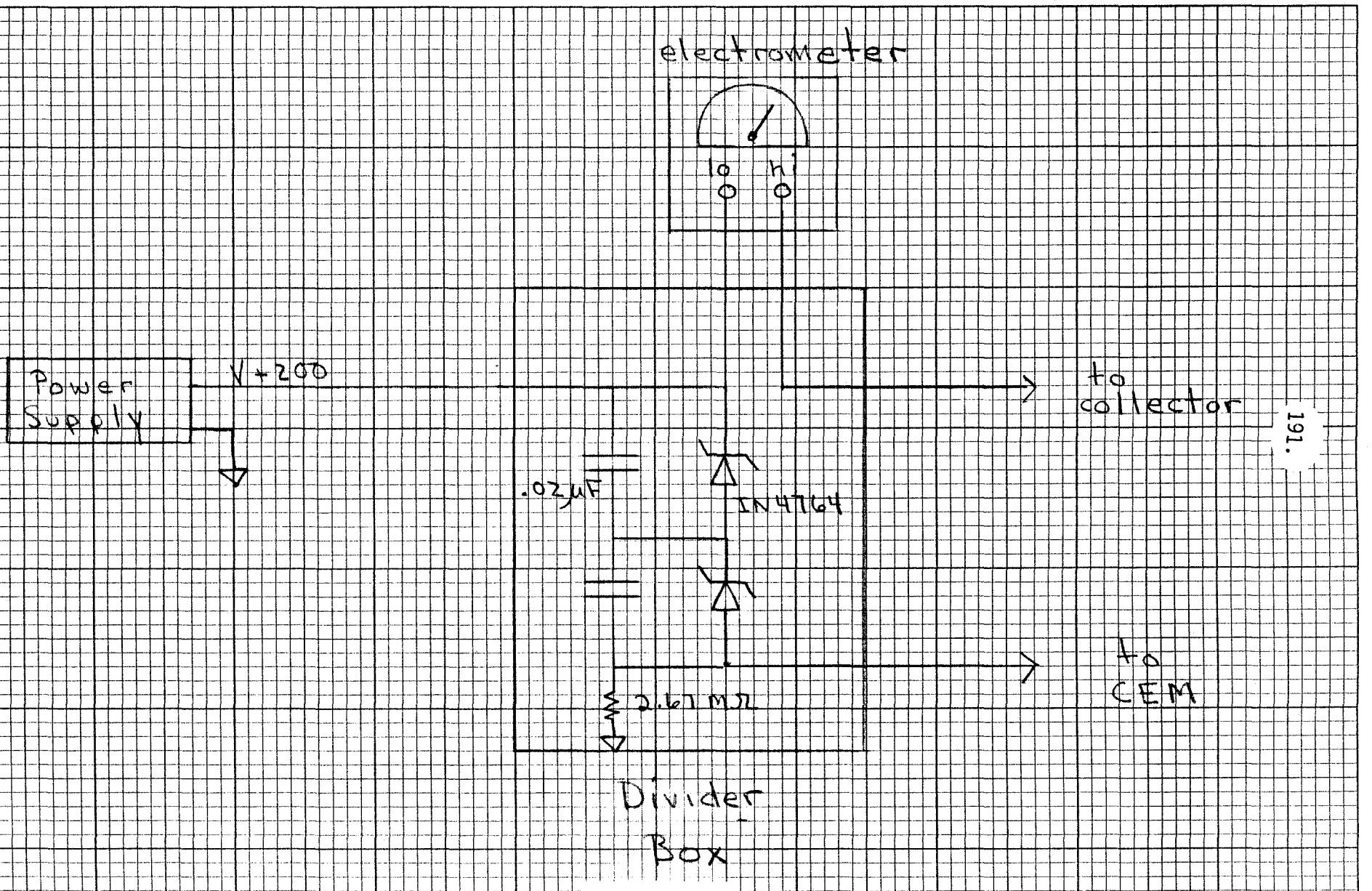
electrometer
lo
hi
Power Supply
V+200
to collector
.02μF
IN4764
to CEM
2.67 MΩ
Divider Box

Figure 4

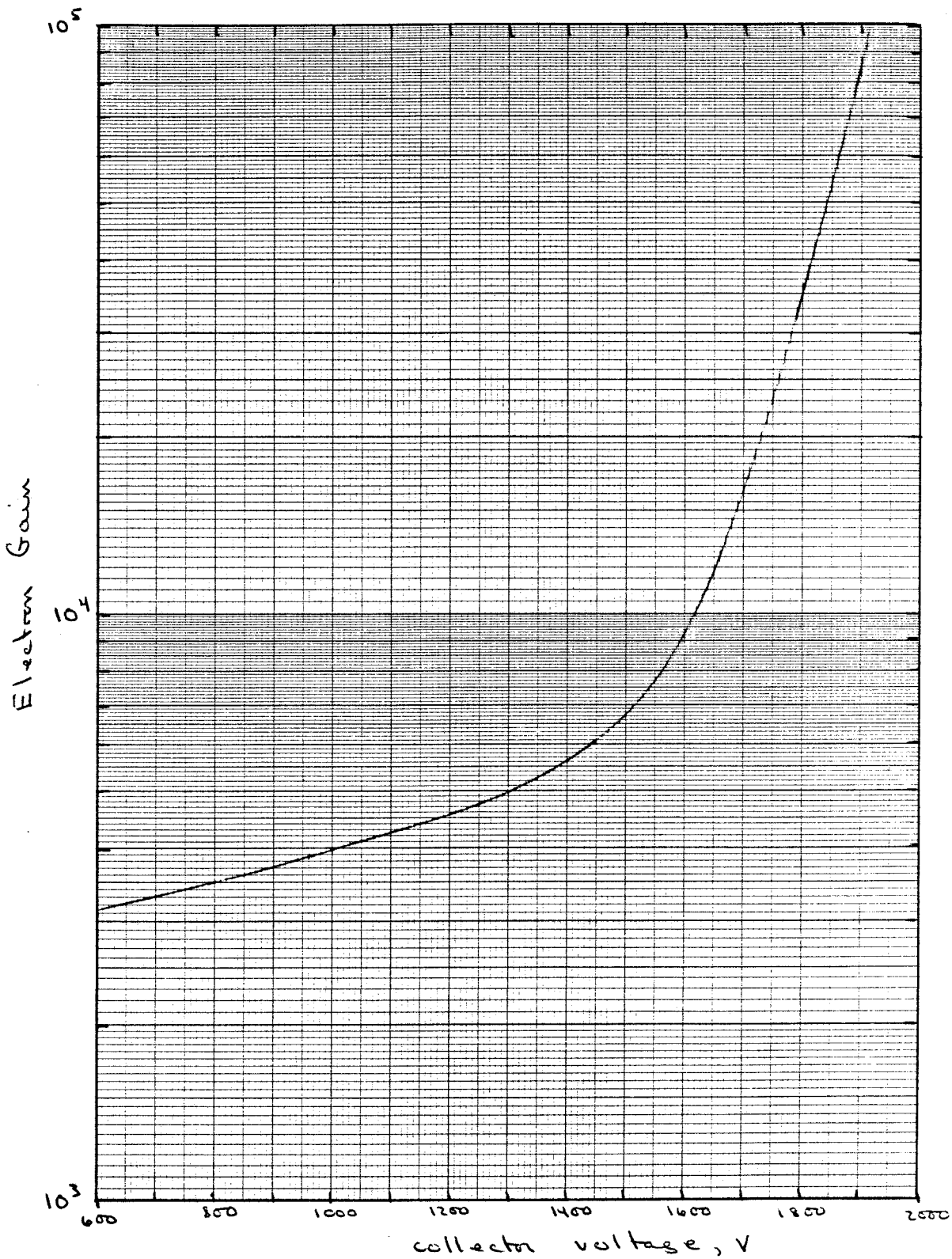
10^5
10^4
10^3
Electron Gain
600
800
1000
1200
1400
1600
1800
2000
collector voltage, V

Figure 5